7-17-2014 12:00 AM

# Early Mechanisms of Retinal Degeneration in the harlequin Mouse

Eric Dolinar
*The University of Western Ontario*

Supervisor
Dr. Kathleen Hill
*The University of Western Ontario*

Graduate Program in Biology
A thesis submitted in partial fulfillment of the requirements for the degree in Master of Science

# Early Mechanisms of Retinal Degeneration in the *harlequin* Mouse

(Thesis Format: Monograph)

by

Eric A Dolinar

Graduate Program in Biology

A thesis submitted in partial fulfillment

of the requirements for the degree of

Master of Science

The School of Graduate and Postdoctoral Studies

The University of Western Ontario,

London, Ontario, Canada

## Abstract

Retinal diseases are personally debilitating and expensive, yet many early disease mechanisms leading to their onset and progression remain poorly understood. The *harlequin* mouse is a model of human mitochondrial dysfunction and parainflammation leading to subsequent cerebellar and retinal degeneration. Diagnosis of retinal degeneration can be tracked *in vivo* and is associated with AIF dysfunction. Here, retinal dysfunction in the *harlequin* mouse was first quantified using electroretinography followed by assay of blood-retinal-barrier integrity and transcriptome alterations in young adulthood. Nonmetric multidimensional scaling of oscillatory potentials provided a novel, comprehensive assessment of inner-retinal health and can detect shifts in OP parameters. Barrier integrity ruled out confounding exogenous antigens and confirmed an endogenous source of retinal tissue malfunction. In addition, transcriptome alterations support the necessity of the *hq* retina to maintain metabolic demands. Alternative metabolism pathways are hypothesized to be important for *hq* complex I mitochondrial-dysfunction associated retinal degeneration.



**Keywords:** *harlequin, Apoptosis-inducing factor,* retinal degeneration, mitochondrial dysfunction, electroretinography, oscillatory potentials, nonmetric multidimensional scaling, blood retina barrier, Evans Blue, ATP deficiency, quantitative gene expression, glycerol metabolism.

## Co-authorship Statement

Eric Ammon Dolinar performed the following work under the supervision and financial support of Dr. Kathleen Allen Hill. This thesis is presented in monographic format. Eric Ammon Dolinar performed the experimental research presented in this thesis and will be a co-author on resulting publications. Dr. Kathleen Hill will be a senior author on all publications produced from this research due to her role in project design, supervision, literature research, data analysis and assistance with publication writing. Alex Laliberté, Thomas MacPherson, Anita Prtenjaca, Anson Li and Dr. C.M.L Hutnik will be co-authors on specialized papers produced from the research due to assistance in experimental design, gene expression array data or electroretinography and clinical relevance.

## Acknowledgements

I would like to express my deepest appreciation and gratitude to all those who helped guide me through my Master's degree. First and foremost, I would like to thank my supervisor, Dr. Kathleen Hill who provided me with moral, academic, scientific and motivational support throughout the duration of my project. Her positive attitude, knowledge, patience, encouragement and attention were essential to the progression and completion of this final thesis. I would also like to thank Dr. Robert Cumming and Dr. Denis Maxwell for their continuous positive feedback, insight, and critical evaluation as advisory committee members.

In addition, I would like to acknowledge and show my appreciation to the staff at the LRGC, particularly David Carter, for his assistance and timely turnaround when I had projects that needed to be finished. I would like to thank all members of the Hill laboratory, past and present, for their technical assistance and friendship over the last two years. In particular, I would like to thank Anson Li for his willingness to work early mornings and late hours in order to assist me, as well as for his friendship outside of the lab. Finally I would like to thank my friends and family for their support and encouragement during all stages of my degree. A special thank you goes to my girlfriend, Marta Pajak and her family, for her unwavering support, patience, understanding and consolation that kept me grounded during stressful times.

Funding from the Plunkett Foundation, Canadian Glaucoma Society, Lawson Health Research Institute-Internal Research Fund, Canadian Institutes of Health Research, National Sciences and Engineering Research Council of Canada to Dr. Kathleen Hill supported the research in this thesis. Eric Dolinar was funded by an Ontario Graduate Scholarship and a travel award from the Department of Ophthalmology at Western University.

## Table of Contents

## List of Figures

## List of Tables

## List of Appendices

## List of Abbreviations

| | |
|---|---|
| *Adcy10* | *Adenylate cyclase 10* |
| ADP | Adenosine Diphosphate |
| AGEs | Advanced Glycation End-products |
| *Aif* | *Apoptosis-inducing factor* |
| *Aifm1* | *Apoptosis-inducing factor 1* |
| *Aldh2* | *Aldehyde dehydrogenase 2* |
| AMD | Age-related Macular Degeneration |
| ANOVA | Analysis of Variance |
| ATP | Adenosine Triphosphate |
| bp | base pair |
| BRB | Blood Retinal Barrier |
| $Ca^{2+}$ | Calcium Ion |
| cAMP | cyclic Adenosine Monophosphate |
| *Cdkn1a* | *Cyclin-dependent kinase inhibitor 1A* |
| cDNA | complementary Deoxyribonucleic Acid |
| cGMP | cyclic Guanosine Monophosphate |
| $CO_2$ | Carbon Dioxide |
| $ddH_2O$ | double-distilled water |
| DNA | Deoxyribonucleic Acid |
| DR | Diabetic Retinopathy |
| EB | Evans Blue Dye |
| ERG | Electroretinogram/Electroretinography |
| $FADH_2$ | Flavin Adenine Dinucleotide |

| | |
|---|---|
| FU | Fluorescence |
| G3P | Glycerol-3-Phosphate |
| G-protein | Guanosine nucleotide-binding protein |
| GABA | Gamma-Aminobutyric Acid |
| *Gapdh* | *Glyceraldehyde 3-phosphate dehydrogenase* |
| GCL | Ganglion Cell Layer |
| gDNA | genomic Deoxyribonucleic Acid |
| *Gk5* | *Glycerol Kinase 5* |
| *Glut4* | *Glucose transporter, member 4* |
| *Gpd2* | *Glycerol-3-phosphate dehydrogenase 2* |
| HCl | Hydrochloric Acid |
| $HCO_3^-$ | Bicarbonate Ion |
| *Hk1* | *Hexokinase 1* |
| HMGB1 | High Mobility Group Box 1 |
| *hq* | *harlequin* |
| *hq*X | Moderate disease *harlequin* female, heterozygote genotype |
| *hq*Y | Severe disease *harlequin* male, hemizygous genotype |
| INL | Inner Nuclear Layer |
| IPL | Inner Plexiform Layer |
| IS | Inner Segment (Photoreceptors) |
| ISCEV | International Society for Clinical Electrophysiology of Vision |
| $K^+$ | Potassium Ion |
| kb | kilobase |
| *Ldhc* | *Lactate dehydrogenase C* |
| *Mct* | *Monocarboxylate Transporters* |

| | |
|---|---|
| mRNA | messenger Ribonucleic Acid |
| $Na^+$ | Sodium Ion |
| NAD+ | Nicotinamide Adenine Dinucleotide |
| NaOH | Sodium Hydroxide |
| NC | No DNA Control |
| NMDS | Nonmetric Multidimensional Scaling |
| nt | nucleotide |
| NTC | No Template Control |
| OAG | Open-angle Glaucoma |
| ONL | Outer Nuclear Layer |
| OP | Oscillatory Potentials |
| OPL | Outer Plexiform Layer |
| OS | Outer Segment (Photoreceptors) |
| OXPHOS | Oxidative Phosphorylation |
| PAMPS | Pathogen-Associated Molecular Patterns |
| PBS | Phosphate Buffered Saline |
| PCR | Polymerase Chain Reaction |
| *Pdhx* | *Pyruvate dehydrogenase, component X* |
| *Pfkfb3* | *Phosphofructose-2-kinase/fructose-2,6-bisphosphatase-3* |
| PRP | Pattern Recognition Receptors |
| qPCR | quantitative Polymerase Chain Reaction |
| RAGEs | Receptor for Advanced Glycation End-products |
| RIN | Ribonucleic Acid Integrity Number |
| *Rn18s* | *18S Ribosomal subunit* |
| RNA | Ribonucleic Acid |

| | |
|---|---|
| ROS | Reactive Oxygen Species |
| RPE | Retinal Pigmented Epithelium |
| rRNA | ribosomal RNA |
| *Samd4* | *Sterile alpha motif domain containing 4* |
| *Scn4b* | *Sodium channel beta 4 subunit* |
| *Sdk2* | *Sidekick-2* |
| *Slc4a10* | *Sodium bicarbonate transporter, member 10* |
| STD | Size Standard |
| *Tbc1d4* | *TBC1 domain family, member 4* |
| TCA cycle | Tricarboxylic Acid cycle |
| TNFα | Tumor Necrosis Factor *alpha* |
| VEGF | Vascular Endothelial Growth Factor |
| WT | Wild Type, specifically XY |
| $X^{hq}X$ | *harlequin* Heterozygous Disease Mouse |
| $X^{hq}X^{hq}$ | *harlequin* Homozygous Disease Mouse |
| $X^{hq}Y$ | *harlequin* Hemizygous Disease Mouse |

# Chapter 1. Introduction

## *1.1 Increased prevalence of neurodegenerative disorders in an increasingly aged population*

Neurodegenerative diseases are characterized by progressive functional deficiencies and cell death of neurons resulting in nervous system dysfunction. Medical advances in cardiovascular diseases, cancers and other common illnesses have increased human longevity and thereby increased prevalence of neurodegenerative disorders.[1] Predispositions from familial and environmental risk factors may also play a role in neurodegenerative disease onset and progression, however, the highest propensity of disease risk occurs with age.[2] Despite high prevalence and extreme negative consequences to quality of life, the causes and early disease mechanisms of such diseases remain unknown.

In Canada, it is expected that within 25 years the number of seniors will double to well over 9.9 million people and surpass the age demographic of 0-14 year olds for the first time in Canadian history (Population Projections for Canada, Provinces and Territories. 2009-2036).[3] Common retinal degenerative diseases such as: age-related macular degeneration (AMD), diabetic retinopathy (DR) and open-angle glaucoma (OAG) affect well over 1.75 million Canadians and the prevalence of such diseases is expected to rise proportionally (CNIB Report, 2009).[4] These three diseases fall under the umbrella term of "vision loss" and have the highest direct healthcare costs of any disease in Canada at $8.6 billion annually.[4] Despite this high level of expenditure, little is known about early disease mechanisms and prevention leaving the diseases personally debilitating and expensive. Vision research remains critical for increasing the quality of

life of affected individuals and also for reducing expenditures as the increasingly aged population brings alarming financial demands.

### *1.2 Mechanisms of common retinal degenerative diseases remain unclear*

As the Canadian population shifts towards an older demographic cohort, the prevalence of common retinal degenerative disorders is expected to rise.[4] These common diseases are progressive and require continual and enhanced treatment as the disease advances. Retinal degenerative disorders can lead to losses of central, peripheral, and even complete vision in the later stages of disease progression. Unfortunately, disease mechanisms and triggers leading to neuronal death are numerous and little is known about initiating mechanisms that cause retinal degeneration.

Age-related macular degeneration (AMD) is a prevalent retinal degenerative disorder affecting over one million Canadians and is the leading cause of irreversible blindness in the developed world.[4,5] AMD begins with the deposition of acellular protein and lipid debris, known as drusen, in the space behind the retina around the macula.[6] The macula contains the highest density of cone photoreceptors in the primate eye and is responsible for the central vision acuity that we appreciate as human beings.[7] Excess drusen can cause damage to the retina and lead to hypoxia. Hypoxia induces the expression of angiogenic cytokines, such as vascular endothelial growth factor (VEGF), causing neovascularization in the macula and leading to subsequent central vision loss.[5]

Diabetic retinopathy (DR) is the second-most prevalent retinal degenerative disorder affecting over 500,000 Canadians.[4] It is a common complication of diabetes caused by hyperglycemia, hypoxia and neovascularization.[8] The exact mechanisms by

which DR causes neovascularization and progressive retinal degeneration remain poorly understood.

Open-angle glaucoma (OAG) is the third-most prevalent retinal degenerative disorder affecting over 250,000 Canadians.[4] Glaucoma is often caused by an increase in intraocular pressure leading to optic neuropathy.[4] Increases in intraocular pressure caused by reduced aqueous humor drainage lead to progressive retinal neuron axon loss, particularly along the optic nerve.[9] Mechanisms that drive retinal cell loss remain unknown and lead to peripheral vision loss with no preventative treatment available.[10]

The progressive symptoms associated with these common retinal degenerative diseases are clearly characterized and various treatments are available in the later advancements of the disease. However, early mechanisms and triggers leading to retinal degenerative disorders are poorly understood and treatment is only available after cell damage has already begun. Therefore, to increase the quality of life, an understanding of early disease mechanisms is critical to limit disease onset and progression.

### *1.3 The physiology and anatomy of a healthy retina is complex*

The retina is one of the most complex structures of the vertebrate eye and a key component of the visual pathway (Figure 1.1A). The retina is a light-sensitive tissue that lies in the posterior region of the vertebrate eye and is divided into two regions known as the neural retinal and retinal pigmented epithelium (RPE) (Figure 1.1B).[7] These two anatomical regions develop from the embryonic forebrain and undergo complex differentiation and ultimately function as an outcropping of the central nervous system.[11]

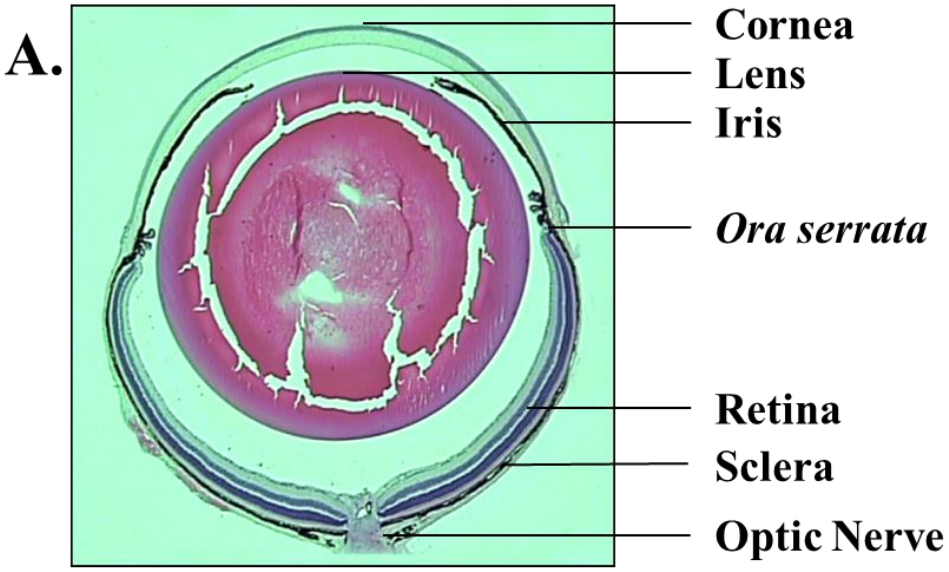
A.
Cornea
Lens
Iris
Ora serrata
Retina
Sclera
Optic Nerve

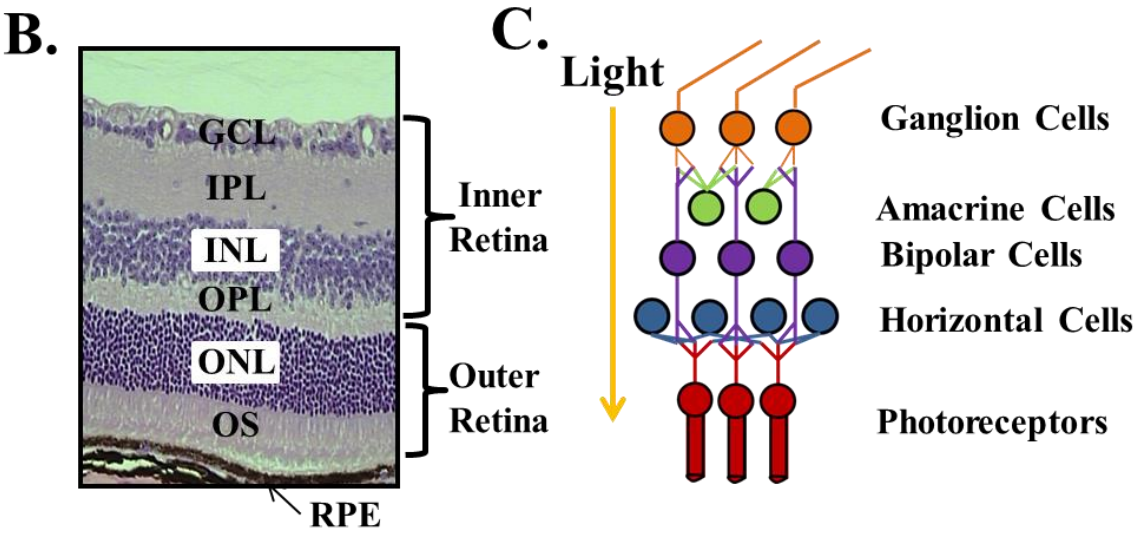
B.
GCL
IPL
INL
OPL
ONL
OS
RPE
Inner Retina
Outer Retina
C.
Light
Ganglion Cells
Amacrine Cells
Bipolar Cells
Horizontal Cells
Photoreceptors

**Figure 1.1 A cross-section of the mouse eye and retina stained with Hemotoxylin and Eosin.** (A) A C-cut section of the mouse eye demonstrates similar anatomical features of the human eye including the cornea, lens, pupil, iris, retina, scalera and optic nerve. Representative wild-type mouse eye adapted from MacPherson (2009).[19] (B,C) A cross-section of the mouse retina indicates the distinct retinal cells layers. Light must transverse all layers of the retina prior to excitation of the photoreceptors which are positioned in the outer segment (OS). The retinal pigment epithelium (RPE) lies at the base of the retina and absorbs any stray photons of light not absorbed by photoreceptors. In addition, the RPE separates the retina from the posterior choroid and acts as a nutrient shuttle. Phototransduction begins in the OS as the electrochemical signal is conveyed through the outer nuclear layer (ONL) and synapses through the outer plexiform layer (OPL) onto the horizontal cells and bipolar cells of the inner nuclear layer (INL). The electrochemical signal is then relayed to the amacrine and ganglion cells of the ganglion cell layer (GCL) through the inner plexiform layer (IPL). The electrochemical signal leaves the GCL via the optic nerve where it is transmitted to the visual cortex for interpretation.

The design of the mammalian retina is counter-intuitive in nature because light must cross all neural retinal layers prior to the excitation of photoreceptors. Thereby, photoreceptors are positioned at the most posterior region of the neural retina, only posteriorly superseded by the RPE (Figure 1.1B).[12] This is due to the fact that the RPE continuously supplies nutrients to the highly metabolic photoreceptors.[11] The RPE is a monolayer of pigmented cells that separates the internal choroid from the neural retina and acts as a nutrient shuttle, providing a steady stream of 11-*cis* retinal, glucose, and fatty acids from the choroid to the outer segment of the photoreceptors.[13–15] The RPE also plays an essential role in the recycling of all-*trans* retinal back into 11-*cis* retinal once it has been isomerized by light.[14,13] The RPE is highly pigmented, containing a high proportion of melanin granules that absorb stray photons of light in the retina to enhance vision acuity and reduce exposure to light radiation.[7] In addition, the RPE creates an outer blood-retinal-barrier (BRB) through epithelium tight junctions which maintains optimal homeostatic conditions for retinal neurons.[15]

Anterior to the RPE lies the neural retina composed of six differentiated layers (posterior to anterior) (Figure 1.1B,C). The outer segment (OS) contains the familiar rod and cone photoreceptors responsible for the initial absorption of light and relay of electrochemical signal.[7] All vertebrate retinas contain both rod and cone photoreceptors which differ by their absorption wavelength and cell morphology. Rods are thin, rod-shaped structures that are highly sensitive to blue-green light (500 nm) and are densely packed with the visual surface photopigment rhodopsin. Rods are generally used for low-light vision (scotopic vision) and make up 95-97% of all photoreceptors in the mammalian eye (human 95%).[7,16] Cones are large, conical structures that are densely

packed with opsin photopigments and are sensitive to daylight and bright colours (photopic vision). Three types of cones with different associated opsin photopigments exist in the human retina, each responsible for the absorption of a different wavelength of light: red (559 nm), green (431 nm) or blue (419 nm).[16] This provides the trichromatic vision that we appreciate as humans. The inner segment (IS) contains the cell bodies of the photoreceptors and is responsible for maintaining metabolism.[16] In the outer nuclear layer (ONL) lie the nuclei of the photoreceptors. The outer plexiform layer (OPL) is a thin region of synaptic connections between the photoreceptors and the neural cells of the inner nuclear layer (INL). The outer plexiform layer (OPL) is a region densely populated with axons from the rod and cone photoreceptors and neurites of bipolar and horizontal cells.[11] Eleven types of human bipolar cells exist in the INL, the most common being bipolar cells connecting photoreceptors with ganglion cells through the release of glutamate.[11] Horizontal cells have a large lateral extension across the retina and synapse back onto rod and cone photoreceptors in an inhibitory manner.[17] This provides a level of local gain in the retina and allows image processing to begin through inhibiting light-saturated photoreceptors to prevent scattering of light in the retina.[18] The INL also contains the nuclei of amacrine cells which mediate the effect of the ON-,OFF- bipolar cells on ganglion cells through the release of neurotransmitters, glycine and gamma-aminobutyric acid (GABA).[18] These mechanisms assist with the early building of images in the retina.[7] Synapsis of bipolar and amacrine with ganglion neurons occurs in the inner plexiform layer (IPL). The innermost layer of the retina is the ganglion cell layer (GCL) which contains both the axons and nuclei of the ganglion cells and is responsible for relaying electrochemical signals to the visual cortex via the optic nerve.

### *1.4 Phototransduction is compromised in retinal degeneration*

Phototransduction is the process in which photons of light excite photopigments in the photoreceptor cells to generate an electrical response.[20] First, light must travel through all layers of the retina and will only activate photoreceptors in the field of reference. In rod photoreceptors, rhodopsin is the primary photopigment and is covalently linked to the chromophore, 11-*cis* retinal.[21] During the absorption of light, 11-*cis* retinal is converted to all-*trans* retinal through photoisomerization.[20] Conformational changes of rhodopsin are capable of activating photoreceptor-specific G-protein, transducin.[20] Transducin stimulates the activity of cGMP phosphodiesterase, resulting in a reduction of cytoplasmic cGMP concentration and subsequent closure of cGMP gated channels.[22] Closure of the cGMP channels results in a decrease of $Na^+$ and $Ca^{2+}$ influx triggering membrane hyperpolarization and reduced release of synaptic neurotransmitter, glutamate.[20] Glutamate is the principal neurotransmitter involved in electrochemical transmission in the retina.[7] Unlike common nerve cell function, photoreceptors release glutamate in the dark as $Na^+$ and $Ca^{2+}$ flow freely across the phospholipid membrane.[20] Upon light stimulus, glutamate release is hindered in photoreceptors and leads to subsequent depolarization of bipolar, horizontal and amacrine cells of the INL.[22] This signal is further processed by the GCL before travelling to the visual cortex via the optic nerve. Phototransduction occurs in a similar fashion in cone photoreceptors, however, opsin proteins vary slightly in their optimal absorption wavelength. Phototransduction is imperative to normal retinal function and vision. Common retinal degenerative diseases can lead to damage of the photoreceptors and phototransduction pathway by various

disease factors including: age, light toxicity, diabetes, hypertension, genetic mutations, vitamin A deficiency, angiogenesis, parainflammation and mitochondrial dysfunction.[23,24]

### *1.5 Neuronal homeostasis is maintained by glial cells of the retina*

Three types of resident glial cells reside in the retina and are essential for retinal function and homeostasis, these include Müller cells, astroglia, and microglia cells. Müller cells are the most abundant glia of the retina and provide architectural support across all neural layers.[25] Müller cell bodies sit in the INL and perform a variety of functions including: the breakdown of glycogen for anaerobic metabolism,[26] removal of excess neurotransmitters from the subretinal space,[27] assistance with phagocytosis of apoptotic neurons and neuronal debris,[28] assistance with the formation of the BRB[29] as well as maintaining ionic homeostasis in the retina by recycling $K^+$.[30] Astroglia are the supportive glia that originate in the optic nerve head and are subsequently present in the GCL.[31,32] Similar to Müller cells, they assist with the formation of barrier properties by vascular endothelial cells,[29,33,34] the breakdown of glycogen for neuron nutritive support,[26] and regulation of ionic homeostasis[30] as well as GABA metabolism.[25] The resident macrophage of the retina is the microglial cell. The retina is a region of immune privilege protected by the BRB to hinder the movement of pathogens and microbes into the highly sensitive neural retina. Microglia cells act as part of the innate immune system and partake in immune surveillance[35], neuronal support[36] and phagocytosis of cellular debris and pathogens.[37] Under necrotic or apoptotic pathways, cellular debris such as ATP, uric acid and other alarmins are released and stimulate the innate immune system.[38]

Microglial cells become activated and elicit an inflammation response to clear cytotoxic debris from the retina. Together, these three types of glial cells all play a vital and distinct role in the retina to maintain homeostasis and proper retinal function.

### *1.6 Retinal neurons rely heavily of oxidative phosphorylation for ATP generation*

Neurons of the retina require high amounts of ATP to maintain ionic potentials through the active transport of $Na^+$ influx and $K^+$ efflux by $Na^+K^+$ATPases.[39] In addition, the continuous recycling of neurotransmitters places additional metabolic pressure on the cell.[40] Neurons do not store glycogen and suppress the enzymatic machinery to synthesize glycogen and therefore rely on the constant flow of oxygen and glucose from the vasculature in order to maintain their high metabolic rate.[41,42] Dendrites, regions of frequent membrane hyperpolarizations/depolarizations and ion mobility, are the most energetically consuming region of the neuron. Consistent with their great metabolic rate, neurons rely heavily on glucose oxidative phosphorylation (OXPHOS) for ATP production.[43–45] Glial cells, on the other hand, are highly glycolytic. In addition, glia also have the ability to store glycogen and convert it to glucose 6-phosphate when glucose supply to the retina is diminished.[44] Glial cells can provide lactate and other metabolites to the neurons of the retina via Monocarboxylate transporters (MCT) when glucose supply is diminished.[40]

### *1.7 Nourishment in the retina is maintained by a healthy blood-retinal-barrier*

Glucose is supplied to the retina through the choroid (located posterior to the RPE) and the retinal capillaries.[7] Glucose must first traverse the epithelial barrier of the RPE (outer BRB) or the retinal capillary endothelial vasculature (inner BRB) which controls the exchange of metabolites and waste products between the vasculature and neural retina.[46] The inner BRB supplies nutrients and oxygen to the ONL, INL, and GCL, whereas the outer BRB is responsible for neuronal support of the inner and outer segments of the photoreceptors.[46] Pericytes surround the endothelial cells and secrete angiopoietin 1 to induce tight junction protein expression.[47] Both the inner and outer BRB develop junctional complexes between the vascular endothelial/epithelial cells to allow limited movement of ions and solutes into the neural retina.[46,48] Tight junctions are made up of transmembrane proteins known as, claudins, occludin and the junctional adhesion molecules which are linked to the cytoskeleton of the adjacent cells.[46] Tight junctions lead to the fusion of two adjacent endothelial or epithelial cells and limit intracellular space to reduce diffusion of ions, pathogens, lipids, proteins, reactive oxygen species (ROS) and foreign substances into the sensitive neuronal space. Epithelial cells of the RPE act as a regulatory interphase between the choroid and outer retina. The basal surface of the RPE contains many invaginations to enhance selective transport and secretion along the vasculature.[15] Due to the continual active transport of substrates across the RPE and vasculature barrier, cells are highly metabolic and subsequently require high levels of ATP to maintain efficient transport. The endothelial/epithelial structure of the BRB is considered to be the first line of defence to protect the neural retina from invasion of pathogens as they can engulf foreign antigens.[15] In addition,

epithelial cells of the RPE can excrete various cytokines to initiate an inflammatory response.[49] Dysfunctions of the BRB are associated with DR as the dysfunction leads to pathological changes such as chronic inflammation and hypoxia triggering retinopathy progression.[50,51] In addition, the outer BRB harbours the choroid vasculature and limits neovascularization in the retina. A loss of integrity also leads to AMD and subsequent vision loss.

### *1.8 Electrophysiological examination can assess health of the visual system in vivo*

Electroretinography can be used to assess the integrity of phototransduction in the retina. The electroretinogram (ERG) is a massed, retinal response measured by corneal electrodes following a light stimulation. The major components of the ERG include, the a-wave and the b-wave with high-frequency oscillations known as oscillatory potentials (OP) on the ascending limb of the b-wave (Figure 1.2).[11] The initial output wave, known as the a-wave, is associated with photoreceptor hyperpolarization.[52] The secondary wave, known as the b-wave, is associated with the depolarization of bipolar cells and Müller cells.[53] The exact origin of the oscillatory potentials remains unknown, although they are believed to be generated by interactions between amacrine, bipolar and ganglion cells.[54–56] Electroretinography can be used to assess the function of both rod- and cone-based systems. "Dark-adaptation" of the subject prior to the assay will result in rod hyperpolarization following a light stimulus.[57] "Light-adaptation" of the subject prior to the assay will result in hyperpolarization of the cone photoreceptors as the rods will be saturated.[57] Electroretinography performed under scotopic conditions assesses the functionality of rod photoreceptors and can be used to examine the inner retinal pathways

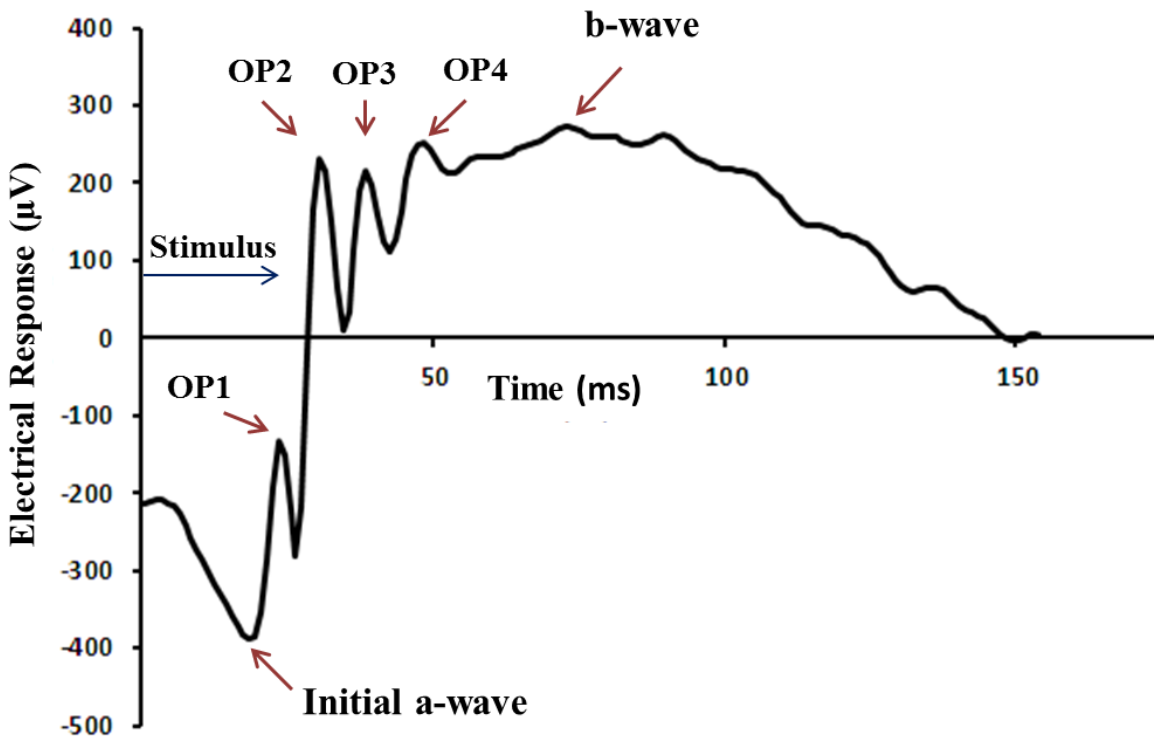
b-wave
OP2
OP3
OP4
400
300
200
100
0
-100
-200
-300
-400
-500
Electrical Response (µV)
Stimulus
OP1
50
Time (ms)
100
150
Initial a-wave

**Figure 1.2. A schematic representation of a trace electroretinogram elicited by a healthy, dark-adapted mouse retina following a light stimulus of 30 cd•s/m$^2$ (Flash 11).** All major characteristic components of the electroretinogram are evident. The a-wave represents the initial hyperpolarization of the photoreceptors and is the initial negative deflection. This is followed by the intermediate oscillatory potentials (OP) peaks 1-4 (OP1, OP2, OP3, OP4) on the ascending limb of the b-wave. It is apparent that early OP peaks are correlated with the function of the photoreceptors whereas late OP peaks are indicative of ganglion and amacrine negative feedback in the outer retina.[56] The final component, the b-wave, represents the depolarization of the bipolar and Müller cells, and is the cumulative response of the retina.

and mechanisms rods initiate. Since the mouse retina is composed of well over 97% rods [58] ERGs performed under scotopic conditions provide a more general, comprehensive analysis of retinal function and health. The ERG provides the only non-invasive, *in vivo*, diagnostic tool that can be used to quantify retinal health by testing functionality of photoreceptors and neural cells of the retina.

### *1.9 Oscillatory potentials can provide early in vivo examination of INL and GCL function*

Oscillatory potentials (OPs) are the low amplitude, high-frequency oscillations that are found on the ascending limb of the b-wave.[11] The exact origin of OPs remains unknown and their interpretation remains difficult, however attritional changes are associated with diseases of the retina particularly retinopathy and retinal degeneration. Early OPs are believed to be associated with the hyperpolarization of the photoreceptors and intermediate OPs with action-potential (graded) independent neurons such as horizontal cells and bipolar cells.[56] Later OPs however, are associated with more proximal retinal responses, that of action-potential dependent mechanisms of amacrine and ganglion cells.[56] Due to the fact that OPs appear as oscillations on the leading edge of the b-wave, it has been suggested that OPs may be the result of neurons with large lateral mobility in the IPL i.e. amacrine cells.[54,59] Additionally, the interplexiform cell which spans the OPL and IPL may also generate radial current (feedback) from lateral synapses and may be responsible for the oscillations.[54,55] OPs have been used previously, to study the function of the inner retina and have been useful in the diagnosis of a variety of progressive retinal eye diseases including; increased intraocular pressure, diabetic

retinopathy, retinal vascular occlusions, and retinopathy of prematurity.[59–66] OPs have been useful in the diagnosis of DR prior to any structural cell loss or ocular symptoms in both human and animal models.[59,62,65] Therefore OPs can be used as a versatile, disease tracking, diagnostic tool prior to any structural and noticeable changes.

There is little consensus on the most appropriate method for extracting oscillatory potentials from the ERG. Signal conditioning is the first step that must be performed for isolation of OPs from the ERG trace. Current recommendations set by the International Society for Clinical Electrophysiology of Vision (ISCEV) suggest a simple band-pass filter applied at 75 to 300 Hz to remove any a-wave contribution or high-frequency noise.[67] In mice, these cut-offs discard most of the rod-driven OPs and are therefore rarely followed.[68–70] The most common method of OP isolation involves a pre-conditioning waveform to remove any photoreceptor contribution[68,71–74] followed by a fifth order Butterworth transformation with a band-pass of 65 to 300 Hz (Figure 2.2).[68–70,75] The amplitude and latency of each OP wavelet can be analyzed individually or as a sum in the time domain; or through a fast Fourier transform in the frequency domain.

The underlying goal of any OP examination is to surmise physiological origins of the parameters or to identify a clinically relevant, diagnostic parameter that may infer disease mechanisms prior to disease onset.[76] In the time domain (Figure 2.3), analysis of individual OP amplitudes is advantageous because the amplitudes offer implicit information about associated retinal regions given retinal layers and signal transduction through the retina.[60] Summed amplitude of all OPs encompasses a full inner retinal response of the INL and GCL. Initial latency is a measure of synapsis timing and periodicity of the INL/GCL retinal response.[77] Decreases in both OP summed amplitude

and initial latencies have found in retinopathy,[66,78,79] diabetic retinopathy,[63,65] and glaucoma.[61] The time domain analysis of OPs contains relevant information in regards to individual components and mechanisms occurring in the retina, however until an exact understanding of OP generation is established only qualitative interpretations can infer disease. The frequency domain (Figure 2.3) analysis of the extracted OP waveform following application of a fast Fourier transform is advantageous because it provides a holistic examination of the OP waveform, particularly when signal-to-noise ratio is low.[66,76] In addition, the frequency domain analysis is much more objective as it does not require the subjective identification of individual OPs which may become troublesome when signal response is low or noise is high.[80] Since both time- and frequency-domain analysis provide distinct information about OP parameters and general health of the retina, they were both examined in our investigation to identify an early diagnostic feature of retinal degeneration.

### *1.10 Nonmetric multidimensional scaling as a method for understanding OP waveform changes*

In general, the mammalian ERG contains five OP wavelets existing on the leading edge of the b-wave, each with its own characteristic period (latency) and amplitude.[54] OP profiles depend on the intensity of the light stimulus, with increasing intensity leading to increased OP amplitude and decreased latency until retinal phototransduction saturation occurs.[66,74,78] Examination of the OPs occurs following a single high-intensity flash and subsequent comparisons of latencies and amplitudes of each OP between a disease model and a healthy control. In addition, summed OP amplitude is useful for understanding

whole retinal response in the time domain.[76,78] Examination of OPs at a single flash-intensity has limitations since it may not be useful for understanding complete waveform changes across multiple stimuli intensities where disease mechanisms may be evident in retinal neurons only activated under low light intensity. The frequency domain provides a much more holistic approach to whole OP waveform interpretation; however, similar to the time domain, this approach can only be examined at a single flash intensity to examine differences in frequency, power, and energy between a disease model and a healthy control.[66,80,81]

To understand whole OP waveform changes, a comprehensive nonmetric multidimensional scaling (NMDS) of OP parameters across multiple flash intensities can be applied. NMDS is a monotonic, numeric, ordination technique that involves spatial representation of observed variables to fitted distances.[82–84] The method involves the assignment of derived coordinates for every sample and mandates that rank order may not be changed but observed proximities can be adjusted.[82–84] In this way, many variables can be examined for each sample and modelled into a previously selected explicit number of axes, provided that the original rank order is not changed.[82] Stress is a measure of how well the ordination fits the observed distances among samples and the error associated with modelling.[85] Stress increases with the number of samples and the number of variables fit into the ordination.

### *1.11 Mitochondrial dysfunction is a common theme in retinal degeneration*

The mitochondrion is the organelle responsible for oxidative phosphorylation (OXPHOS). In highly metabolic tissues, the density of mitochondria tends to be much higher to keep up with the energetic demands of the cell.[86] The visual pathway is amongst the most energetically demanding processes in the body, as it requires continual movement of ions across membranes for maintenance of resting potentials in addition to the continual recycling of neurotransmitters.[87,40] Due to the persistent energetic demands of the retina, it has the highest relative oxygen consumption of any tissue in the body, necessary to facilitate OXPHOS.[88,89] Therefore, adequate and consistent delivery of oxygen is vital to retinal homeostasis and any deviations can lead to mitochondrial dysfunction and subsequent oxidative stress. Mitochondrial dysfunction is a common theme in retinal degenerative diseases and has been implicated in AMD, OAG, and DR due to oxidative damage of photoreceptors.[90]

### *1.12 The mouse is a valuable model organism for vision research*

The use of animal models continues to be vital as an ethical means to investigate fundamental biological principles. Mouse models are amongst the most common due to their short life cycle, quick sexual maturity, large litter size, and similar physiological and genetic composition to humans.[91] In addition, isogenic, inbred strains reduce variation amongst individuals and allow complex diseases to be studied with smaller sample sizes while achieving higher power to detect significant differnces.[11] Many similarities exist between the human and mouse eye; including a large cornea and lens' as well as

analogous retinal nerve layer physiologies and cell types.[92] The mouse retina is quite similar to the human retina with only minor differences in the visual pathway. For example, mice have a higher proportion of rod photoreceptors (over 97%)[58] which makes their retinas much more effective in scotopic light. Another major difference is the presence of a macula in the human retina. The macula is a dense, cone-rich area in the central region of the retina responsible for central vision acuity.[7] In mice this is replaced with a central region of highly concentrated rod photoreceptors.[58] While humans possess three types of cone photoreceptors, mice only have two; green- and blue-sensitive.[7] This property, although a major difference, assists researchers because mouse "dark-adapted" experiments can be performed in red-light. While subtle differences do exist between the mouse and human retina, common physiologies, genetics and cell types as well as the progression of similar diseases make mice an excellent mimic for human retinal disease mechanisms and subsequently vision research.[92]

### *1.13 The harlequin (hq) mouse is a model of mitochondrial dysfunction and neurodegenerative disease*

The *harlequin* (*hq*) mouse ($X^{hq}X^{hq}$, $X^{hq}Y$ or $X^{hq}X$) is a model of mitochondrial dysfunction associated with neurodegenerative disease of the retina and cerebellum.[93] The term "*hq*" refers to the *hq*Y genotype unless otherwise specified. Characteristic markers of the *hq* phenotype include; low body mass, a patchy coat, ataxia, low subcutaneous fat reserves as well as characteristic retinal and cerebellar degeneration.[93] These phenotypic characteristics are the result of a spontaneous proviral insertion into

intron 1 of the X-linked *Apoptosis-inducing factor* (*Aif*) gene which encodes a mitochondrial flavin adenine dinucleotide-dependent oxidoreductase.[94] Since the proviral insertion is in a suspected regulatory region of intron 1, there is an overall global downregulation of AIF by nearly 80% in most tissues.[93]

As described previously, *AIF* is located on the human X-chromosome in the Xq25-26 region.[94] The gene is syntenic in the mouse and is also located on the X-chromosome in the A6 region.[94] The AIF amino acid sequence is highly conserved in both organisms, sharing 92% sequence homology of the active domain as well as an amino-terminal mitochondrial-localization sequence.[94] Upon translocation to the intermembraneous space of the mitochondrion, the localization sequence is cleaved leaving a functional 57 kDa flavoprotein.[94] AIF is ubiquitously expressed across most tissues in mice[95] with demonstrated embryonic lethality at day 9 in a complete *Aif* mouse knockout.[96] This indicates AIF's vital role in development as well as cell life and death.

The function of AIF was first characterized as a mitochondrial bound caspase-independent death effector protein that translocates to the nucleus and aids with chromatin condensation and DNA fragmentation when apoptosis is induced.[94,97] However, recent investigations have led to the description of multiple functions of AIF. AIF's primary role *in vivo* may be linked to OXPHOS efficiency, particularly that of NADH dehydrogenase (complex I). *Aif*-knockdowns have displayed limited formation of complex I *in vivo* indicating its role in maintenance and facilitation of complex I formation.[98] *hq* mice have an overall decrease in mitochondrial complex I efficiency, particularly that of the retina (~30% of normal function) and brain (~60% of normal function).[95] Although *Aif* causes a decrease in complex I function, no changes in the

transcriptome or proteome indicate dysfunction of complex I subunits post-translationally.[98] Further analysis of AIF indicates that it shares sequence similarities[94] and similar crystal structure[99,100] with bacterial oxidoreductases and may function as a mitochondrial scavenger of free-radicals including ROS. *hq* mice demonstrate elevated oxidative stress in dying neurons of the retina and cerebellum.[93] However, this function of AIF remains controversial because mitochondria isolated from brain of *hq* mice show no traces of increased ROS production as a result of *Aif* deficiency.[101]

### *1.14 Timeline of the hq disease progression*

Since *Aif* is mapped to the X-chromosome, affected *hq* males are hemizygous for the proviral insertion. Females can either be homozygous or heterozygous for the proviral insertion. Homozygous females demonstrate a severe, early-onset disease phenotype, similar to that of hemizygous males.[93] Heterozygous females however, show delayed onset, moderate disease progression and moderate disease phenotype,[102,103] likely due to random X-inactivation.

The progression of the *hq* disease (homozygous and hemizygous) is well characterized in both the retina and the cerebellum. The *hq* disease is an ageing-associated retinal degeneration with primary structural losses occurring as early as three months of age in amacrine and ganglion cells.[93] The progression of the *hq* disease is quite rapid with histological analysis indicating significant losses in the INL and ONL by four months of age.[19,93] Examination of the IPL and OPL in the *hq* retina indicate losses of neurites, particularly that of dendrites.[93] Functional deficits precede structural losses in

the *hq* retina with electroretinography showing rapid functional deficits in ERG a-wave amplitudes at three months and b-wave at two months of age.[19] By ten months of age, *hq* mice elicit no functional response of the retina.[93] Physiological changes begin as early as 1.8 months in the *hq* retina, consistent with a loss of homeostasis and activation of microglial cells in the IPL[104]. This is indicative of an inflammatory response and may contribute to the early structural and functional losses observed. Chronic activation of microglial cells continues through *hq* disease progression and leads to microglial migration into the ONL and GCL by four months of age, consistent with cell losses observed previously.[93,104]

The degeneration of the *hq* cerebellum occurs with a much slower progression in comparison to the retina.[102] Early histological analysis indicates apoptosis in the *hq* cerebellum as early as four months of age in granule cell nuclei leading to smaller total cerebella by seven months.[93,105] Loss of over 50% of granule cells was observed by twelve months of age.[93] Purkinje cell loss in the *hq* cerebellum occurs later in comparison to granule cell loss initiating at seven months of age.[93,105] Characteristic markers of microglia activation in the *hq* cerebellum have yet to be tracked *in situ*.

### *1.15 Deficiencies in OXPHOS lead to neuronal malfunction and ATP deficiencies*

It is well established that OXPHOS is the major source of ATP for all cells, in particular neuronal cells of the brain and retina. Energetic failure of OXPHOS in neuronal cells has been linked with Alzheimer's disease,[106] Parkinson's disease,[107] Huntington's disease,[108] amyotrophic lateral sclerosis[109] and other neurodegenerative

disorders. Neuronal cells maintain consistent internal ATP concentrations and minimal energy gradients by axonally transporting mitochondria via microtubules to regions of high energy consumption.[110] The presynaptic compartment of the neuron, responsible for neurotransmitter release, is the region of highest energy consumption.[110,111] High amounts of ATP are required for continuous neurotransmitter recycling as well as ion pumping to maintain membrane potentials.[111] Deficiencies in OXPHOS particularly affect the presynaptic cleft and other highly metabolic regions leading to neurite loss and synaptic degeneration.[111,112]

In addition to being "the powerhouse of the cell," the mitochondrion is also an intracellular regulator of calcium. Mitochondrial dysfunction as a result of OXPHOS deficiency causes mitochondrial overload of $Ca^{2+}$, leading to opening of the mitochondrial permeability transition pore and $Ca^{2+}$ release.[113,114] This furthers induces ATP deficiency, successive glycolytic ATP dependency, reduced mitochondrial mobility, release of ROS and subsequent activation of the caspase execution cascade leading to apoptosis and cell death in the tissue.[114–116]

### *1.16 OXPHOS deficiencies in the hq mouse*

The variability associated with the *hq* disease phenotype is large, with timing of disease onset and progression occurring differently across individuals.[95] Additionally, the effect of the *Aif* proviral insertion is also not equivalent across tissues of the *hq* mouse. Western blotting reveals that AIF expression in *hq* mice, in comparison to controls, was approximately 20-40% in the cerebellum, spinal cord, cortex, skeletal muscle, and

kidney.[95] AIF reaches almost 60% expression levels in the liver, with minimal to nil expression in the retina.[95]

In association with decreased AIF expression, compromised OXPHOS efficiency was found in all regions of the brain and retina however no OXPHOS deficiency was evident in the heart or the liver.[98] A complete knockout of *Aif* in the mouse heart does however lead to reduced OXPHOS activity indicating the buffering threshold of the *Aif* knockout may be organ specific.[117] Tissue specific *Aif* knockout for liver, muscle and heart leads to increased glucose uptake (via *glucose transporter 1* and *4)* as well as a reduction in overall ATP levels and high NADH/NAD+ ratios and lactate production. This suggests the switch towards glycolytic metabolism and generation of anaerobic ATP.[117,118] In addition, *hq* mice demonstrate similar characteristics of increased insulin sensitivity and glucose uptake/tolerance with reduced predisposition to obesity on a high fat diet.[118]

The complete *Aif* knockout in embryonic stem cells identifies consistent consequences leading to high levels of lactate production.[98] The addition of 2-D-deoxyglucose, an inhibitor of glycolysis, increases apoptosis in these *Aif*-deficient embryonic stem cells and indicates high dependency on glycolytic ATP and glucose as a primary metabolite.[98] Taken together, this thorough examination of AIF dysfunction indicates a metabolic change towards anaerobic and lactate ATP production in *Aif*-deficient cells particularly in tissues of mesodermal and ectodermal origin.

The knockout or knockdown of *Aif* predisposes embryonic stem cells, muscle, liver and heart cells to mitochondrial OXPHOS deficiency and reduces overall ATP

generation. *Aif*–deficient cells must compensate and switch their metabolic processes towards a glycolytic pathway of ATP production and promote high glucose uptake and metabolism. Glycolysis is the conversion of a glucose molecule into pyruvate in a 1:2 ratio with the reduction of two $NAD^+$ molecules to NADH and the net overall production of two ATP molecules. The switch to glycolysis allows for ATP production when OXPHOS is an inefficient source of energy production and provides the necessary energy for metabolic need. Unlike other cell types and tissues, glycolysis is intrinsically repressed in neurons and the central nervous system to maintain low oxidative stress.[45,119] Therefore they do not have the ability to increase glycolysis when OXPHOS integrity is interrupted.[45] PFKFB3 enzymatically produces fructose-2,6-bisphosphate (a strong glycolytic activator) and is down-regulated in neurons. Its overexpression leads to oxidative stress and cell death *in vivo*.[45] Since neurons of the central nervous system rely almost completely on OXPHOS-generated ATP, they are highly vulnerable to decreases in ATP generation.[120] In the *hq* mice, this is evident due to the severe and irreversible onset of retinal and cerebellar degeneration.

### *1.17 Parainflammation is a chronic response in the hq retina*

Inflammation is the biological response to maintain homeostasis following a negative insult *in vivo*. Inflammation is commonly the product of a tissue injury or infection[121] and solicits the homeostatic response of the innate immune system and the adaptive immune system. The recognition of pathogens by the innate immune system begins with the specific binding of the pathogen-associated molecular patterns (PAMPs) expressed by microbes via Pattern Recognition Receptors (PRP)[122]. Following binding,

immune cells (macrophages) are recruited and the pathogen is destroyed and removed. The adaptive immune response is triggered for the selection of an antibody to better target the pathogen during future insult. In the event of a tissue injury, the innate immune system must respond to cellular damage of an endogenous injured cell and therefore PRPs are not present. The response to these injuries is facilitated by endogenous molecules known as alarmins that are released during non-programmed cell death and recruit the innate immune response.[123,124] One such example is that of architectural chromatin protein, High Mobility Group Box 1 (HMGB1).[125] Under apoptotic conditions HMGB1 binds irreversibility to nucleosomes and elicits no immune response, however under necrotic conditions HMGB1 is released into the extracellular space and becomes a potent activator of inflammation.[125]

In addition, alternative endogenous mechanisms beyond necrosis can induce inflammation. The formation of advanced glycation end-products (AGEs) begins under hyperglycemic or oxidative conditions and catalyzes the interaction of glucose with protein amino acids and lipids.[126] Once formed, they bind with the receptor for advanced glycation end-products (RAGEs) which can induce a pro-inflammatory response through the secretion of Tumor necrosis factor α (TNF-α) and stimulation of T-cells.[126] Under oxidative conditions; proteins, lipids and DNA can be oxidized. Lipids are oxidized into highly reactive aldehydes which in turn induce macrophage secretion of TNF-α and elicit an inflammatory response.[127] Finally, inflammatory cytokines released by activated macrophages can further induce inflammatory responses. Chronic cytokine release by macrophages causes further tissue damage and the potential breakdown of blood

barriers.[121] Inflammatory cytokines can alter the functionality of the endothelial/epithelial tight junctions leading to barrier degradation.[128]

Microglial cells are the resident macrophages of the retina and cerebellum that are responsible for the innate immune response during an inflammatory stimulus.[12] Resting, dormant microglia cells generally take on a ramified cellular morphology with many protrusions as a means to monitor their microenvironment as well as clearing any metabolic waste and tissue debris.[129] Microglial cells become activated during neuronal injury, stress and infection changing their cell morphology to an amoeboid macrophage. The surface membrane, G-coupled purinergic membrane receptor $P2Y_{12}$ can detect small changes of ADP and ATP concentrations in the extracellular space released by stressed or necrotic neurons and prompts microglial activation.[130] Activated microglia become highly mobile and exhibit strong phagocytic ability and further induce the release of cytokines to enhance microglia recruitment to mediate tissue repair.[121] During healthy conditions, this is generally a low-grade tissue adaptive response known as basal inflammation. In contrast, chronic activation of microglia cells as a result to neuronal stress can lead to a state of parainflammation. Parainflammation is an intermediate response between overt-inflammation and non-inflammatory removal of apoptotic cells.[121] Chronic microglial activation is associated with the release of tissue damaging ROS, nitric oxide, proteases, and further cytokines causing exaggerated recruitment of microglial cells and retinal degeneration.[131] Parainflammation and chronic microglial activation have previously been observed in the *hq* retina as early as 1.8 months of age as a result of AIF downregulation. Chronic microglial activation may be the cause of subsequent structural losses in the *hq* retina. The exact triggers leading to chronic

microglial activation has yet to be defined and may be the result of a continuous endogenous stress (tissue stress) or the breakdown of a retinal barrier allowing chronic influx of exogenous pathogens into the sensitive retinal space (Figure 1.3).

### *1.18 Central hypothesis*

I hypothesize that since the *hq* mouse is hypomorphic for AIF function in oxidative phosphorylation, health of the inner retina is compromised without loss of blood-retinal-barrier integrity and evidence of compensatory ATP production mechanisms exist.

### *1.19 Experimental Aims*

The first experimental aim is to determine if electroretinogram oscillatory potentials can infer early mechanisms of retinal degeneration, particularly operational in the inner retina. The use of OPs as a non-invasive diagnostic feature could infer physiological changes as well as the health of the inner retina prior to any cell losses. The rapid onset of the hemizygous *hq*Y disease leads to functional losses as well as later structural losses. OPs have been used to track disease progression prior to any symptomatic functional losses in a variety of retinal diseases as OP features infer the health of various neural networks in the retina. It is therefore predicted that OPs can be used to diagnose early functional changes in the *hq* retina prior to any structural losses. To track and examine disease progression, OP from *hq* mice were analyzed monthly from two months of age to ten months of age. This provides long term disease progression

information and functional retinal documentation at a later age. To complement the examination of OPs in the severe and rapid disease phenotype, the investigation of the heterozygote phenotype can provide valuable information regarding disease progression. Female heterozygotes demonstrate a longer timeframe to observe disease mechanisms prior to cell death and were examined at three months, eleven months and fifteen months of age.

The second experimental aim is to assess RPE (outer BRB) and inner retina endothelial vasculature barrier (inner BRB) integrity to ascertain the potential for exogenous triggers of microglial activation and subsequent retinal degeneration (Figure 1.3). This examination is instrumental in determining if the metabolic deficiency associated with *hq* neurons compromises the functionality of the highly metabolic RPE and inner retina endothelial vasculature barrier. Metabolic deficiency in the *hq* retina may result in the degradation of tight junctions and lead to vascular endothelial/epithelial leakage into the sensitive inner retinal space and thereby elicit microglial activation. Alternatively, it can be hypothesized that microglial activation in the *hq* retina is the consequence of endogenous photoreceptor and inner retinal neuron cell stress due to ATP deficiency triggering chronic microglial activation. To examine the integrity of the BRB, injections of Evans Blue followed by a complete vascular perfusion assesses diffusion of albumin-bound Evans Blue into the inner retina and potential breakdown of the BRB. Two age groups of mice were examined for both wild-type and *hq* mice: a younger age group (< 4 month) prior to ONL losses, and an older age group (> 7 months) corresponding to chronic microglial activation at 1.8 months. It is hypothesized

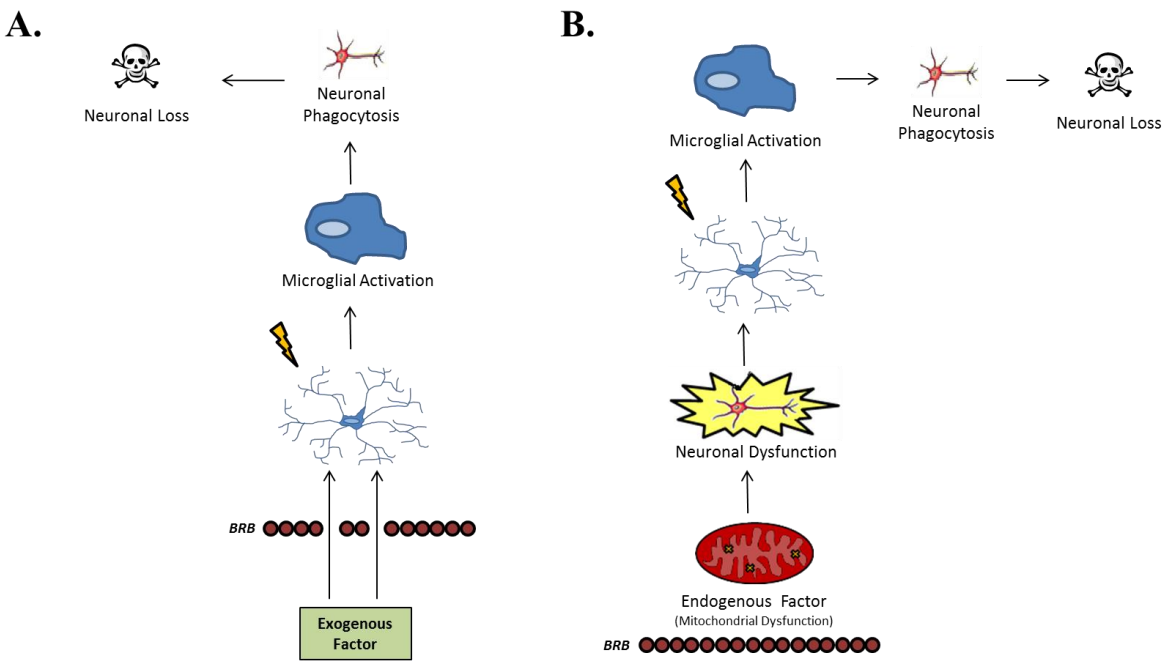
A.
Neuronal Loss
Neuronal Phagocytosis
Microglial Activation
BRB
Exogenous Factor
B.
Microglial Activation
Neuronal Phagocytosis
Neuronal Loss
Neuronal Dysfunction
Endogenous Factor
(Mitochondrial Dysfunction)
BRB

**Figure 1.3. Activation of retinal microglia may be the result of blood-retinal-barrier breakdown (exogenous) or inner retinal dysfunction (endogenous).** (**A**) Microglia activation (ramified to amoeboid) may be a consequence of BRB breakdown causing diffusion of harmful exogenous antigens into the sensitive retinal space. Highly metabolic epithelial and endothelial cells of the BRB may malfunction due to intracellular ATP deficiency. (**B**) Alternatively, microglia activation may be the result of internal neuronal malfunction due to AIF downregulation and ATP deficiency leading to cell stress, apoptotic and necrotic conditions thereby inducing parainflammation and chronic microglia activation.

that microglial activation in the retina is the result of endogenous ATP deficiency leading to cellular stress and apoptotic neurons rather than a compromised BRB inducing microglial activation.

The third and final aim is to confirm retinal transcriptome changes consistent with mitochondrial dysfunction and subsequent metabolic disease during the onset and progression of *hq* retinal and cerebellar degeneration. The downregulation and reduced expression of AIF leads to alternative metabolism in mesodermal tissues. It was predicted that similar compensating mechanisms were expected to transpire in the *hq* retina and cerebellum. Although glycolysis is unlikely to be upregulated in *hq* neurons, alternative pathways of ATP production such as lactate production, glycerol metabolism and glucose uptake are predicted to be upregulated. To confirm transcriptome changes consistent with alternative metabolism three ages were examined corresponding to disease onset and progression (two, three and four months of age). Since the cerebellum is not as ATP demanding as the retina[40] and histological changes occur later in the *hq* cerebellum it is expected that metabolic changes in the *hq* mouse are not as evident by four months of age.

# Chapter 2. Materials and Methods

## *2.1 Animal care and housing*

The Canadian Council on Animal Care and The Animal Use Subcommittee of The University Council on Animal Care approved all protocols prior to the commencement of any experimental work (Appendix A). Mice (B6:CBACaA$^{w\text{-}J}$/A-Pcdc8$^{hq/J}$, 97% CBA/CaJ genetic background) [Jackson Laboratories, Bar Harbor, ME] were housed at a constant temperature of 21 ± 1$^{o}$C with a relative humidity of 44% to 60% and a light/dark cycle of 14/10 hours. The mice received a standard diet [PMI Foods, St. Louis, MO] and water *ad libitum*.

## *2.2 Genotyping of the hq allele*

A tri-primer polymerase chain reaction (PCR) was used to determine the presence of the *Aif hq* allele.[93] Tissue samples for genotyping were taken as ear-notches when mice were approximately 12 days old. DNA was amplified using the Terra$^{TM}$ PCR Direct [Clontech, Mountain View, CA] standard protocol. Amplified DNA was subjected to gel electrophoresis through a 1.5% agarose gel stained with SYBR® Safe DNA Gel Stain [Life Technologies Inc., Burlington, ON]. The presence of a 725 bp amplicon indicated the *Aif hq* disease allele and the presence of a 537 bp amplicon indicated a wild-type *Aif* allele. Female heterozygous mice show both a 537 bp and a 725 bp amplicon. PCR primer sequences used for *Aif* genotyping are provided in Appendix B (Table B.1). Reference to the *hq* phenotype refers to the *hq*Y genotype unless otherwise specified. Wild-type (WT) mice refer to male (XY) mice with a functional *Aif*.

### *2.3 Collection of trace electroretinograms*

Repeated electroretinogram (ERG) analyses were performed on cohorts of wild-type mice and *hq*Y mice at two, three, four, five to seven and eight to ten months of age to assess retinal function and severe disease progression (Figure 2.1A,B).[132] Additionally, ERG analyses were performed on female carrier mice (*hq*X) along with an age-matched wild-type cohort at three, eleven and fifteen months to assess moderate disease progression of the *hq* carrier disease (Figure 2.1B).[102,103] Electroretinography was performed with a Colordome Stimulator [Diagnosys, Lowell, MA] on both dark-adapted (scotopic) eyes through a series of eleven flashes of increasing intensities (0.001 – 25 $cd \bullet m/s^2$).

### *2.4 Processing of trace electroretinogram for waveform modelling*

Original exported ERG trace files contained only data corresponding to parameters of the a-wave and b-wave components. A thorough review of the ERG user manual was performed and allowed for export of all raw data corresponding oscillatory potential components. A macro written into Excel [Microsoft, Redmond, VA] known as "MLTRIM" automatically sorted the original trace file into averaged neuronal responses for each eye and presented them as μV across all flash intensities.[133] In addition, MLTRIM was used to convert ERG trace data into a format readable by MATLAB [The MathWorks, Natick, MA].

**A.**

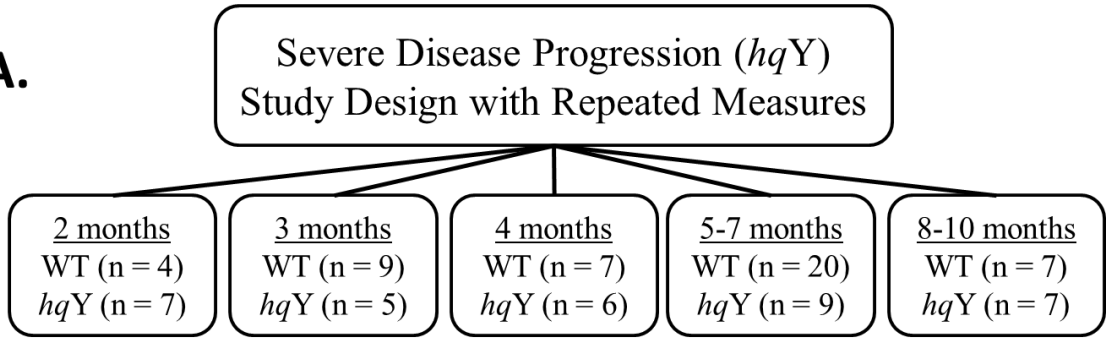
Severe Disease Progression (*hq*Y) Study Design with Repeated Measures
2 months
WT (n = 4)
*hq*Y (n = 7)
3 months
WT (n = 9)
*hq*Y (n = 5)
4 months
WT (n = 7)
*hq*Y (n = 6)
5-7 months
WT (n = 20)
*hq*Y (n = 9)
8-10 months
WT (n = 7)
*hq*Y (n = 7)

**B.**

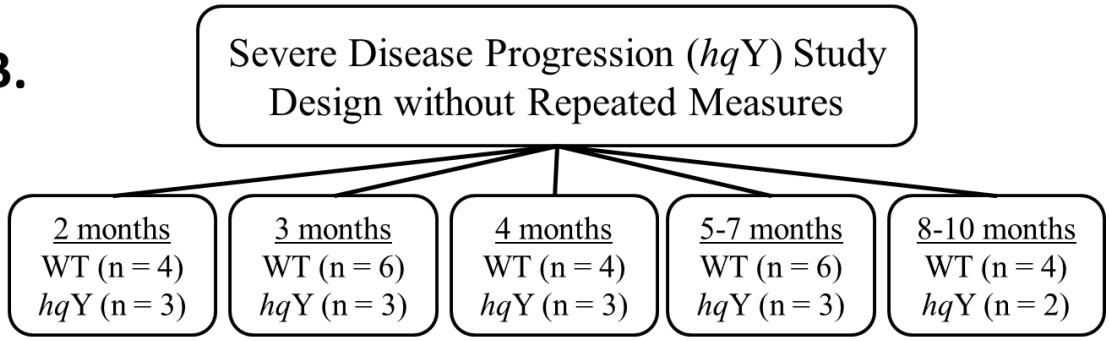
Severe Disease Progression (*hq*Y) Study Design without Repeated Measures
2 months
WT (n = 4)
*hq*Y (n = 3)
3 months
WT (n = 6)
*hq*Y (n = 3)
4 months
WT (n = 4)
*hq*Y (n = 3)
5-7 months
WT (n = 6)
*hq*Y (n = 3)
8-10 months
WT (n = 4)
*hq*Y (n = 2)

**C.**

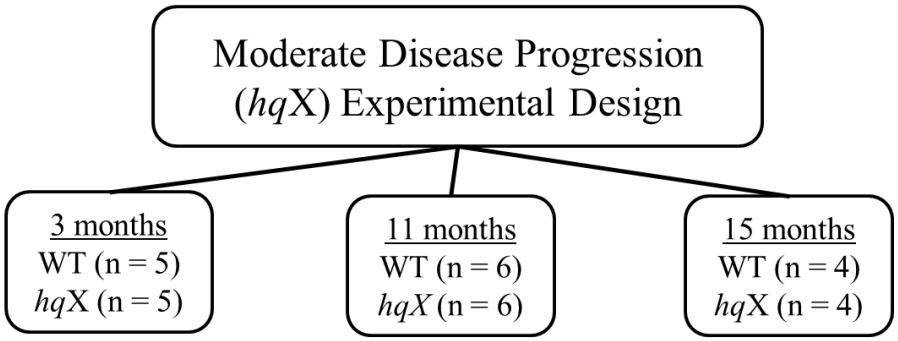
Moderate Disease Progression (*hq*X) Experimental Design
3 months
WT (n = 5)
*hq*X (n = 5)
11 months
WT (n = 6)
*hqX* (n = 6)
15 months
WT (n = 4)
*hq*X (n = 4)

**Figure 2.1. Experimental design and cohort sizes for oscillatory potential analysis.** (**A**) The complete experimental design for the severe disease progression *hq*Y analysis.[132] A single mouse may appear multiple times due to repeated measures at multiple ages. (**B**) Repeated measures of the severe disease progression experiment were removed randomly to allow study of *hq*Y mice without repetition. (**C**) The complete experimental design for the moderate disease progression *hq*X experiment.[103] No repeated measures were present in this study.

### *2.5 Signal conditioning and oscillatory potential waveform extraction*

Scripts (Appendix C, MATLAB Script A,B) were written into MATLAB [The MathWorks, Natick, MA] to model and extract relevant oscillatory potential waveforms (Figure 2.2).[133] To limit contribution of photoreceptor hyperpolarization, the a-wave was digitally modelled and subtracted from the original trace (Figure 2.2A).[66,68,69,71–74] Additional high frequency and low frequency noise were removed by processing the waveform through a fifth-order Butterworth filter with a band pass of 65-300 Hz (Figure 2.2C).[69,70] Previous literature suggests a lower band pass limit of 40 Hz for characterization of mouse rod photoreceptor oscillatory potentials, however 65 Hz was chosen to avoid interference by the 60 Hz line noise as previously described.[69,70] The remaining bandwidth made up the final OP waveform, herein known as the "extracted waveform".

### *2.6 Parameter analysis of the extracted waveform*

The extracted waveform was first analyzed in the time-domain. The amplitude (μV), initial latency (ms) and interpeak distance were determined for OP2, OP3, OP4, and OP5 (Figure 2.3A). Following waveform extraction, OP1 was typically present, however due to inconsistencies OP1 was not included in further analysis. Amplitude of each OP was defined as the difference between the trough and the peak immediately preceding it (Figure 2.3A). Initial latency was defined as the time from stimulus to the onset of OP2 (Figure 2.3A). Interpeak distance was the measurement of time (ms)

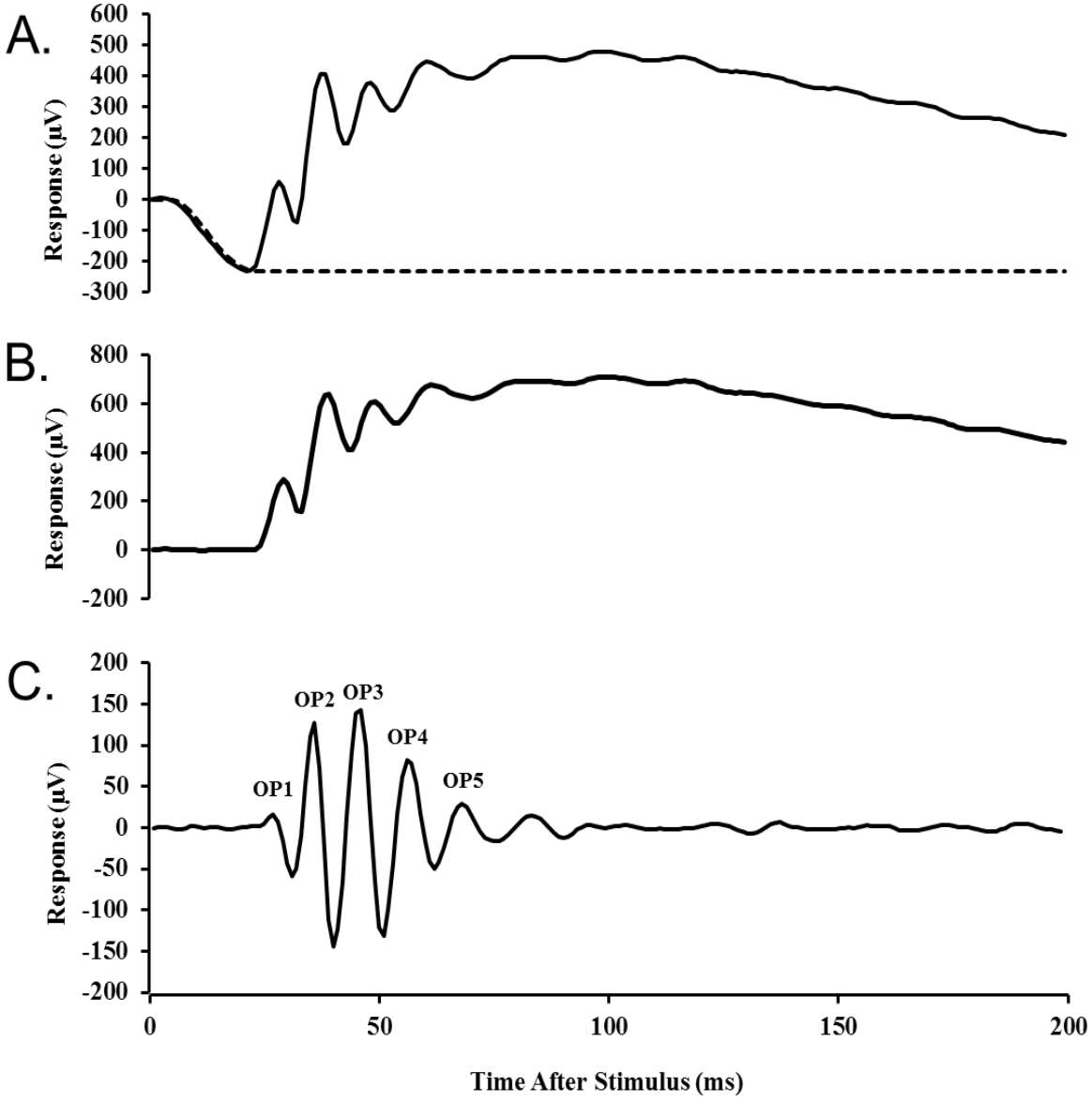
A.
600
500
400
300
200
100
0
-100
-200
-300
Response (µV)
B.
800
600
400
200
0
-200
Response (µV)
C.
200
150
100
50
0
-50
-100
-150
-200
OP1
OP2
OP3
OP4
OP5
Response (µV)
0
50
100
150
200
Time After Stimulus (ms)

**Figure 2.2 Signal conditioning of oscillatory potentials from the ERG trace waveform.** (**A**) A digital subtraction of photoreceptor contribution (dashed line) was performed by a mathematical fitting and subtraction of the a-wave from the initial ERG (solid line). (**B**) The ERG waveform following complete a-wave digital subtraction. (**C**) The final waveform was passed through a fifth order Butterworth transformation (65-300 Hz) to remove any low or high frequency noise resulting in the final "OP extracted waveform" (solid line).

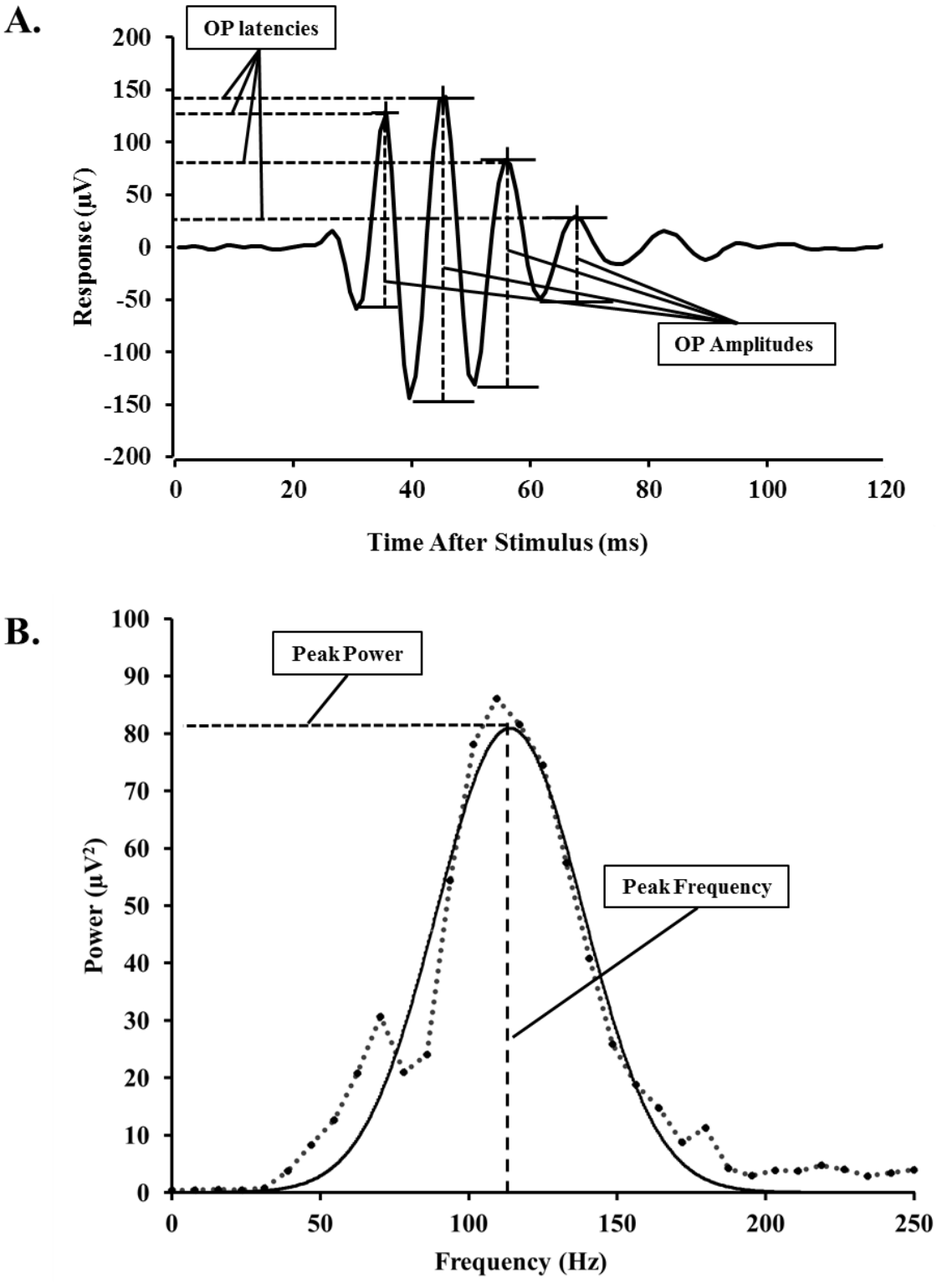
A.
OP latencies
OP Amplitudes
Response (μV)
Time After Stimulus (ms)
200
150
100
50
0
-50
-100
-150
-200
0
20
40
60
80
100
120
B.
Peak Power
Peak Frequency
Power (μV²)
Frequency (Hz)
100
90
80
70
60
50
40
30
20
10
0
0
50
100
150
200
250

**Figure 2.3. Measurement of individual Oscillatory Potential features in the time-domain and frequency-domain.** (**A**) Following waveform extraction, measurements of OP latency (ms) and amplitude (μV) were taken for OP2, OP3, OP4, and OP5. Amplitude of each OP was defined as the difference between the trough and the peak immediately preceding it. Initial latency was defined as the time from stimulus to the onset of the OP2 peak. Interpeak distance was the measurement of time (ms) between adjacent peaks. OP1 was not measured due to inconsistencies and the potential for a-wave contamination. (**B**) A fast Fourier transform (FFT) was applied to the extracted OP waveform and gave a single-sided smoothed frequency power spectrum (dotted Line). The single-sided smoothed frequency power spectrum was fitted to a two-term Gaussian envelope (solid line) and measurements of peak power ($P_{peak}$), peak frequency ($F_{peak}$) and total energy (waveform integration) were taken.

between adjacent peaks (i.e. OP2 and OP3) (Figure 2.3A). Total OP response in the time domain was measured as the summation of OP2-OP5 amplitudes.

### *2.7 Fast Fourier Transformation (FFT) of the extracted waveform*

The frequency spectrum of the extracted waveform was also analyzed by a Fast Fourier Transformation (FFT) to provide a holistic frequency waveform interpretation.[54] Scripts (Appendix C, MATLAB Script C) written in MATLAB [The MathWorks, Natick, MA] performed this operation and converted the frequency-power spectra to a single-sided smoothed frequency power spectrum. To avoid "powers of two" problems, only the first 128 samples of the extracted waveform (contained entire OP waveform) were applied to the FFT.[66] To calibrate the output of the FFT, a sine wave of known periodicity and amplitude was subjected to the algorithm. These produced a single peak indicative of a properly calibrated FFT algorithm. To avoid the problem known as 'overspill' the FFT output was fit to a two-term Gaussian envelope with the following equation: [66,75]

$$\mathrm{P(F)} = (Ppeak)[^{-\frac{1}{2}(\frac{F-Fpeak}{S})^2}]$$

where P is the power associated with the frequency response (F, Hz). $F_{peak}$ is the frequency at the peak of the Gaussian envelope, and $P_{peak}$ is the corresponding power (Figure 2.3B). Major frequency ($F_{peak}$) was determined as the dominant frequency of the Gaussian frequency-power spectrum and is related to OP periodicity. S indicates the width of the time distribution. The area under the original frequency power spectrum (Total energy) was calculated by integration of the original frequency-power spectrum (Figure 2.3B).

### *2.8 Non-Metric Multidimensional Scaling (NMDS) of oscillatory potential parameters*

The longitudinal nature of the *hq*Y study does not allow simple statistical testing (Figure 2.1). Approximately five mice were euthanized at the end of each age cohort age (2, 3, 4, 5-7, 8-10 respectively) and the attrition associated does not allow the application of a simple repeated-measures two-way ANOVA. In addition, OPs contain a wealth of information across multiple flash intensities and a comprehensive analysis was pursued as described in the introduction. A clustering method known as Non-metric Multidimensional Scaling (NMDS) was used in R Statistical Software [R Core Team, Vienna, Austria] (Appendix D, NMDS R-code A**)** to model every variable from each respective OP peak at all four flash intensities (Flash 8-11). This resulted in a total of 32 variables being analyzed in the time domain and 12 variables in the frequency domain (Figure 2.4). Each variable was first converted into a z-score using the following equation:

$$z - scores = \frac{x - \mu}{\sigma}$$

where $x$ is each value in the dataset, μ is the mean of the dataset and σ is the standard deviation of the dataset. The Euclidean distance between all mice was calculated encompassing all variables and a dissimilarity matrix was computed to demonstrate the absolute distances between mice.[82] A NMDS was then applied to model data in a two-dimensional ordination plot such that rank order matches the order of dissimilarity between mice. Stress is indicative of the best rank order of agreement between the dissimilarities as well as fitting the data to a monotonic regression (Shepard plot). Lowest

**A.**

| Time-Domain Measurements Taken | | | |
|---|---|---|---|
| Flash 8 (0.63 cd•s/m$^2$) | Flash 9 (4 cd•s/m$^2$) | Flash 10 (10 cd•s/m$^2$) | Flash 11 (25 cd•s/m$^2$) |
| Latency OP2 (ms) | Latency OP2 (ms) | Latency OP2 (ms) | Latency OP2 (ms) |
| Amplitude OP2 (µV) | Amplitude OP2 (µV) | Amplitude OP2 (µV) | Amplitude OP2 (µV) |
| Latency OP3 (ms) | Latency OP3 (ms) | Latency OP3 (ms) | Latency OP3 (ms) |
| Amplitude OP3 (µV) | Amplitude OP3 (µV) | Amplitude OP3 (µV) | Amplitude OP3 (µV) |
| Latency OP4 (ms) | Latency OP4 (ms) | Latency OP4 (ms) | Latency OP4 (ms) |
| Amplitude OP4 (µV) | Amplitude OP4 (µV) | Amplitude OP4 (µV) | Amplitude OP4 (µV) |
| Latency OP5 (ms) | Latency OP5 (ms) | Latency OP5 (ms) | Latency OP5 (ms) |
| Amplitude OP5 (µV) | Amplitude OP5 (µV) | Amplitude OP5 (µV) | Amplitude OP5 (µV) |
| 8 Meaurements | 8 Meaurements | 8 Meaurements | 8 Meaurements |
| **32 Total Measurements Per Mouse** | | | |

**B.**

| Frequency-Domain Measurements Taken | | | |
|---|---|---|---|
| Flash 8 (0.63 cd•s/m$^2$) | Flash 9 (4 cd•s/m$^2$) | Flash 10 (10 cd•s/m$^2$) | Flash 11 (25 cd•s/m$^2$) |
| Gaussian Peak Frequency (Hz) | Gaussian Peak Frequency (Hz) | Gaussian Peak Frequency (Hz) | Gaussian Peak Frequency (Hz) |
| Gaussian Power (µV$^2$) | Gaussian Power (µV$^2$) | Gaussian Power (µV$^2$) | Gaussian Power (µV$^2$) |
| Total Energy (µV$^2$•S) | Total Energy (µV$^2$•S) | Total Energy (µV$^2$•S) | Total Energy (µV$^2$•S) |
| 3 Measurements | 3 Measurements | 3 Measurements | 3 Measurements |
| **12 Total Measurements Per Mouse** | | | |

**Figure 2.4. Total number of measurements taken from a single mouse across four flash intensities.** (**A**) A total of 32 parameters are measured in the time-domain, eight measurements for each flash intensity. (**B**) A total of 12 parameters are measured in the frequency-domain, three for each flash intensity.

stress was found at the global optima following 100 iterations. Stress below 20% is deemed fair.[82] For NMDS axis interpretation a Pearson's correlation coefficient was used to interpret the axis in relation to various time domain and frequency domain parameters.

### *2.9 Experimental design for Blood-Retinal-Barrier (BRB) integrity phenotyping*

Male *hq*Y mice and age-matched wild-type controls were selected at two age cohorts of two-to-four months of age and seven months of age. The number of mice in each cohort was between three and five individuals. Evans Blue dye [Sigma Aldrich, St. Louis, MO] dissolved in 1X Phosphate Buffered Saline (PBS) (50µL) [Santa Cruz Biotechnology, Dallas, TX] was intravenously injected over 15 seconds through the tail vein at a concentration of 45 mg/kg.[134,135] Following injection, the dye was allowed to circulate through the vasculature for a period of 30 minutes. During this period the mouse turned visibly blue particularly in the extremities, confirming the uptake and distribution of the dye.[136] The mouse was then euthanized via $CO_2$ inhalation and the chest cavity was opened. A transcardial perfusion with 60 mL 1X PBS was performed until all blood was removed from the vasculature. Tissue was stored at -80$^{o}$C until further processing.

### *2.10 Generation of a standard curve to estimate Evans Blue tissue concentrations*

A standard curve was generated to calculate concentrations of EB in respective tissues. Serial dilutions of EB in formamide were made from 10000 ng/mL to 250 ng/mL and background-subtracted absorbances (620 nm - 740 nm) measurements were made in triplicate. Standards were prepared on different days by three different individuals.

### *2.11 Evans Blue Extravasation*

Immediately following PBS perfusion, eyes were enucleated and the retinas were carefully microdissected away and rinsed with PBS. Liver, cerebellum and cerebrum tissue were also harvested and rinsed with PBS. Tissues were flash frozen in liquid nitrogen and stored at -80$^{o}$C until further processing.

The wet weight of tissues was determined and they were then homogenized using a blunt homogenizer. The approximate weight of a mouse retina was 1 milligram and therefore approximately 1 mg of liver tissue was also processed as a technical control. EB was extracted from liver and retinal tissue by incubating in 100 µL of formamide [Sigma Aldrich, St. Louis, MO] for 24 hours at 75$^{o}$C.[134] Cellular debris was removed by centrifugation at 4000 rpm for 45 minutes. Approximately 1 µL of supernatant was used for triplicate spectrophotometric measurements using the NanoDrop ND-1000 Spectrophotometer [Thermo Scientific, Wilmington, DE]. A background-subtracted absorbance was determined with measurements at 620 nm and 740 nm, known absorbance maximum and minimums for EB dye.[134] The concentration of the dye in the extracts was determined using the standard curve and was normalized to liver concentrations from the same animal to account for technical variation such as albumin dye uptake and injection efficiencies. Statistical significance was determined using a two-way ANOVA.

### *2.12 Examining daily food consumption in the hq mouse*

Four-month-old *hq*Y (n = 4) and age-matched, wild-type (n = 4) mice participated in a feeding study to determine average daily food consumption (grams of food consumed/ grams of body mass/ day) differences in *hq* mice. Food intake (mass) and mouse mass were measured every-other-day over a two-week period to determine daily food consumption. At the end of the two-week period, average daily food consumption for each mouse was determined and divided by the mouse mass. Statistical significance was determined by a repeated-measures ANOVA.

### *2.13 Microarray pathway analysis*

To identify early triggers and mechanisms of retinal degeneration, gene expression microarray [Affymetrix, Mouse Gene 1.0 ST Array, Santa Clara] data were analyzed extensively. The microarray data were obtained by Alex Laliberté with 4-month-old *hq* and age-matched wild-type mice.[103] To determine early mechanisms of retinal degeneration selection criterion were set; at a significant change of $p < 0.05$ and a threshold fold change (mRNA transcript level) of at least ± 1.75. Canonical pathway analysis was performed using KEGG Pathway Analysis [Kyoto University, Kyoto, Japan] and Ingenuity Pathway Analysis [Ingenuity Systems Inc., Redwood City, CA]. A thorough literature review of *Aif* function complemented this pathway analysis and indicated a loss of *Aif* function leads to increased glucose metabolism, lactate metabolism, as well as glycerol and fatty acid metabolism.[98] Due to the specific nature of retinal degeneration markers and multiple genetic isoforms used in the retina, gene

ontology databases did not provide a thorough review of microarray data. Therefore grouping and annotation of differentially-expressed genes was performed manually and based on extensive literature survey on above pathways in NCBI [National Institute of Health, Bethesda, MD] (Appendix E). Multiple genes (>1.75 fold change, $p < 0.05$) from each above stated pathway were selected for confirmation of transcriptome changes via quantitative PCR (qPCR).

### *2.14 Tissue harvest for gene expression assays*

Cohorts of *hq*Y mice aged two-, three-, and four-months of age and age-matched wild-type mice (n = 5 per cohort) were euthanized via $CO_2$ inhalation according to Animal use Protocol (AUP) 2009-033 (Appendix A). Eyes were enucleated and retinas were microdissected and cleaned with 1X PBS in an RNase-free environment. Cerebellum, cerebrum and liver tissues were also harvested. Extracted retinas and cerebella were flash frozen in liquid nitrogen and stored at -80$^{o}$C. All tools involved in microdissection were baked overnight at 200$^{o}$C or treated with RNaseZAP [Sigma Aldrich, St. Louis, MI] to ensure an RNase-free environment and RNA integrity.

### *2.15 Retinal RNA extraction*

Retinal samples (~1 mg) were homogenized and lysed using a sand homogenization protocol as previously described.[137] Ottawa Sand (20-30 mesh) [Fisher Scientific, Fair Lawn, NJ] was rinsed through multiple, serial washes of $ddH_2O$, 0.5M NaOH and 0.5M HCl and baked overnight at 200$^oC$. Following homogenization, RNA was isolated using the Qiagen® RNeasy Mini Spin Columns Kit [Qiagen Canada Inc., Montreal, QC]. This included binding of total RNA to a silica membrane within the spin-column. A series of subsequent RPE® and RW1® washes were performed to clean the RNA and increase efficacy of RNA binding to the silica column membrane. An on-column Qiagen® RNase-Free DNase [Qiagen Canada Inc., Montreal, QC] step was performed to remove genomic DNA (gDNA) contamination. RNA was resuspended in nuclease-free $ddH_2O$ and stored at -80$^oC$.

### *2.16 Cerebellar RNA extraction*

Cerebellar samples (30 mg) were lysed with Qiazol® Lysis Buffer [Qiagen Canada Inc., Montreal, QC] and were homogenized by 20 strokes in a 7 mL Type A Glass Dounce Homogenizer [Wheaton Science Products, Millville, NJ]. Following homogenization, total RNA was isolated using the standard protocol for the Qiagen® RNeasy Mini Spin Column Kit [Qiagen Canada Inc., Montreal, QC] as described above. An additional on-column RNase-Free DNase step was added and RNA was resuspended in nuclease-free $ddH_2O$ and stored at -80$^oC$.

### *2.17 Assessment of RNA purity and quality*

Retinal and cerebellar RNA quality was first assessed with a NanoDrop ND-1000 Spectrophotometer [Thermo Scientific, Wilmington, DE] to determine A260/A280 ratios (>1.9). Cerebellar samples were then subjected to gel electrophoresis and electrophoresed through a 1.5% agarose gel to determine the presence, integrity and ratios of the 18S and 28S rRNA subunits. This quality assurance stage was not performed with the retinal samples as the total amount of RNA isolated was considerably lower and not sufficient to perform gel electrophoresis. However, to ensure RNA purity, both cerebellar and retinal samples (1 µL) were assessed with the Agilent 2100 Bioanalyzer [Agilent Technologies Inc., Palo Alto, CA] to determine RNA integrity (RNA Integrity Number - RIN > 8).

### *2.18 cDNA synthesis*

Mouse retinal RNA samples were selected for single-stranded, complementary DNA (cDNA) synthesis from concentrations ranging from 15 ng/µL to 72 ng/µL. Mouse cerebellar samples were selected for cDNA synthesis from concentrations ranging from 84 ng/µL to 354 ng/µL. In each age cohort, the lowest concentration was selected as the rate-limiting sample, indicating the highest total RNA (µg) that could be added to the cDNA synthesis reaction based on the final volume of 16 µL. cDNA synthesis was performed using the Superscript® VILO™ cDNA Synthesis Kit [Life Technologies, Burlington, ON] and its associated standard protocol. A negative control did not contain any RNA and dd$H_2O$ was used as a substitute. Following synthesis, cDNA was diluted to 100 µL to increase downstream throughput and stored at -20$^{o}$C.

### *2.19 Taqman® gene expression experimental design*

qPCR was performed using Taqman® probes [Life Technologies, Burlington, ON]. Probes that spanned exon junctions were selected to avoid the possibility of false amplification due to gDNA contamination. Genes were assayed in a block design for each age cohort (Appendix B, Figure B.1). Each gene of interest was assayed in three technical replicates including triplicate No-Template Controls (NTC). Biological replicates were assayed in parallel to avoid the possibility of additional technical variation (n = 4). For each reaction; 5µL of Taqman® Fast Advanced MasterMix [Life Technologies, Burlington, ON], 0.5 µL of Taqman® probes [Life Technologies, Burlington, ON], 2.5 µL of nuclease free water and 2 µL of cDNA were added to a final volume of 10 µL per reaction well. The assay was performed using the ViiA™ 7 Real-Time PCR System [Life Technologies, Burlington, ON]. qPCR cycling conditions began with a 2 minute hold at 50$^{o}$C for Uracil N Glycosylase incubation, a 20 second hold at 95$^{o}$C for complete cDNA denaturation, followed by 40 cycles of 1 second at 95$^{o}$C for denaturation and 20 seconds at 60$^{o}$C for primer annealing and polymerase extension. Two reference genes, *18S Ribosomal RNA (Rn18s) and Glyceraldehyde-3-phosphate dehydrogenase (Gapdh)* were selected as normalizer genes due to their documented high and consistent expression levels in all tissues.[138,139] *Rn18s* was selected to ensure expression of *Gapdh* was consistently expressed between *hq* and wild-type mice. Upon confirmation of high, consistent uniform expression of *Gapdh* across genotypes, *Gapdh* was selected as the primary normalizer. *Aif* was assayed across all cohorts to ensure a downregulation in *hq* mouse retina and cerebellum.

### *2.20 Statistical analysis of Taqman® gene expression changes*

The ΔΔCt relative quantification method was used to determine fold-changes across genotypes.[140] ΔCt values were determined as the difference between the measured average amplification cycle of the gene of interest and the average amplification cycle of *Gapdh*. Significance was determined with a one-way ANOVA in Excel [Microsoft, Redmond, VA] comparing ΔCt values between *hq* and wild-type mice in each cohort. To calculate fold-change the *hq* ΔCt values were subtracted from wild-type ΔCt values to yield a ΔΔCt value which was then input in to the following equation to determine fold change:

$$\text{Fold Change} = 2^{-\Delta\Delta Ct}$$

# Chapter 3. Results

## *3.1 Mouse phenotyping and Aif PCR genotyping confirmed the presence or absence of an Aif proviral insertion*

Characteristic phenotypic *hq* markers such as a patchy coat, ataxia and low body mass were consistently observed among $X^{hq}X^{hq}$ and $X^{hq}Y$ mice. Genotypes of mice used in this study were confirmed by PCR using the tri-primer method. A 725 bp amplicon indicated the presence of an *Aif* hemizygous males (*hq*Y) proviral insertion whereas the presence of a 537 bp amplicon indicated a wild-type *Aif* allele (Figure 3.1). Female heterozygotes (*hq*X) showed amplification of both 537 bp and 725 bp amplicons (Figure 3.1).

## *3.2 hqY mice show longer latency as early as three months and progressive decreases in OP summed amplitude following a 10 cd•s/m$^2$ stimulus*

Time-domain analysis of ERG OPs revealed no early (two month) delays of initial OP latency in *hq* disease mice when compared to the wild-type mice (Figure 3.2A). However, by three months of age *hq* mice demonstrate a significant delay ($p = 0.005$, Figure 3.2A) of initial OP latency by 24.6%. This is indicative of neural retinal feedback delay between the photoreceptors, INL and GCL of the retina. The trend of OP delayed response continues at four months and is significantly delayed at five to seven months ($p = 0.0115$, Figure 3.2A). Summed OP amplitudes demonstrated no significant changes at two or three months of age in the *hq* mice indicating normal INL and GCL function

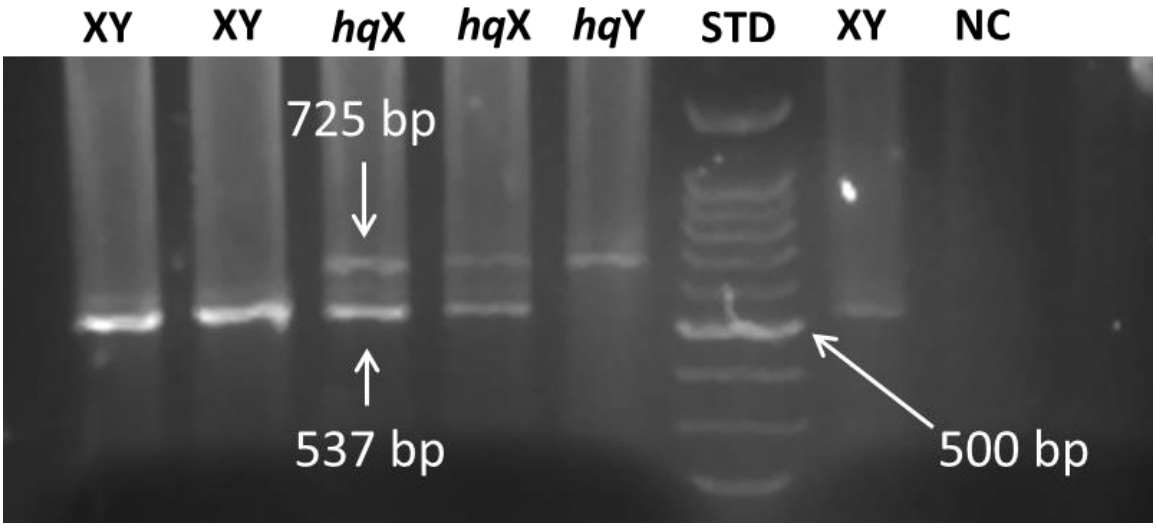


**Figure 3.1. PCR amplification confirmed *Aif* genotype.** *Aif* genotyping PCR amplicons were electrophoresed through a 1.5% agarose gel and stained with SYBR® Safe DNA Gel Stain (Invitrogen, Burlington, ON). A 100 bp DNA ladder (FroggiaBio Inc, Toronto, ON) was used as a size standard (STD) to estimate amplicon size. A single 537 bp amplicon indicated a wild-type *Aif* allele (XY) while a single 725 bp amplicon indicated the presence of an *Aif* proviral insertion.[93] Heterozygote, *hq* carriers demonstrated the presence of both 537 bp and 725 bp amplicons. A no DNA control (NC) was created with water prior to amplification and added to the PCR mastermix to eliminate the possibility of a false positive.

(Figure 3.2B). However by four months of age, a significant deterioration of summed OP amplitudes (p = 0.0222) by 26.5% occurred in *hq* mice resulting in reduced INL and GCL function (Figure 3.2B). The largest effect on summed OP amplitudes occurred at five to seven months with a significant reduction (p = 0.003, Figure 3.2B) by 54.4%. No statistical conclusions can be made about initial OP latency or summed OP amplitudes at eight to ten months of age as the *hq* cohort only contains two mice, although general trends appear to continue (Figure 3.2A,B).

### *3.3 Frequency-domain analysis of ERG OPs show early frequency changes in hqY disease mice followed by later changes in OP power and energy (10 cd•s/m$^{2}$ - stimulus)*

*hq*Y OP frequency demonstrated early, two-month changes with a significant reduction by nearly 14% in comparison to the wild type. Significant reductions were also present at three (p = 0.0015, 26.6%) and four months (p = 0.0248, 25.9%) of age (Figure 3.3A). This is indicative of delayed periodicity and reduced neural feedback mechanisms. *hq*Y overall OP power showed no early significant changes at two, three, or four months in comparison to the wild type (Figure 3.3B). This indicated adequate uniform retinal response of the INL and GCL of the *hq* mice. However by five to seven months of age, overall OP power demonstrated a significant reduction (p = 0.0028) by nearly 54.5% in comparison to the wild type (Figure 3.3B). Total OP waveform energy, indicative of total retinal INL, GCL and retinal response across the entire retina, demonstrated no early changes at two or three months of age in *hq*Y mice (Figure 3.3C). A significant decline

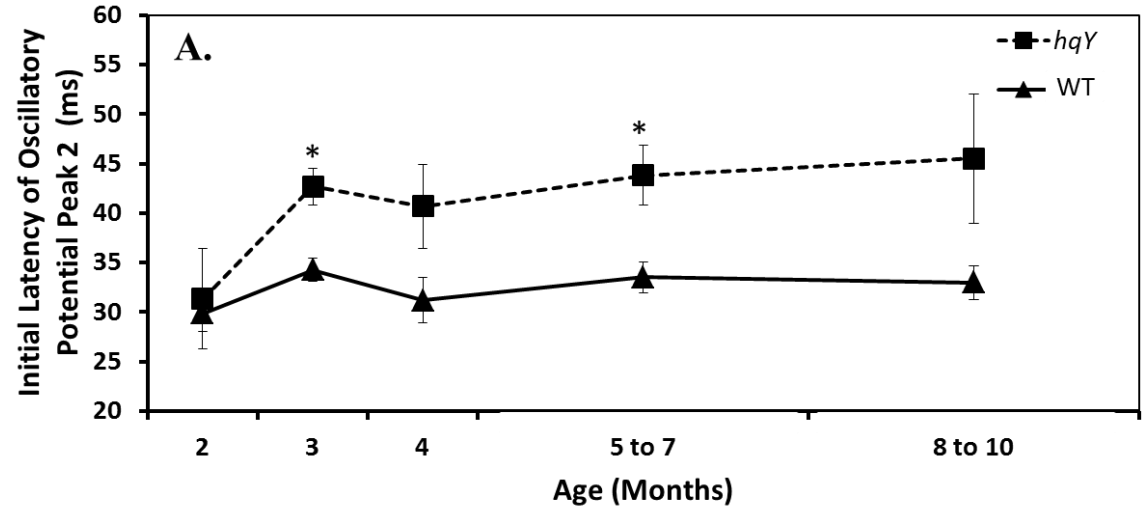
A.
hqY
WT
Initial Latency of Oscillatory Potential Peak 2 (ms)
60
55
50
45
40
35
30
25
20
*
*
2
3
4
5 to 7
8 to 10
Age (Months)

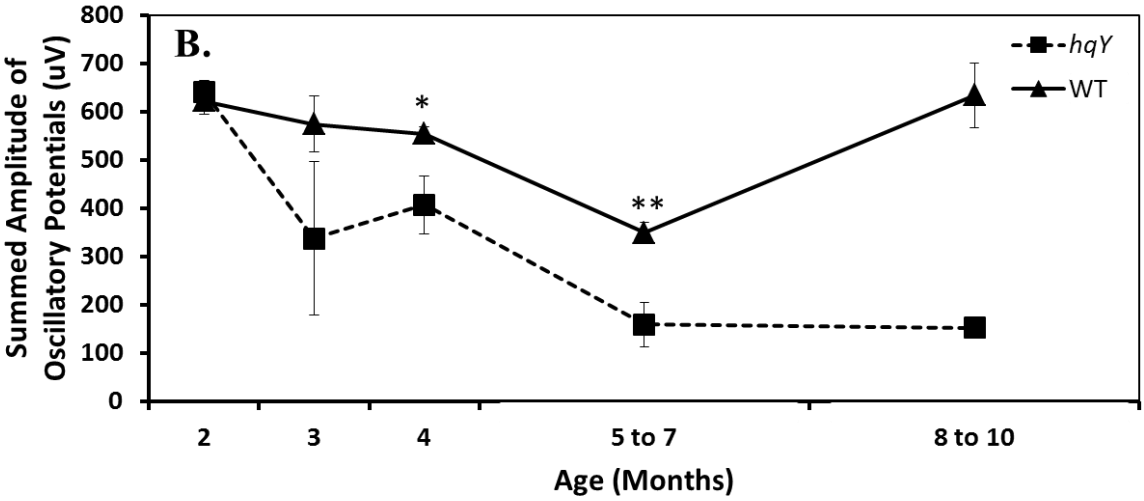
B.
hqY
WT
Summed Amplitude of Oscillatory Potentials (uV)
800
700
600
500
400
300
200
100
0
*
**
2
3
4
5 to 7
8 to 10
Age (Months)

**Figure 3.2. Electroretinography demonstrates delayed retinal responses and decreases in initial OP latency followed by subsequent reductions in summed OP amplitudes in the *hq* retina following a 10 cd•s/m$^2$ stimulus.** (**A**) Initial latency of OP2 indicates the functional response of the INL and GCL cells to photoreceptor hyperpolarization. Delayed initial latency of OP2 is evident at three months in *hq* mice with a significant delay of nearly 24.6% in comparison to the wild type. The delay in *hq* initial OP response is also evident at five to seven months with an overall delay by 30.8%. (**B**) Summed amplitude is indicative of the overall retinal response and continuity of neural feedback of the INL and GCL. Significant reductions in *hq* OP summed amplitude are first apparent at four months of age resulting in an overall reduction by nearly 26.5%. In five-to-seven-month-old *hq* mice, the disease reduces summed OP amplitudes by 54.5%. The effect of age on genotype was also examined for all measured variables (data not shown, Appendix B, Table B.6A) Sample size per cohort can be found in Figure 2.1B. Asterisks indicate statistical significance (* $p < 0.05$, ** $p < 0.005$) and error bars represent ± 1 standard error of the mean.

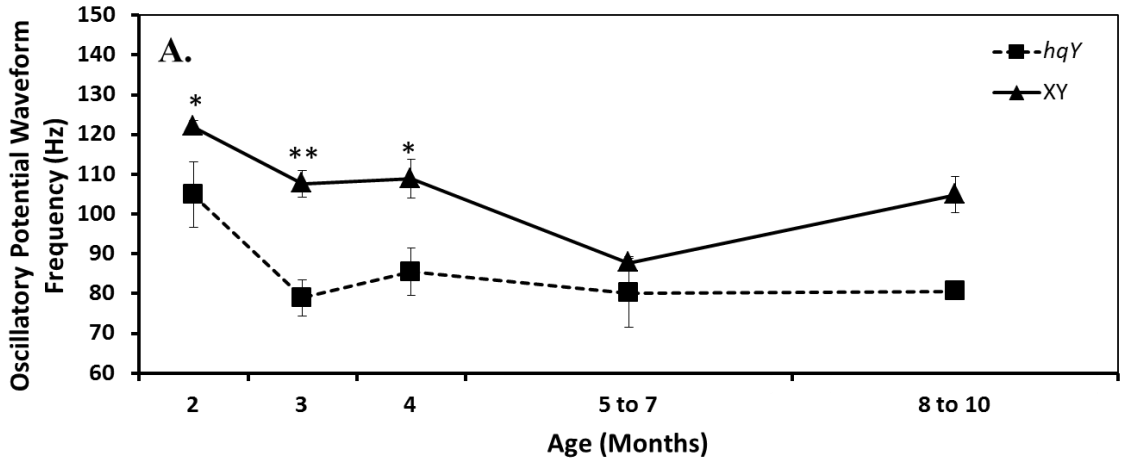
A.
hqY
XY
Oscillatory Potential Waveform Frequency (Hz)
150
140
130
120
110
100
90
80
70
60
*
**
*
2
3
4
5 to 7
8 to 10
Age (Months)

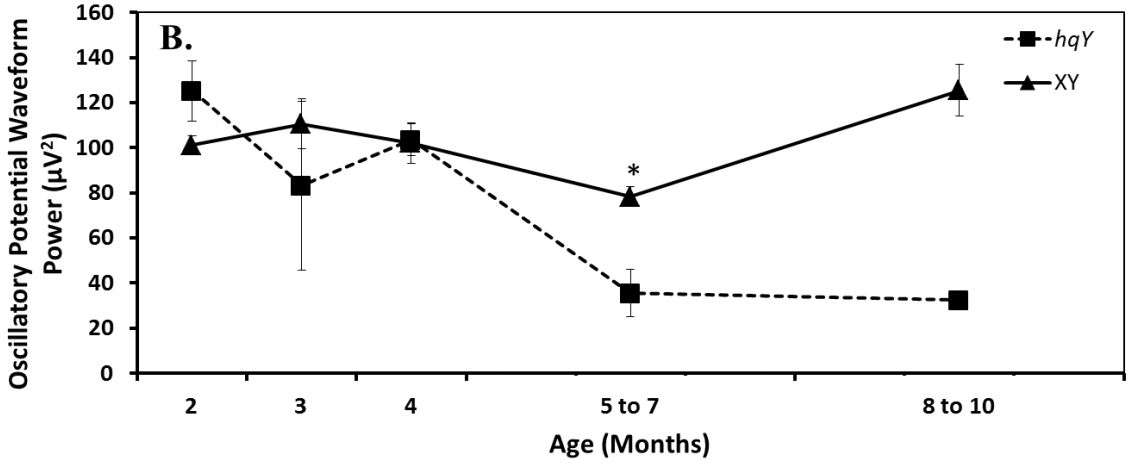
B.
hqY
XY
Oscillatory Potential Waveform Power (μV²)
160
140
120
100
80
60
40
20
0
*
2
3
4
5 to 7
8 to 10
Age (Months)

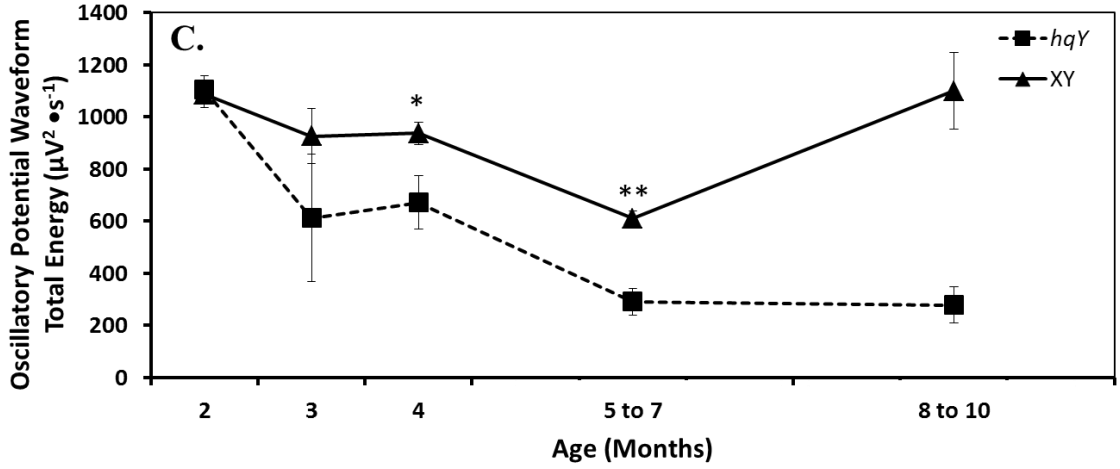
C.
hqY
XY
Oscillatory Potential Waveform Total Energy (μV² •s⁻¹)
1400
1200
1000
800
600
400
200
0
*
**
2
3
4
5 to 7
8 to 10
Age (Months)

**Figure 3.3. *hq*Y mice have changes in OP waveform frequency as early as two months of age, followed by subsequent reductions of OP power and energy following stimulus of 10 cd•s/m$^2$.** (**A**) Significant OP frequency reductions were evident immediately at two months of age with a 14% decline in comparison to the wild type. OP frequency continued to decline in *hq*Y mice at 3 (26.6% reduction) and four months (25.9% reduction) of age in comparison to the wild type. This was indicative of a prolonged INL and GCL periodicity. (**B**) OP power is a measure of uniform retinal response of the INL and GCL. OP power showed a significant reduction of 54.5% by five to seven months in *hq* mice and continued to decline until eight to ten months. (**C**) OP energy is the summation of total OP retinal energy and was not significantly different at two or three months of age in *hq* mice. However, by four months of age *hq* mice show a significant reduction of OP energy by nearly 28.3% which progresses to a nearly 52.3% reduction by five to seven months of age. This indicates progressive disease in the *hq* retina particularly in the INL and GCL response. The effect of age on genotype was also examined for all measured variables (data not shown, Appendix B, Table B.6B) Sample size per cohort can be found in Figure 2.1B. Asterisks indicate statistical significance (* $p < 0.05$, ** $p < 0.005$) and error bars represent ± 1 standard error of the mean.

($p = 0.029$) is evident at four months of age resulting in a 28.3% reduction of OP energy (Figure 3.3C). The decline in OP energy continues as the *hq* disease progresses and by five to seven months an overall significant reduction ($p = 0.0006$) by 52.3% is apparent (Figure 3.3C). No statistical conclusions can be made about OP frequency, power or total energy at eight to ten months of age as the *hq* cohort only contains two mice, although general trends appear to continue (Figure 3.3A, B,C).

### *3.4 Time-domain analysis of OPs indicate decreased summed amplitude in hq carrier mice as early as eleven months of age following a 10 cd•s/m$^2$ stimulus*

Initial latency of OP2 revealed no significant changes across all ages of the *hq*X heterozygote when compared to the wild type (Figure 3.4A). Summed amplitude, a measure of total inhibitory feedback mechanisms of the INL and GCL demonstrated no significant changes at three months when compared to the wild type. In the eleven-month cohort, a significant reduction of summed OP amplitude was evident ($p = 0.011$; Figure 3.4B) at nearly 40.6%. Similarly, a significant reduction of 70.9% was observed in summed OP amplitudes at fifteen months ($p = 0.0341$; Figure 3.4B) indicating overall INL and GCL dysfunction and progression of the *hq* disease.

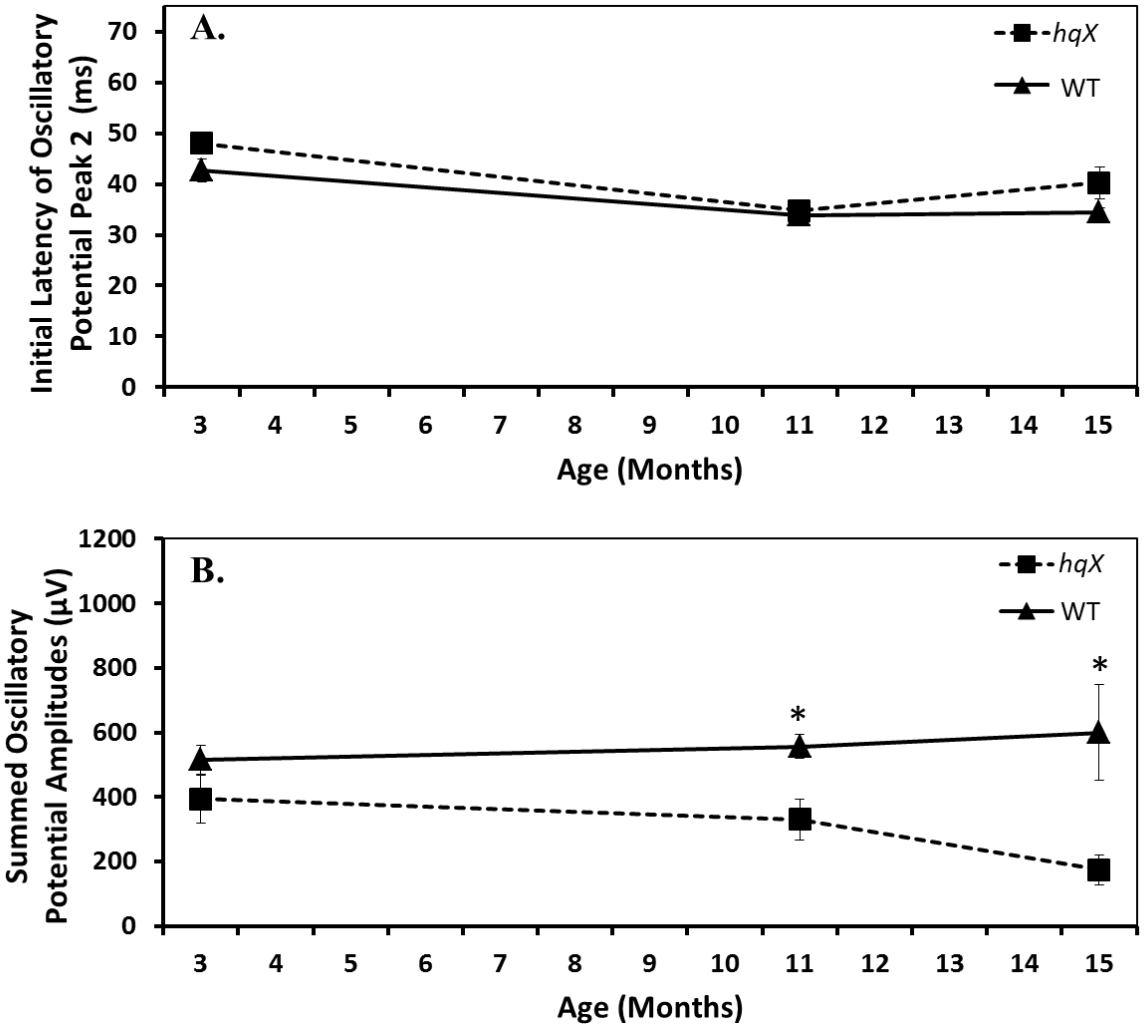
A.
hqX
WT
Initial Latency of Oscillatory Potential Peak 2 (ms)
70
60
50
40
30
20
10
0
3
4
5
6
7
8
9
10
11
12
13
14
15
Age (Months)
B.
hqX
WT
Summed Oscillatory Potential Amplitudes (µV)
1200
1000
800
600
400
200
0
*
*
3
4
5
6
7
8
9
10
11
12
13
14
15
Age (Months)

**Figure 3.4. OP2-5 summed amplitudes indicates progressive loss of functional feedback mechanisms of the *hq* carrier retina following a 10 cd•s/m$^2$ stimulus.** (**A**) Initial latency of OP2 is indicative of the initial neural response between photoreceptors and bipolar and horizontal cells of the INL and GCL. Although not statistically significant at any age it is apparent that *hq*X may have a lengthened initial latency in comparison to the wild type. (**B**) Summed amplitude of all OPs is indicative of the health of the neural retina and the continuity of feedback mechanisms of the INL and GCL. Significance is evident at eleven months of age with a 40.6% reduction in overall summed amplitude. INL and GCL function continued to decline as demonstrated by a significant reduction of OP summed amplitude by 70.9% at fifteen months. The effect of age on genotype was examined for all measured variables (data not shown, Appendix B, Table B.6C) Sample size per cohort can be found in Figure 2.1C. Asterisks indicate statistical significance (* $p < 0.05$) and error bars represent ± 1 standard error of the mean.

### *3.5 OPs of hq carrier mice indicate early functional periodicity deficits and subsequent reductions in retinal response continuity following a 10 cd•s/m$^2$ stimulus*

OP frequency, a measure of response of periodicity and neural feedback mechanisms across the INL and GCL, showed early functional deficits in *hq* carrier mice at three months of age ($p = 0.049$) with an overall reduction of 10.9% (Figure 3.5A). However, at eleven and fifteen months of age *hq* carrier mice showed no significant difference in overall OP frequency (Figure 3.5A). Overall power, a measure of uniform retinal response, showed no significant changes in *hq* carrier mice when compared to the wild type at three months of age (Figure 3.5B). By eleven months of age, retinal continuity in *hq*X mice is significantly reduced ($p = 0.013$) by 43.7% and progressive decreases lead to a significant ($p = 0.0047$) 62.9% reduction by fifteen months (Figure 3.5B). OP total energy, a summation of total retinal response and analogous to OP summed amplitude demonstrated no significant differences at both three and eleven months of age in the *hq* carrier mice (Figure 3.5C). A significant difference was observed in retinal OP total energy at fifteen months with a significant reduction ($p = 0.002$) of 66.3% (Figure 3.5C).

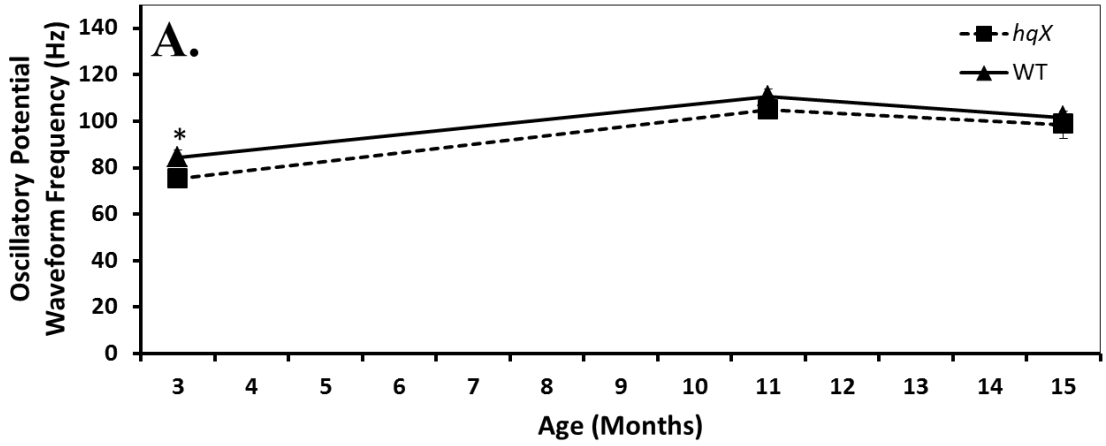
A.
hqX
WT
Oscillatory Potential Waveform Frequency (Hz)
0
20
40
60
80
100
120
140
*
3
4
5
6
7
8
9
10
11
12
13
14
15
Age (Months)

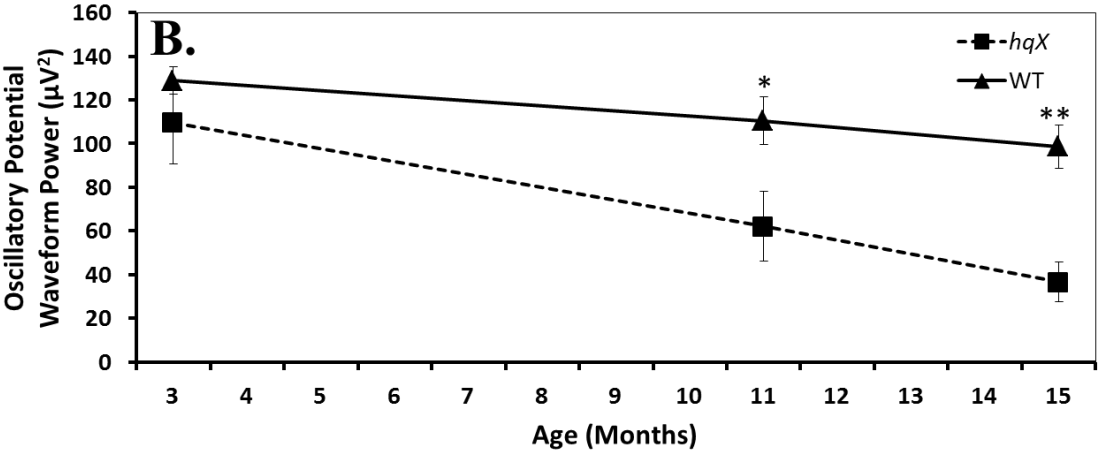
B.
hqX
WT
Oscillatory Potential Waveform Power (μV²)
0
20
40
60
80
100
120
140
160
*
**
3
4
5
6
7
8
9
10
11
12
13
14
15
Age (Months)

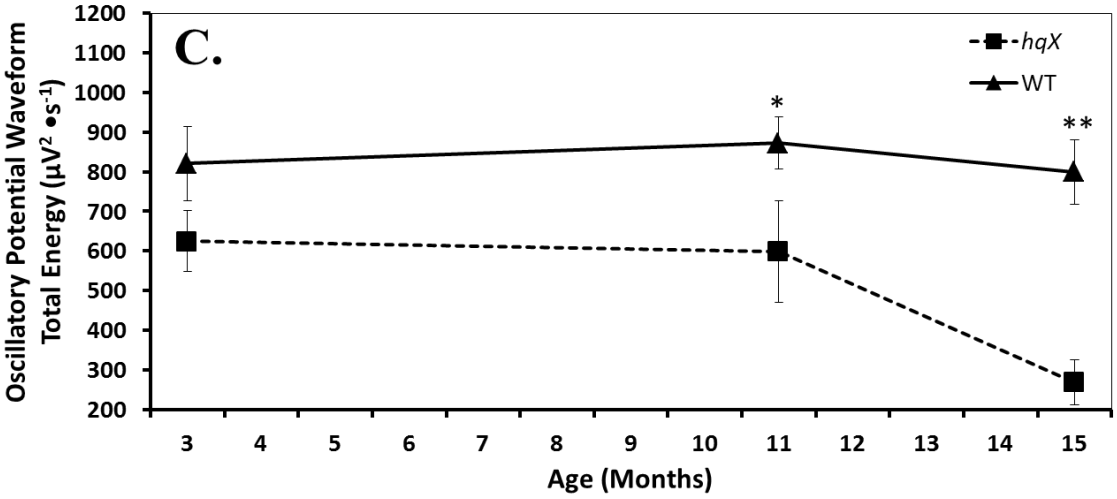
C.
hqX
WT
Oscillatory Potential Waveform Total Energy (μV² • s⁻¹)
200
300
400
500
600
700
800
900
1000
1100
1200
*
**
3
4
5
6
7
8
9
10
11
12
13
14
15
Age (Months)

**Figure 3.5. Frequency-domain OPs expose early functional differences of periodicity in three-month-old *hq* carrier mice and subsequent losses of OP power and energy following a stimulus of 10 cd•s/m$^2$.** (**A**) Frequency of OPs is indicative of periodicity of feedback inhibitory mechanisms of the INL and GCL. Significance in OP frequency response changes in the *hq* carrier mice at three months, with the *hq*X mice demonstrating a significantly lower OP frequency response. (**B**) OP Power is a measure of uniform retinal response of the INL and GCL. Statistical significance is evident in *hq* carrier mice at eleven months of age with an overall reduction of OP power by 43.7%. OP power and INL and GCL function continued to decline in comparison to the wild type leading to an overall reduction by 62.9% by fifteen months of age. (**C**) Energy of the OP waveform is the summation of the total OP response and was not statistically significant in three- and eleven- month-old *hq* carrier mice when compared to the wild type. However by 15 months of age, OP energy was significantly reduced by 66.3% in *hq* carrier mice indicting the progressive nature of the *hq* disease on INL and GCL function. The effect of age on genotype was also examined for all measured variables (data not shown, Appendix B, Table B.6D) Sample size per cohort can be found in Figure 2.1. Asterisks indicate statistical significance (* $p < 0.05$, ** $p < 0.005$) and error bars represent ± 1 standard error of the mean.

### *3.6 NMDS of time-domain hqY OP parameters indicate functional differences in OP latencies and amplitudes as early as two months of age*

The stress associated with modelling all 32 time-domain variables from the severe *hq*Y disease progression study into a two-dimensional axis was 11.31%. Pearson's correlation coefficients were used for axis interpretation following NMDS of *hq*Y OP time-domain parameters (Appendix B, Table B.2). The x-axis (Coordinate 1) is highly correlated to OPs with shorter latencies, particularly initial latencies of OP2 and OP3 at all flash intensities (Figure 3.6). The x-axis is also positively correlated with increasing OP amplitudes particularly amplitudes of OP4 and OP5 at all flash intensities. The y-axis (Coordinate 2) is positively correlated to decreasing OP amplitudes across all flash intensities (Figure 3.6). Young *hq*Y and wild-type mice cluster distinctly at two months of age with *hq*Y mice demonstrating decreased OP amplitudes in comparison to the wild type (Figure 3.6A). Aging of the *hq*Y mice is associated with a sharp decline in OP amplitudes and latencies between two and three months of age indicative of reduced INL and GCL function (Figure 3.6A). The disease appears to be progressive, leading to further reductions of OP latencies and amplitudes as the *hq*Y mice age (Figure 3.6A). Inter-animal variation is much higher in the *hq*Y mice, likely due to variation in the severity of retinal degeneration occurring in the *hq*Y mice (Figure 3.6A). Wild-type mice show little OP amplitude change and slight decreases in OP latencies through time (Figure 3.6A).

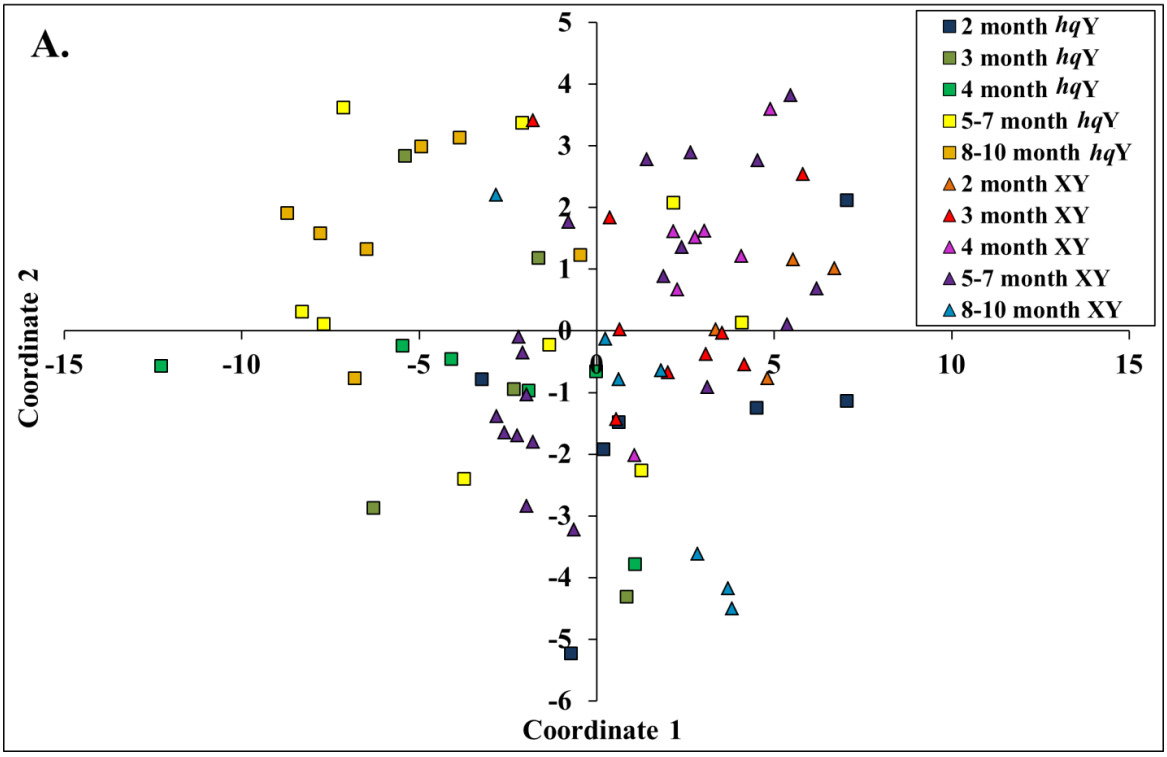
A.
2 month hqY
3 month hqY
4 month hqY
5-7 month hqY
8-10 month hqY
2 month XY
3 month XY
4 month XY
5-7 month XY
8-10 month XY
Coordinate 2
Coordinate 1
5
4
3
2
1
0
-1
-2
-3
-4
-5
-6
-15
-10
-5
0
5
10
15

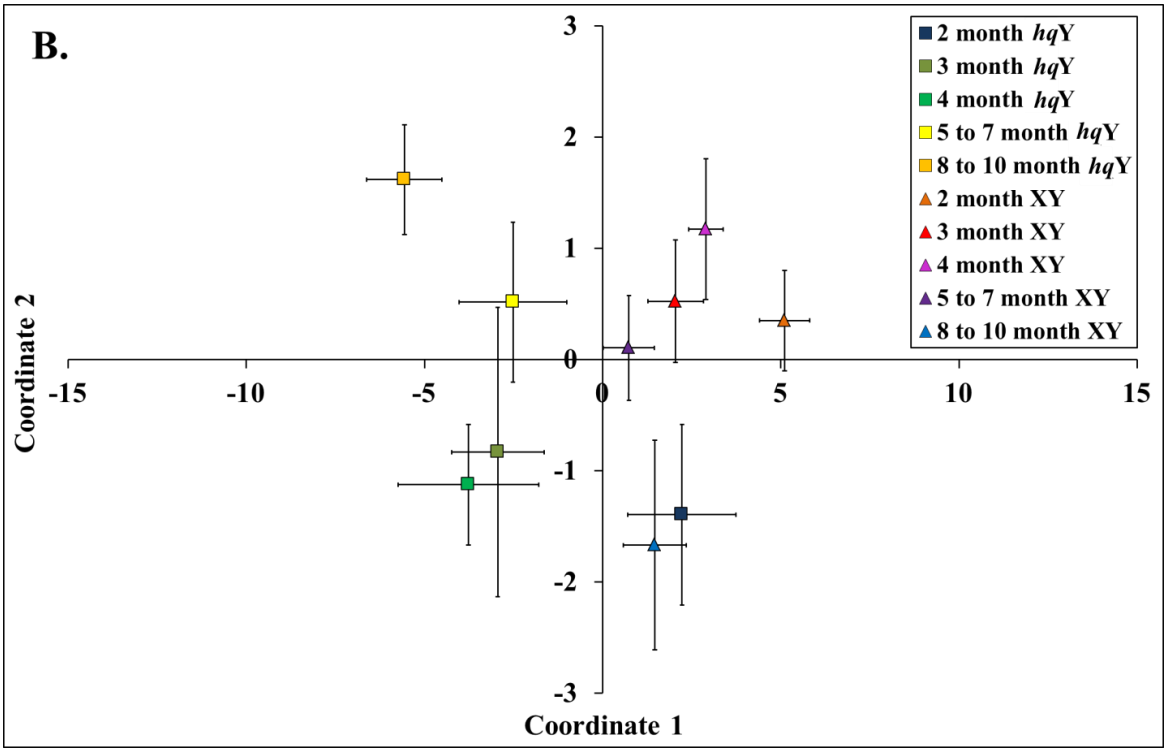
B.
2 month hqY
3 month hqY
4 month hqY
5 to 7 month hqY
8 to 10 month hqY
2 month XY
3 month XY
4 month XY
5 to 7 month XY
8 to 10 month XY
Coordinate 2
Coordinate 1
3
2
1
0
-1
-2
-3
-15
-10
-5
0
5
10
15

**Figure 3.6. *hq*Y time-domain OP parameters indicate early (two months) losses of INL and GCL periodicity and reduced retinal continuity at later ages.** (**A**) Young *hq*Y mice cluster distinctly from young, wild-type mice at two months of age as a result of reduced OP amplitudes and OP latencies. Progression of the *hq* disease leads to continued loss of OP amplitude (particularly OP4 and OP5) and latencies across all other age groups (months) resulting in severe losses of INL and GCL function. *hq* retina degeneration shows great inter-animal variation. Young, wild-type mice at two months demonstrate high OP amplitudes and short OP latency responses indicative of healthy retinal responses and have marginal declines from ages two through seven months. By eight to ten months, wild-type retinal function begins to decline with delayed OP latency and decreasing OP amplitudes. (**B**) The average coordinates for each cohort were plotted to assist with interpretation of NMDS clustering. Error bars represent ± 1 standard error of the mean. Stress is equal to 11.31%.

### *3.7 NMDS of frequency-domain OP parameters reveal distinct clustering of young hqY mice associated with decreased OP power, energy and frequency*

The stress associated with modelling all 12 frequency-domain variables from the severe *hq*Y disease progression study into a two-dimensional scale was 5.67%. Pearson's correlation coefficients were used for axis interpretation following NMDS of *hq*Y OP frequency-domain parameters (Appendix B, Table B.3). Coordinate 1 is highly correlated with decreasing energy and frequency and slightly correlated with decreasing power at all flash intensities (Figure 3.7). Coordinate 2 is highly correlated to decreasing power and highly correlated to increasing OP frequencies at all flash intensities (Figure 3.7). Wild-type and *hq*Y mice cluster distinctly at two months of age with *hq*Y mice demonstrating immediate lower total OP power, energy and frequency (Figure 3.7A). Distinctive *hq*Y clustering continues across all ages with progressive reductions of OP frequency, power and energy (Figure 3.7A). Inter-animal variation is much higher in the *hq*Y mice, likely due to variation in the severity of retinal degeneration occurring in the *hq*Y mice (Figure 3.7A). Young, wild-type mice cluster with high OP energy, power and frequency and with only marginal reductions in any parameter with age (Figure 3.7A).

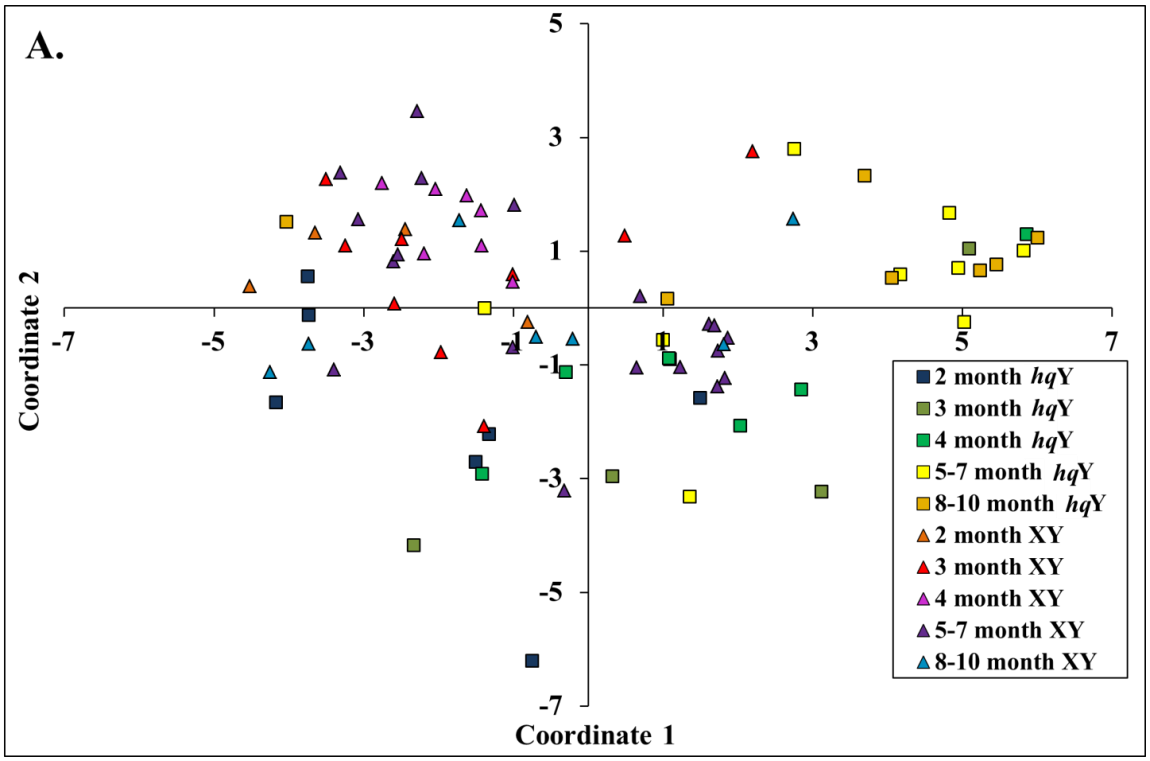
A.
Coordinate 2
Coordinate 1
5
3
1
-1
-3
-5
-7
-7
-5
-3
-1
1
3
5
7
2 month hqY
3 month hqY
4 month hqY
5-7 month hqY
8-10 month hqY
2 month XY
3 month XY
4 month XY
5-7 month XY
8-10 month XY

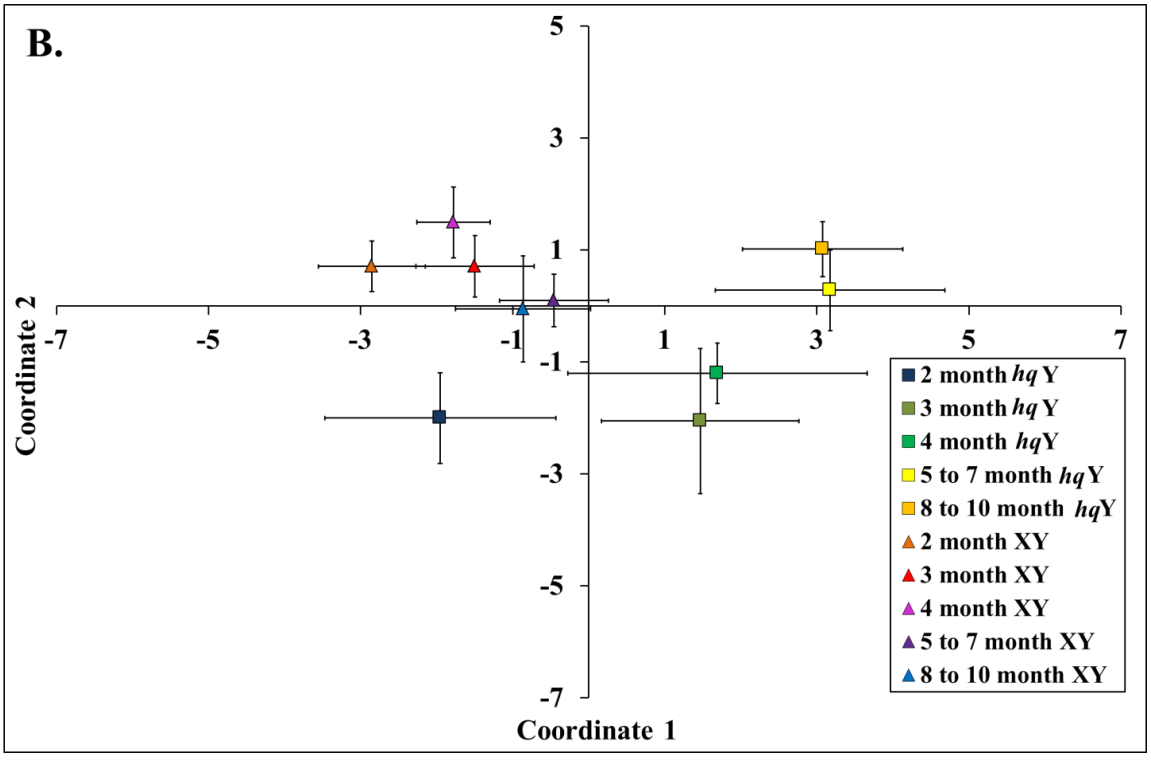
B.
Coordinate 2
Coordinate 1
5
3
1
-1
-3
-5
-7
-7
-5
-3
-1
1
3
5
7
2 month hq Y
3 month hq Y
4 month hqY
5 to 7 month hq Y
8 to 10 month hqY
2 month XY
3 month XY
4 month XY
5 to 7 month XY
8 to 10 month XY

**Figure 3.7. *hq*Y frequency-domain OP parameters reveal distinct loss of overall retinal periodicity and continuity of the INL and GCL response as early as two months.** (**A**) Young *hq*Y and wild-type mice cluster distinctly demonstrating an immediate reduction in overall OP frequency, power and total energy and loss of retinal function. Aging of *hq*Y mice (three-ten months) leads to progressive loss of all frequency-domain OP parameters. Severe losses in OP energy and frequency are most prominent between two and three months of age in *hq*Y mice. Young, wild-type mice (two months) cluster with high OP frequency, power and total energy and have slight age related decreases (three to ten months). Progression of aging in wild-type mice shifts NMDS parameters similar to that of young *hq*Y mice (two months). (**B**) The average coordinates for each cohort were plotted to assist with interpretation of NMDS clustering. Old wild-type mice cluster similarly with young *hq* disease mice. Error bars represent ± 1 standard error of the mean. Stress is equal to 5.67%.

### *3.8 NMDS of hq heterozygote time-domain parameters expose distinct clustering at eleven and fifteen months of age*

The stress associated with modelling all 32 time-domain variables from the moderate *hq*X disease progression study into a two-dimensional scale was 9.84%. Pearson's correlation coefficients were used for axis interpretation following NMDS (Appendix B, Table B.4). The x-axis (Coordinate 1) is highly correlated to short OP latencies, particularly of OP2 and OP3 as well as high OP3 and OP4 amplitudes (Figure 3.8). The y-axis (Coordinate 2) is highly correlated to decreasing OP amplitudes across all flash intensities (Figure 3.8). Young *hq* carrier and wild-type mice (three months) cluster together with long OP latencies and intermediate amplitudes (Figure 3.8A). However by eleven months, *hq* mice shift towards decreased OP amplitudes and shorter latencies indicative of enhanced periodicity but loss of continuity of neural feedback response. By fifteen months of age *hq* carrier mice demonstrate a large delay in OP latencies with small OP amplitudes resulting in overall decreased retinal function (Figure 3.8A). Aging of wild-type mice (eleven and fifteen months) is associated with marginal decreases in OP amplitudes and enhanced OP latencies (Figure 3.8A).

### *3.9 NMDS of frequency-domain hq carrier mice OP parameters demonstrate progressive loss of OP power and energy at eleven and fifteen months*

The stress associated with modelling all 12 frequency-domain variables from the moderate *hq*X disease progression study into a two-dimensional scale was 3.84%. Pearson's correlation coefficients were used for axis interpretation following NMDS of

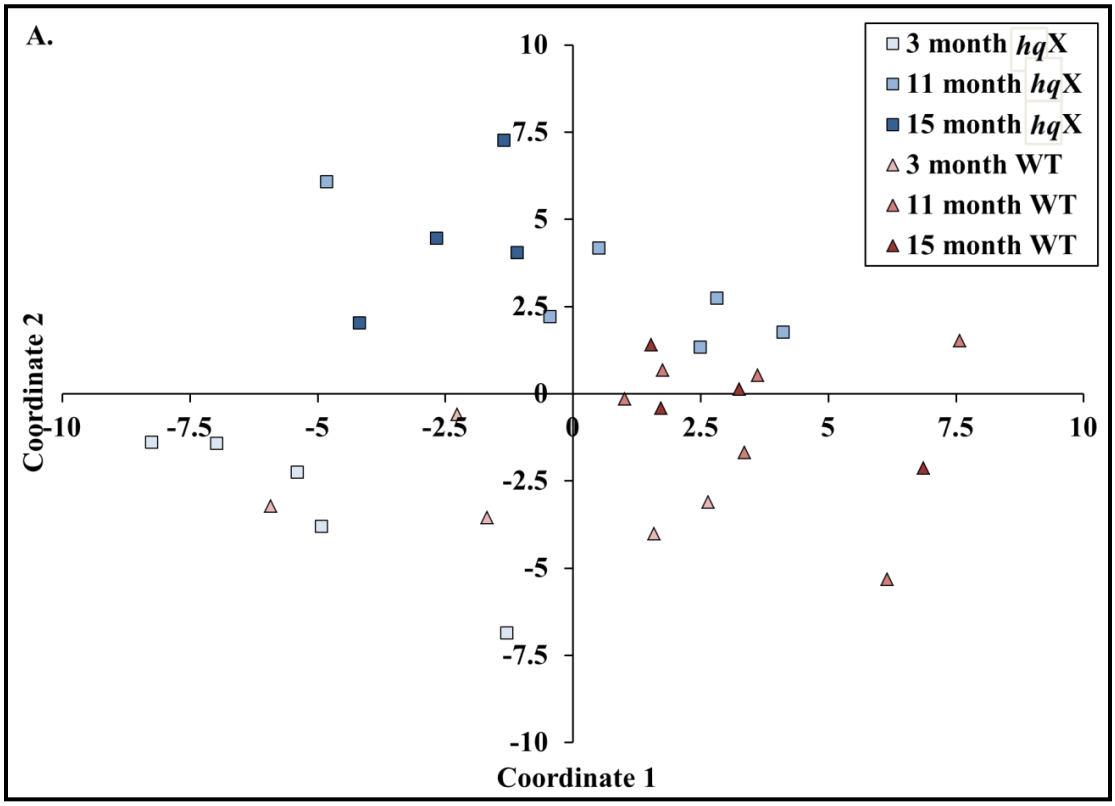
A.
3 month hqX
11 month hqX
15 month hqX
3 month WT
11 month WT
15 month WT
Coordinate 2
Coordinate 1
10
7.5
5
2.5
0
-2.5
-5
-7.5
-10
-10
-7.5
-5
-2.5
0
2.5
5
7.5
10

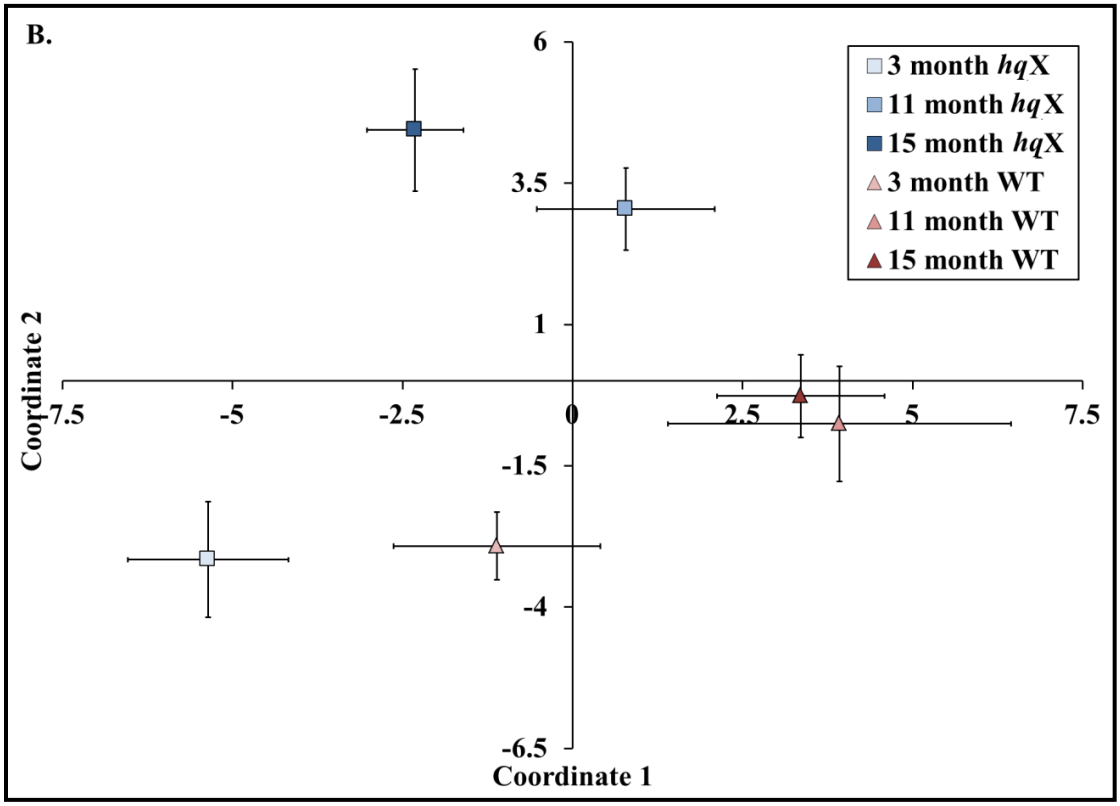
B.
3 month hqX
11 month hqX
15 month hqX
3 month WT
11 month WT
15 month WT
Coordinate 2
Coordinate 1
6
3.5
1
-1.5
-4
-6.5
-7.5
-5
-2.5
0
2.5
5
7.5

**Figure 3.8. *hq* carrier time-domain OP parameters demonstrates distinct clustering at 11 and fifteen months associated reduced initial INL/GCL response and decreased continuity of overall retinal response.** (**A**) Young *hq* carrier and wild-type mice cluster similarly with reduced OP initial latency and intermediate amplitudes at three months of age. This is indicative of reduced photoreceptor and INL and GCL periodicity and continuity of INL and GCL function at a young age. By eleven months of age, *hq* carrier mice demonstrate distinct clustering associated with delayed initial OP latency and a reduction in OP amplitudes when compared to age-matched wild type. As the *hq* disease progresses, further reductions are evident in both OP initial latency and amplitudes at fifteen months and as a result of incomplete retinal function. Aging of wild-type mice is associated with marginal decreases in OP amplitude and increases in OP latencies and ultimately little change in retinal function. (**B**) The average coordinates of each age cohort were plotted to assist with interpretation of NMDS clustering. Error bars represent ± 1 standard error of the mean. Stress is equal to 9.84%.

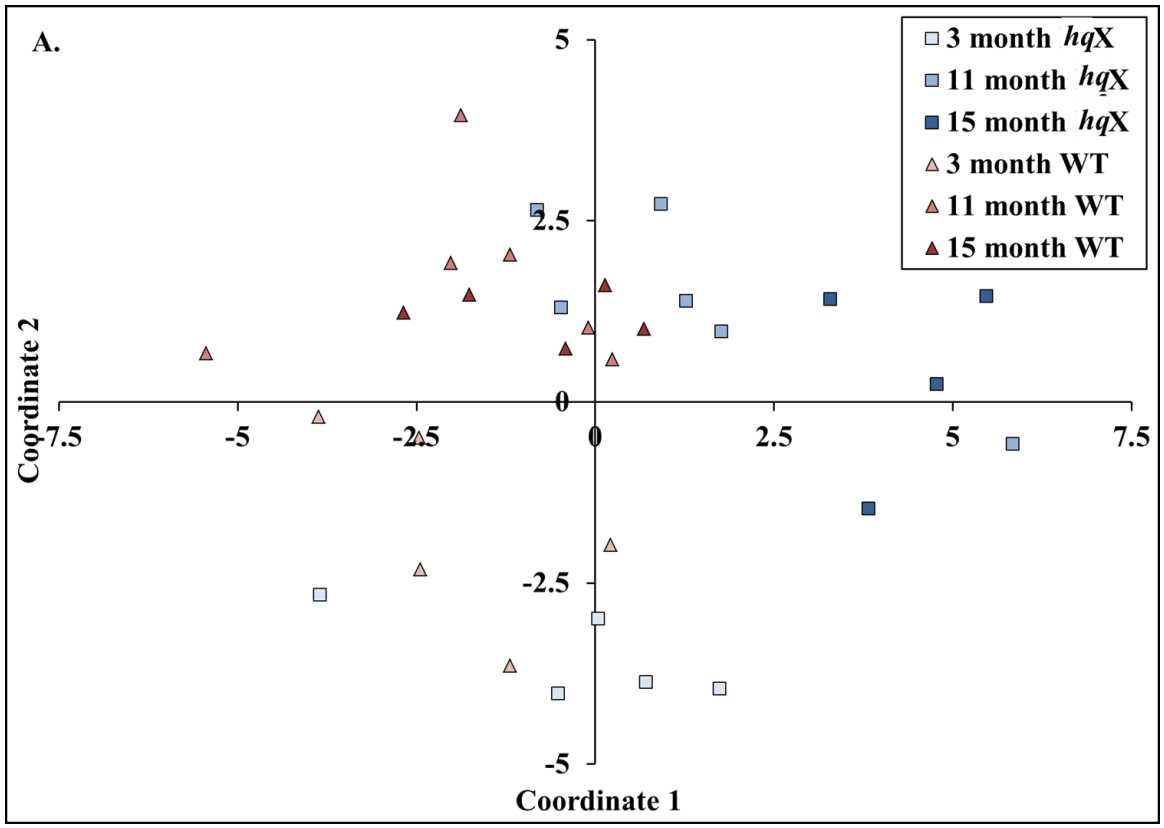
A.
3 month hqX
11 month hqX
15 month hqX
3 month WT
11 month WT
15 month WT
5
2.5
0
-2.5
-5
-7.5
-5
-2.5
0
2.5
5
7.5
Coordinate 2
Coordinate 1

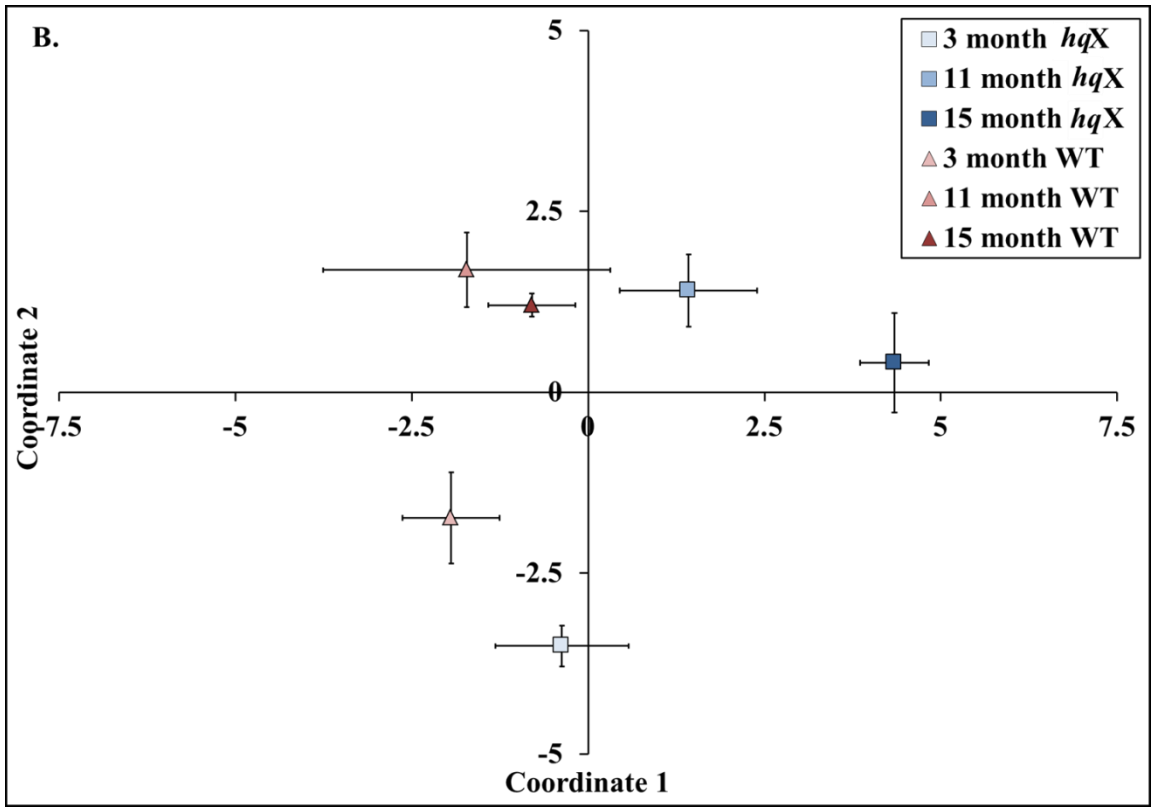
B.
3 month hqX
11 month hqX
15 month hqX
3 month WT
11 month WT
15 month WT
5
2.5
0
-2.5
-5
-7.5
-5
-2.5
0
2.5
5
7.5
Coordinate 2
Coordinate 1

**Figure 3.9. Frequency-domain OP parameters of *hq* carrier mice indicates distinct clustering associated with INL and GCL dysfunction at eleven and fifteen months.** (**A**) Young (three months) *hq*X and wild-type mice cluster similarly based upon high OP power and energy and low frequency. *hq* disease progression at eleven months is indicative of large reductions in total OP power and energy as well as increased OP frequency. Further reductions of OP power and energy are evident at fifteen months with additional reduced OP frequency. Aging of wild-type mice is associated with increases in OP frequencies and minimal reductions in overall OP total power and energy. (**B**) The average coordinates for each cohort were plotted to assist with interpretation of NMDS clustering. Error bars represent ± 1 standard error of the mean. Stress is equal to 3.84%.

*hq*X OP frequency-domain parameters (Appendix B, Table B.5). The x-axis (Coordinate 1) is highly negatively correlated to both OP total energy and power across all flashes while the y-axis (Coordinate 2) is highly positively correlated to frequency across all flashes (Figure 3.9). *hq* carrier and wild-type mice cluster similarly at three months of age with *hq*X mice demonstrating slightly lower OP frequency, power and energy (Figure 3.9A). By eleven months of age, *hq* carrier mice cluster distinctly with higher OP frequency and significantly reduced OP power and energy (Figure 3.9A). This general trend progresses as *hq* carrier mice progress to older ages with further reductions in OP power and energy indicative of reduced continuity of INL and GCL retinal response (Figure 3.9A). Aging of wild-type mice is associated with increases in OP frequency and marginal decreases in OP power and energy (Figure 3.9A).

### *3.10 hq mice maintain blood retinal barrier integrity at both a young and old age*

To estimate concentrations of the Evans Blue (EB) dye in tissue, a standard curve was created through a series of dilutions of EB in formamide. EB dye dissolved in formamide maintain a linear relationship between 250 to 10000 ng/mL (Figure 3.10A, $r^2 = 0.999$, $y = 7.87 \times 10^{-6}x + 0.002$). The liver is a region of full vascularization and therefore no blood endothelial barrier is present. To infer sensitivity of the assay a series of tests were performed as described below. Significantly more EB was found in the liver of EB injected wild-type mice than in uninjected controls ($n = 4$ per cohort, One-way ANOVA, $p < 0.001$). No significant difference in EB amount was found in the retina of wild-type mice injected with EB and uninjected wild-type mice ($n = 4$ per cohort, One-way ANOVA, $p > 0.05$) indicating an intact BRB in wild-type mice. In addition, wild-

type mice show significantly more EB in liver than retina at both a young and old age (Figure 3.10 B, n = 4 per cohort, Two-way ANOVA, $p < 0.005$) but no significant reduction with age (Figure 3.10B, n=4 per cohort, Two-way ANVOA, $p > 0.05$). *hq* mice show a similar trend with significantly more EB in the liver than retina at both ages (Figure 3.10 C, Two-way ANOVA, $p < 0.005$) but no significant reduction with age (Figure 3.10C, Two-way ANOVA, $p > 0.05$). In order to account for technical variation, retina EB amount was normalized to liver EB amount and no significant difference in retina/liver ratio was found across all cohorts indicating a similar amount of EB is present in the retina across all cohorts. This evidence suggests that there is no degradation of the BRB in *hq* mice (Figure 3.10, Two-way ANOVA, $p > 0.05$).

### *3.11 Pathway analysis reveals differential expression of focal adhesion, extracellular remodeling, cell stress and inflammation in the four-month hq retina*

Four-month-old *hq* retinal gene expression microarray data (n=3 per cohort) previously performed by A. Laliberté (2010),[103] was filtered using selection criteria set at a 1.75 fold change (mRNA transcript level) and a p-value less than 0.05. This revealed a total of 521 genes that were differentially expressed between retinal tissue from *hq*Y mice and age-matched wild-type mice. A total of 182 genes were downregulated by greater than 1.75 fold, and a total of 339 were upregulated by greater than 1.75 fold. KEGG pathway analysis revealed pathways with significant proportions of differentially expressed genes. Significant pathways involved in extracellular remodelling, ABC transport, immune response, inflammation, cell cycle and p53 signalling were

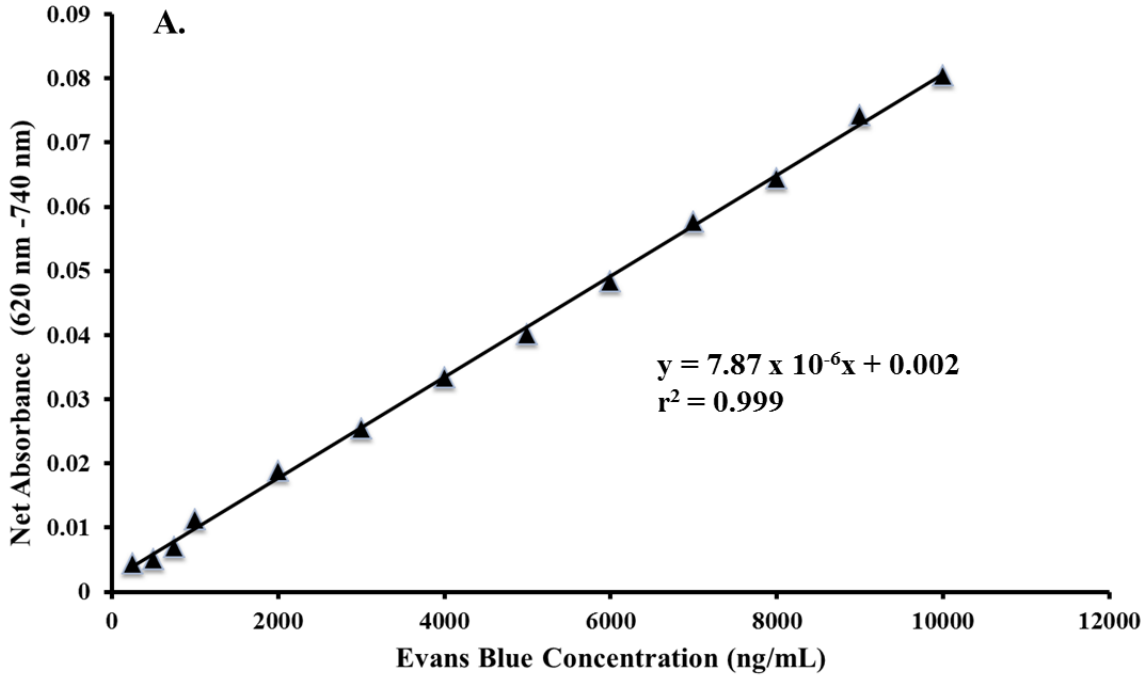
A.
Net Absorbance (620 nm -740 nm)
Evans Blue Concentration (ng/mL)
y = 7.87 x 10-6x + 0.002
r2 = 0.999

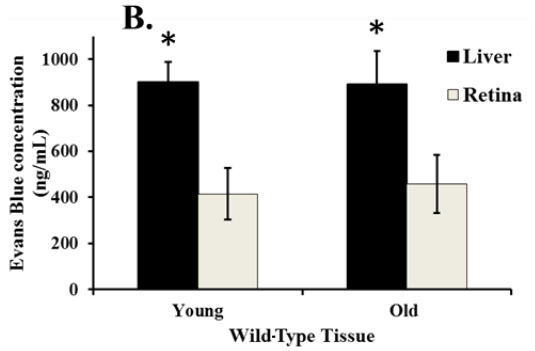
B.
Evans Blue concentration (ng/mL)
Liver
Retina
Young
Old
Wild-Type Tissue

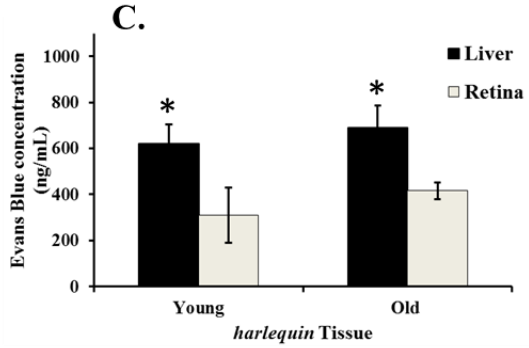
C.
Evans Blue concentration (ng/mL)
Liver
Retina
Young
Old
harlequin Tissue

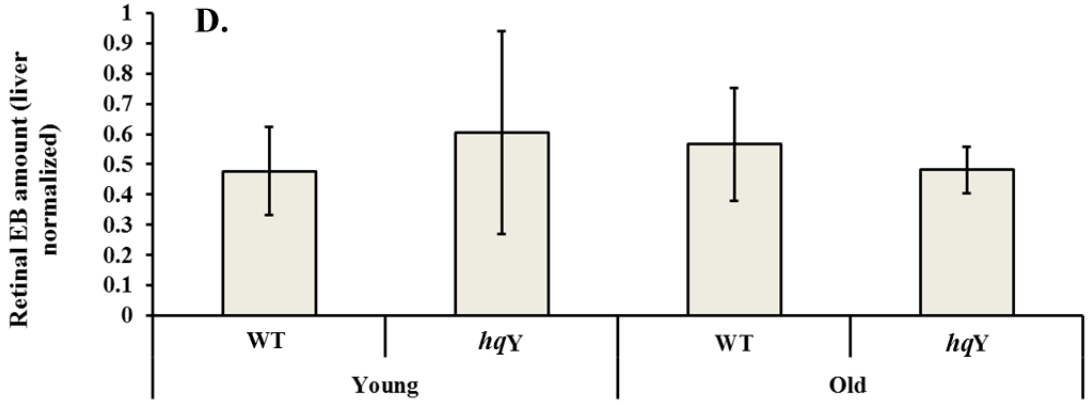
D.
Retinal EB amount (liver normalized)
WT
hqY
WT
hqY
Young
Old

**Figure 3.10. *hq*Y mice maintain a blood-retinal-barrier similar to that of age-matched wild-type mice.** (**A**) Evans Blue standards in formamide maintain a linear relationship between concentration and background-subtracted absorbance ($r^2 = 0.999$, $y = 7.87 \times 10^{-6}x + 0.002$). Standards were tested by three different people in triplicate and were virtually identical. (**B**) A significantly higher concentration of Evans Blue dye is present in the liver in comparison to retina in wild-type mice at both ages. (**C**) Similarly, a significantly higher concentration of Evans Blue dye is present in the liver of *hq*Y mice in comparison to retina across both ages. (**D**) Liver-normalized retinal Evans Blue amount is not significantly different across any cohort indicating an intact blood-retinal barrier.

differentially expressed in the *hq* retina ($p < 0.01$) (Table 3.1). Additional DNA repair and cancer pathways were also differentially expressed ($p < 0.05$) (Table 3.1).

KEGG pathway analysis allowed for a comprehensive overview of differential expression in the *hq* mouse retina. However, due to the nature of KEGG gene annotations (not retinal specific) and containing only single genetic isoforms, only 177 gene IDs out of the 521 were represented the software analysis. Therefore, well over 65% of genes differentially expressed in the expression microarray were not used by KEGG pathway software. To account for this bias, a manual annotation of all differentially expressed genes was performed (Appendix E). A thorough review yielded an alternative metabolism theme, common amongst AIF knock-downs including; the upregulation of glucose metabolism, lactate acidosis, and glycerol metabolism. Genes present in these pathways were selected for Taqman® qPCR analysis (Table 3.2).

### *3.12 Cerebellar and retinal RNA quality was assessed prior to transcriptional analysis*

Spectrophotometry, gel electrophoresis and Bioanalyzer spectra all indicated the presence of high quality cerebellar RNA. Cerebellar samples were only chosen if they indicated a concentration greater than 140 ng/uL and a high absorbance ratio ($A260/A280 > 1.8$) (Appendix B, Table B.7). Gel electrophoresis allowed quantification of the 28S and 18S ribosomal RNA (rRNA) subunits as well as the potential for gDNA contamination. Samples were only selected if they demonstrated distinct rRNA subunits with no gDNA contamination (Figure 3.12). Samples were also analyzed via Bioanalyzer spectra and selected if there was clear separation of 28S and 18S peaks (Figure 3.13A)

**Table 3.1. KEGG pathway analysis based on microarray data of differentially expressed genes from retinal samples of four-month-old *hq* disease mice.*,†**

| Pathway | p-value‡ | Number of Differentially Expressed Genes | Gene Enrichment Percentage (%) |
|---|---|---|---|
| ECM-receptor interaction | $6.9 \times 10^{-6}$ | 13 | 2.5 |
| ABC transporters | $5.5 \times 10^{-5}$ | 9 | 1.8 |
| Focal Adhesion | $1.0 \times 10^{-4}$ | 18 | 3.5 |
| Viral myocarditis | $5.5 \times 10^{-4}$ | 11 | 2.1 |
| p53 signaling pathway | $4.9 \times 10^{-3}$ | 8 | 1.6 |
| Cell cycle | $5.7 \times 10^{-3}$ | 11 | 2.1 |
| Complement and coagulation cascades | $7.8 \times 10^{-3}$ | 8 | 1.6 |
| Tight junction | $8.2 \times 10^{-3}$ | 11 | 2.1 |
| Regulation of actin cytoskeleton | 0.015 | 14 | 2.7 |
| Pathways in cancer | 0.02 | 18 | 3.5 |
| Small cell lung cancer | 0.046 | 7 | 1.4 |

***** Microarray was performed by A. Laliberté (2010). [103]

† Pathway analysis was performed with the Database for Annotation, Visualization, and Integrated Discovery (DAVID) [National Cancer Institute at Frederick, Frederick, MD].[141,142]

‡ Pathway is ordered by increasing p-value.

**Table 3.2. Genes of interest from four-month-old *hq* mice selected from retinal microarray data for Taqman® validation.**

| Gene Name | Symbol | Function† | p-value | Fold Change |
|---|---|---|---|---|
| ***Adenylate cyclase 10*** | ***Adcy10*** | Key intracellular regulation of pH and bicarbonate buffering | 0.005 | +2.858 |
| ***Glycerol-3-phosphate dehydrogenase 2*** | ***Gpd2*** | Secondary step of glycerol metabolism, feeds into glycolysis | 0.04 | +2.377 |
| ***Aldehyde dehydrogenase 2*** | ***Aldh2*** | Primary step for conversion of Acetyl-CoA to acetate | 0.045 | +2.345 |
| ***Glycerol Kinase 5*** | ***Gk5*** | Primary step of glycerol metabolism, feeds into glycolysis | 0.048 | +1.998 |
| ***TBC1 domain family, member 4*** | ***Tbc1d4*** | Responsible for shuttling *Glut4* to the plasma membrane from the endoplasmic reticulum | 0.03 | +1.992 |
| ***Hexokinase 1*** | ***Hk1*** | Initial step of glycolysis in the retina – drives glycolytic rate | 0.037 | +1.964 |
| ***Glucose transporter, member 4‡*** | ***Glut4*** | Rapid, insulin dependent glucose transporter responsible for glucose intake in neurons | 0.023 | +1.4 |
| ***Lactate dehydrogenase C‡*** | ***Ldhc*** | Responsible for reverse reaction of L-lactate to pyruvate | 0.018 | -1.63 |
| ***Pyruvate dehydrogenase, component X*** | ***Pdhx*** | Structural component of pyruvate dehydrogenase complex | 0.016 | -2.482 |
| ***Sodium bicarbonate transporter, member 10*** | ***Slc4a10*** | Bicarbonate transporter to remove excess $CO_2$ from mitochondria | 0.027 | -2.873 |
| ***Apoptosis-inducing factor 1*** | ***Aif*** | Complex I efficiency and maintenance, apoptosis inducer. | 0.0002 | -6.012 |

† Functional annotation was based on NCBI, GENE search annotation [National Institute of Health, Bethesda, MD]

‡ Previous literature suggests increased glucose metabolism and lactate acidosis in *hq* mice, therefore *Glut4* and *Ldhc* ($p < 0.05$, $< 1.75$ fold change) were added for examination.

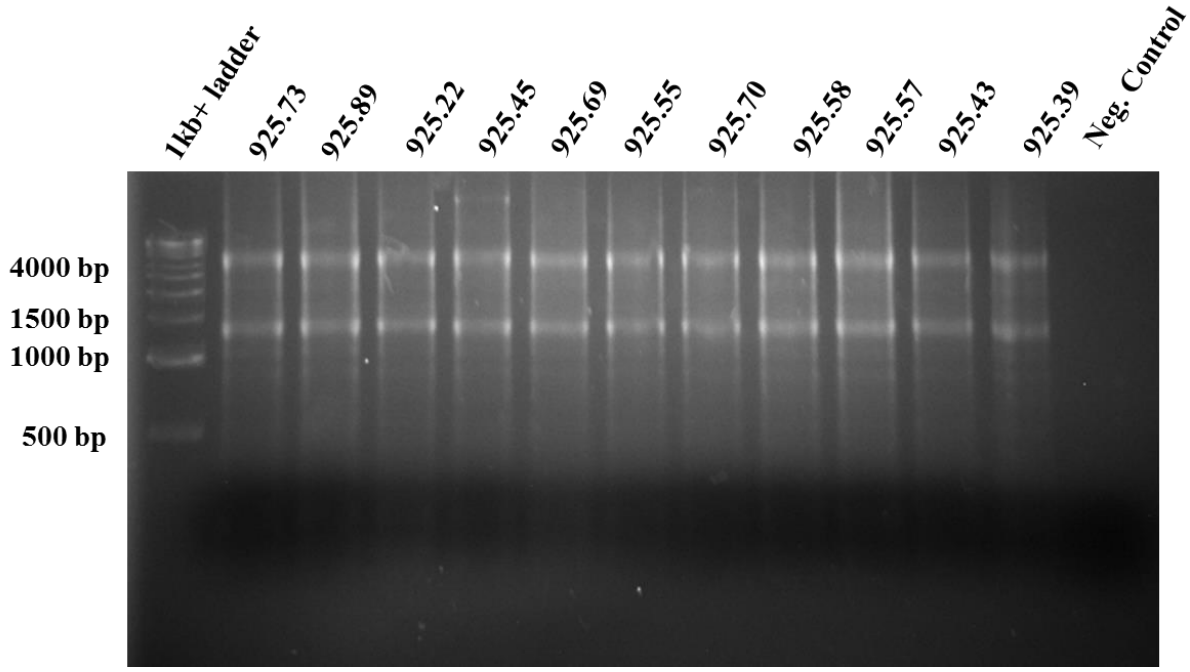


**Figure 3.11. Agarose gel electrophoresis demonstrates high quality cerebellar RNA samples with distinct 28S and 18S ribosomal subunits.** A representative gel of 11 samples indicates the presence of high quality cerebellar RNA (distinct 28S and 18S bands) electrophoresed with a 1 kb+ DNA ladder [Life Technologies, Burlington, ON]. Sample 925.45 (lane 5) presented contamination with high molecular weight gDNA. A negative control of water was electrophoresed in the final lane (lane 13).

**A.**

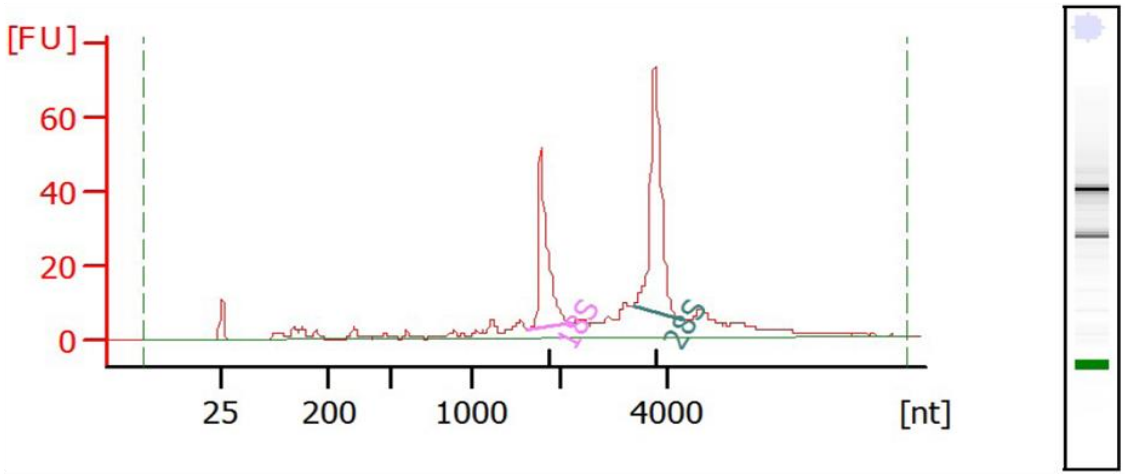
[FU]
60
40
20
0
18S
28S
25
200
1000
4000
[nt]

**B.**

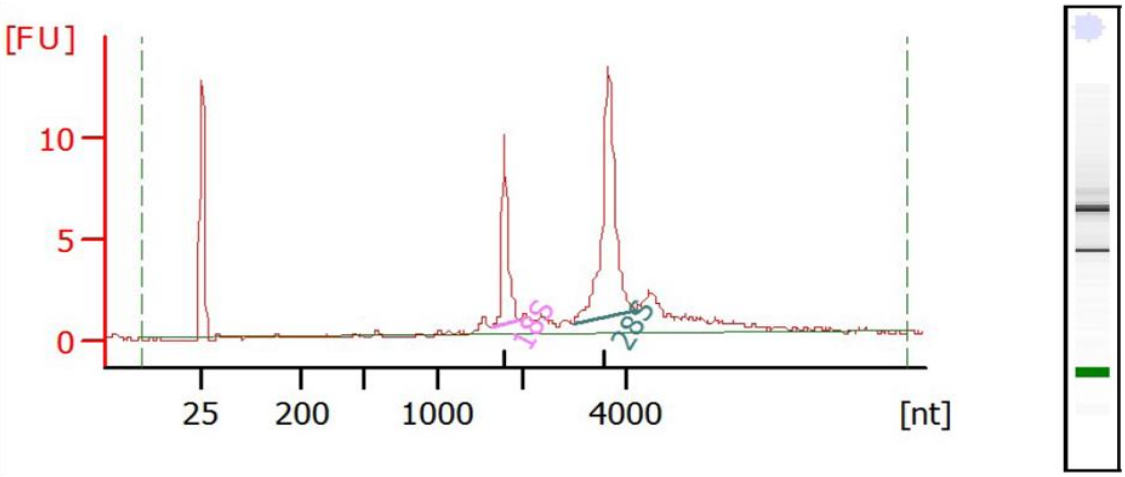
[FU]
10
5
0
18S
28S
25
200
1000
4000
[nt]

**C.**

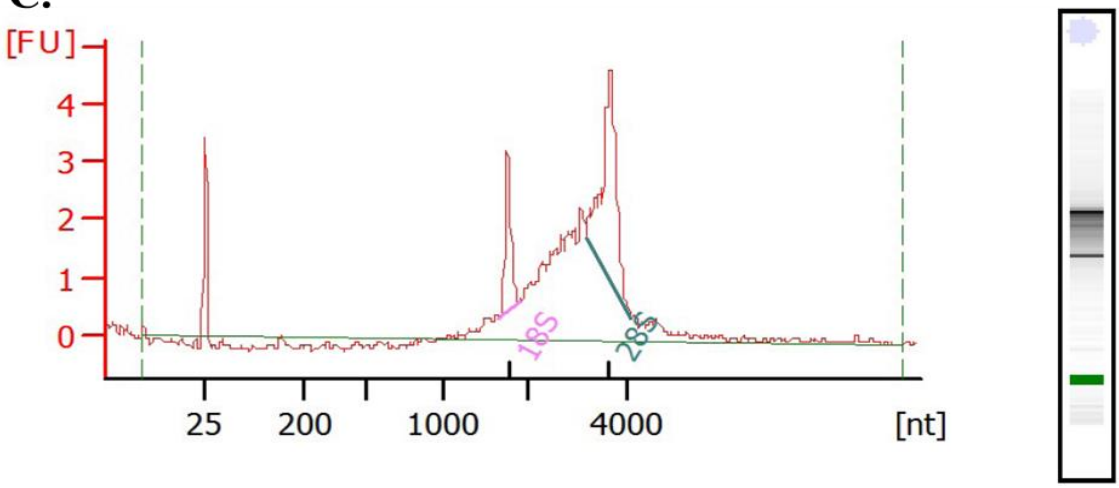
[FU]
4
3
2
1
0
18S
28S
25
200
1000
4000
[nt]

**Figure 3.12. Electropherograms indicate high RNA quality of both cerebellar and retinal samples.** (**A**) A representative electropherogram of intact, high quality cerebellar RNA using the Agilent 2100 Bioanalyzer [Agilent Technologies Inc., Palo Alto, CA]. RNA quality is a measure of fluorescence (FU) and nucleotide (nt) size. An initial fluorescence peak at 25 nt represents a size marker, followed by a clear distinction of the 18S (~1500 nt) and 28S rRNA subunits (~4000 nt). A representative agarose gel image is created (right hand side) based on fluorescence of rRNA peaks. (**B**) A representative electropherogram of intact, high quality retinal RNA. Fluorescence is much lower due to a lower concentration, however a clear separation of the 18S and 28S rRNA subunits is still evident. (**C**) A retinal RNA electropherogram with gDNA contamination. Sheared gDNA and degradation products show similar properties to the 28S rRNA subunit and lead to skewing of the rRNA peak.

as well as an RNA integrity number (RIN) greater than 8. Retinal samples were subject to the same spectrophotometric (concentration > 16 ng/uL) and Bioanalyzer assessment (Figure 3.13B) (Appendix B, Table B.7). Gel electrophoresis was not performed with retinal samples as the RNA concentrations were too low. All retinal RNA samples used for transcriptome analysis were of high quality.

### *3.13 Taqman® quantitative PCR confirms metabolic and cell regulation changes in the hq mice retina and cerebellum*

*Aif* was significantly downregulated ($p < 0.001$, fold change < 11.312) in the *hq* retina at four months, three months, and two months (Table 3.3) of age as well as significantly ($p < 0.001$, fold change = -8.8183) downregulated in the four-month *hq* cerebellum (Table 3.4). *Cyclin-dependent kinase inhibitor 1A* (*Cdkn1a),* responsible for inhibiting cell cycle, was significantly ($p < 0.05$) upregulated in the *hq* retina at four months, three months and two months of age (Table 3.3) as well as the four-month cerebellum (Table 3.4). Genes associated with metabolism were upregulated in the four-month *hq* retina (Table 3.3) including; *Adcy10* ($p = 0.0013$, fold change = +1.7995), *Slc4a10* ($p = 0.0024$, fold change = 1.8102), *Gk5* ($p = 0.0021$, fold change = +1.7995), *Aldh2* ($p = 0.017$, fold change = +1.660), *Gpd2* ($p = 0.023$, fold change = +1.274) and *Pdhx* ($p = 0.027$, fold change = +1.250). No genes involved in metabolism were differentially regulated in the three-month *hq* retina (Table 3.3). However, *Gk5* ($p = 0.022$, fold change = +1.2688) and *Aldh2* ($p = 0.0465$, fold change = +1.289) were found to be differentially expressed early in the two- month *hq* retina (Table 3.3). One metabolism gene was found to be differentially expressed in the four-month *hq* cerebellum (Table 3.4); *Adcy10* ($p = 0.0265$, fold change = +2.2422).

**Table 3.3. Differential gene expression of selected genes in the *hq* retina at two, three and four months of age based on Taqman® RT-PCR.***

| Gene Name | Two months Fold change‡ (p-value†) | Three months Fold change‡ (p-value†) | Four months Fold change‡ (p-value†) |
|---|---|---|---|
| ***Aifm1*** | **- 12.315 (<0.001)** | **- 17.301 (<0.001)** | **- 11.312 (<0.001)** |
| ***Adcy10*** | + 1.7285 (0.0878) | + 1.5042 (0.6607) | **+ 1.7995 (0.0013)** |
| ***Gk5*** | **+ 1.2688 (0.0219)** | + 1.0664 (0.60) | **+ 1.8102 (0.0021)** |
| ***Slc4a10*** | + 1.1164 (0.1655) | + 1.0728 (0.4052) | **+ 1.4990 (0.0024)** |
| ***Cdkn1a*** | **+ 2.2391 (0.0334)** | **+ 1.6654 (0.0053)** | **+ 3.2214 (0.0063)** |
| ***Aldh2*** | **+ 1.2889 (0.0465)** | - 1.0963 (0.5967) | **+ 1.660 (0.017)** |
| ***Gpd2*** | + 1.2586 (0.1036) | - 1.106 (0.6446) | **+ 1.274 (0.023)** |
| ***Pdhx*** | +1.1222 (0.1319) | +1.0285 (0.6297) | **+1.250 (0.027)** |
| *Hk1* | + 1.1442 (0.1780) | - 1.007 (0.997) | + 1.286 (0.060) |
| *Rn18s* | + 1.4432 (0.3058) | + 1.0531(0.7299) | + 1.361 (0.270) |
| *Tbc1d4* | + 1.2331 (0.2442) | n/a | + 1.091 (0.344) |
| *Glut4* | + 3.2467 (0.1107) | - 2.8596 (0.3161) | - 2.898 (0.832) |
| *Ldhc* | n/a | n/a | n/a |

* Gene order was established by ascending four month p-value, bold genes indicate significance.

† An ANOVA was used in Excel [Microsoft, Redmond, VA] to determine significance of the ΔCt values.

‡ Fold change was determined with DataAssist™ software [Life Technologies, Burlington, ON] using the comparative Ct (ΔΔCt) method.[140]

n/a - indicates late amplification.

**Table 3.4. Differential gene expression of selected genes in the *hq* cerebellum at four months of age based on Taqman® RT-PCR.***

| Gene Name | p-Value† | Fold Change‡ |
|---|---|---|
| ***Aifm1*** | **<0.001** | **- 8.8183** |
| ***Cdkn1a*** | **0.0251** | **+ 1.6291** |
| ***Adcy10*** | **0.0265** | **+ 2.2422** |
| *Slc4a10* | 0.1409 | + 1.4275 |
| *Tbc1d4* | 0.1409 | + 1.2278 |
| *Glut4* | 0.1624 | + 1.6189 |
| *Gk5* | 0.1792 | + 1.4212 |
| *Pdhx* | 0.2217 | + 1.1763 |
| *Rn18s* | 0.2776 | + 1.3111 |
| *Hk1* | 0.4030 | + 1.1589 |
| *Gpd2* | 0.4065 | + 1.1127 |
| *Aldh2* | 0.4159 | + 1.1105 |
| *Ldhc* | n/a | n/a |

* Gene order was established on ascending p-value, bolded genes indicate significance.

† An ANOVA was used in Excel [Microsoft, Redmond, VA] to determine significance of the ΔCt values.

‡ Fold change was determined with DataAssist™ software [Life Technologies, Burlington, ON] using the comparative Ct (ΔΔCt) method.[140]

n/a - indicates late amplification.

### *3.14 hqY mice have a decreased total body mass but display hyperphagia at four months*

The mean body mass of *hq*Y diseased mice at four months (22.422 ± 0.9993g) was significantly lower ($p < 0.001$) than age-matched wild-type mice (29.512 ± 0.5362g) (Figure 3.13A) with a 24% reduction in total body mass. Although *hq*Y mice exhibit smaller mean body mass, they display hyperphagia at four months with a significant increase ($p < 0.001$) in mean food consumption (0.1991 ± 0.01 grams of food/gram of body mass/day) in comparison to the wild type. This overall increase is nearly 34.4% (0.1481 ± 0.002 grams of food/gram of body mass/day) in *hq*Y mice (Figure 3.13B).

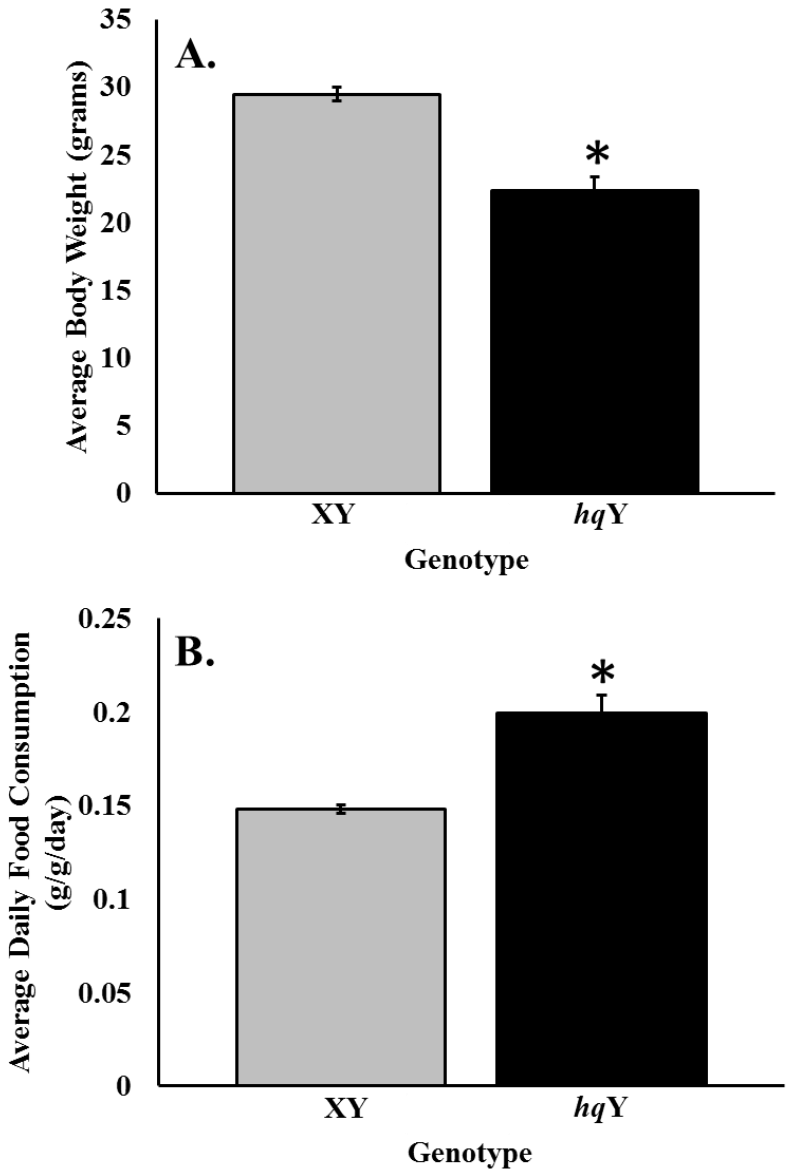


**Figure 3.13. Feeding study indicates hyperphagia in *hq* mice at four months of age.** (**A**) *hq* mice demonstrate a significantly lower mean body mass in comparison to age-matched wild-type mice. (**B**) Mean daily food consumption was significantly higher in *hq* disease mice indicating hyperphagia. Sample size was four per cohort, asterisks indicate significance (*$p < 0.001$) and error bars represent ± 1 standard error of the mean.

# Chapter 4. Discussion

## *4.1 Early hq retinal dysfunction can be tracked to the inner retina through the study of oscillatory potentials*

Previously, it was shown that OXPHOS dysfunction in the *hq* retina is associated with parainflammatory disease as early as 1.8 months of age, resulting in microglial migration to the ONL and subsequent ONL cells losses.[103,104] To date, early mechanisms prompting retinal degeneration in the *hq* mouse have yet to be elucidated. It was predicted that oscillatory potentials could be used to track *hq* disease progression because of their association with *hq* hallmarks of the retinal disease including degeneration of the ONL, IPL, OPL as well as ganglion and amacrine cells. Herein, at the retinal physiological level, *in vivo* diagnosis of electrophysiological response in the *hq* retina was able to identify early, diagnostic candidates of retinal malfunction including OP frequency and initial latency. NMDS provided a thorough visualization of OP waveforms across multiple flash intensities and identified changes across all measured parameters of OP profiles.

Due to the highly metabolic nature (continuous transport) of the BRB, it was unknown whether the severe neurodegeneration in the *hq* retina was the result of BRB degradation or endogenous retinal stress caused by reduced AIF function. Loss of BRB integrity leading to exogenous antigens larger than the Evans Blue albumin complex traversing the BRB was rejected as a proposed mechanism for chronic microglial activation in the *hq* retina. Thus, triggers of chronic microglial activation are hypothesized to be the result of an endogenous cellular stress mechanism. Early transcriptome changes in the *hq* retina are consistent with partial compensating metabolic

mechanisms in an attempt to maintain production of ATP *in vivo*. Such as, glycerol metabolism to generate $FADH_2$ which enters OXPHOS distal to NADH dehydrogenase. This study provides the first, *in vivo*, preliminary evidence for alternative metabolism in the retina of the *hq* mouse and is the basis for subsequent future examinations of *hq* retinal metabolism.

### *4.2 Oscillatory potentials are relevant for the study of hq retinal degeneration*

Oscillatory potentials (OPs) are the intermediate peaks on the ascending limb of the ERG b-wave. OPs are believed to correspond to inner retinal function of the ON-, OFF- and feedback mechanisms of the INL and GCL. OP subgroups, beginning with intermediate OPs represent the proximal action-potential independent (bipolar and horizontal cell graded potentials) and action-potential dependent mechanisms of ganglion cells and amacrine cells of the inner retina (Figure 4.1).[56] Additionally, the interplexiform cell which spans the OPL and IPL may generate radial current flow (feedback) from lateral synapses of the OPL and IPL and may be responsible for oscillations.[54,55] This is particularly beneficial for the study of *hq* retinal degeneration. Neurites of the OPL and IPL contain the synapse between dendrites and axons of adjacent neurons relaying electrochemical signal from the OS. They are the most energetic region of the neurons and hence *hq* mice exhibit considerable thinning of the neurites[93] as well as upregulation of neurite remodelling and maintenance genes.[103] These genes include; *Sodium channel beta 4 subunit* (*Scn4b*), and *Sterile alpha motif domain containing 4* (*Samd4*) both of

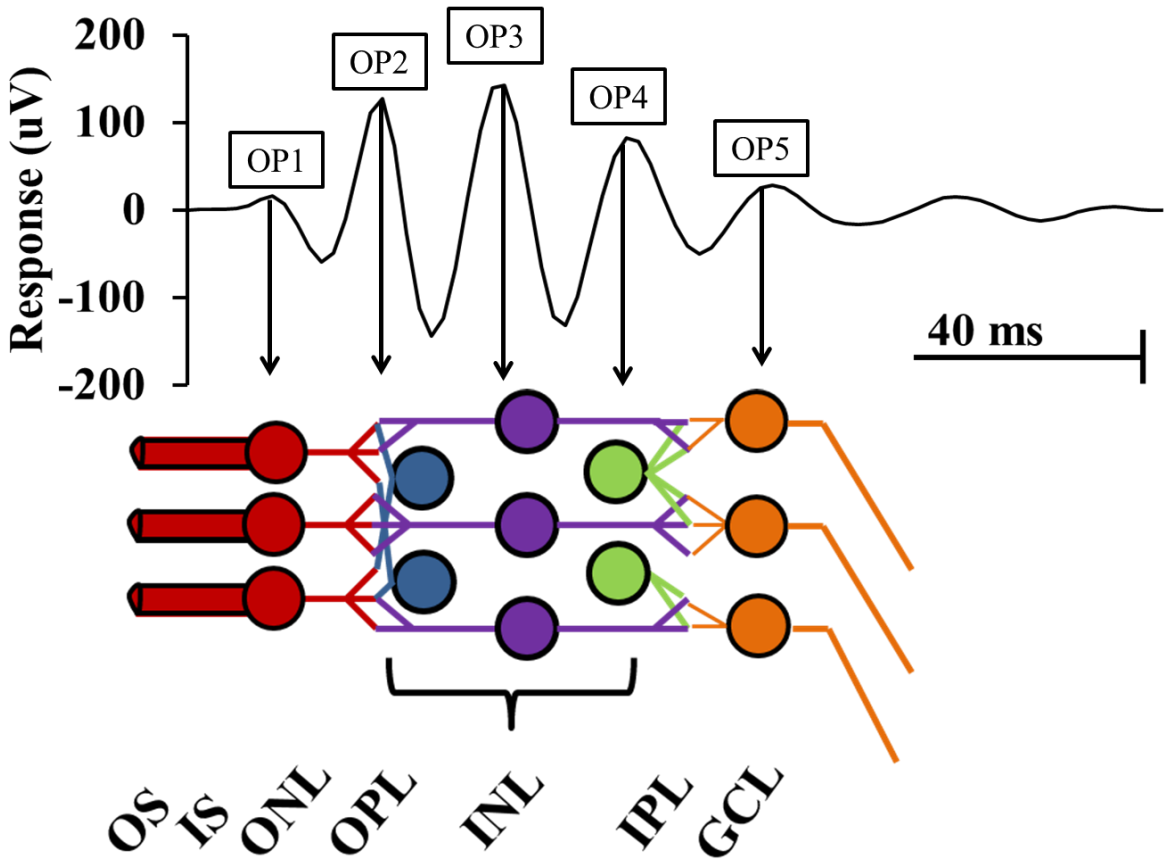


**Figure 4.1. Isolated oscillatory potentials (OP1-OP5) may correspond to retinal layer functionality.** OP1 is associated with photoreceptor hyperpolarization (red). Intermediate peaks OP2-OP3 are believed to be the response of second-order horizontal (blue) and bipolar (purple) action-potential independent (graded) neurons. Subsequent late OP peaks are believed to be associated with action-potential dependent amacrine (green) and ganglion (orange) cells. Intermediate OP peaks are thereby generally associated with INL function and later OP peaks with GCL function. Radial electrochemical cycling is the result of feedback mechanism occurring across the IPL of the retina.

which are involved in maintenance of neurite function and synaptic health.[103] In addition to neurite loss, the first histological hallmarks of retinal degeneration begin at three months of age, with retinal thinning of the ganglion and amacrine cells.[93] Oscillatory potentials measure retinal health and signal transduction through the retina and can therefore assess the health of both the neurites and the ganglion cells prior to structural losses. OPs are capable of detecting early changes as a result of mitochondrial dysfunction prior to any functional losses in the *hq* retina as diagnosed by the ERG a-wave and b-wave.

### *4.3 The hqY mouse shows early neuronal functional deficits*

In the longitudinal study of ERG OPs through the *hq* disease, OP profiles changed in both the time and frequency domain. The initial latency of OPs indicated that functional changes began as early as three months of age in *hq* mice. Simultaneously, changes in the major frequency of the OPs began at two months of age in the *hq* mouse and were followed by a steep reduction in OP frequency occurring between two and three months of age. Major frequency and initial latency are informative of periodicity and likely a response of radial current cycling through the inner retina and therefore are indicative of the speed of the graded potential changes in the INL and GCL as a result of photoreceptor synapsis leading to depolarization of the bipolar cells. Analysis in the frequency domain is advantageous when examining periodicity of OPs because it identifies significant changes across *hq* retina function prior to the time domain.

Significant decreases in OP summed amplitude began at four months of age in the *hq* mouse and continued into later ages with diminished total OP amplitude. Analogous changes in the frequency domain demonstrate decreases in total OP energy occurring at four months of age. Both the summed amplitude and total energy are indicative of total energetic response of the OPs, and therefore the functionality and health of all cells in the inner retina. Decreases of both *hq* OP summed amplitude and total energy are likely due to neuronal cell loss of the ONL, INL and GCL as decreasing OP amplitudes have been implicated in structural retinal loss.[56] Summed OP amplitude can therefore be used as a measure of overall inner retinal health as previously described in other models.[66,78,79]

In the *hq* mouse, inner retinal functional deficits as a result of changes in OP frequency and latency occur prior to any documented structural losses at four months.[19,93,102] These functional differences occur as early as two months of age and are consistent with a neuronal synaptic malfunction and microglial activation at complementing ages in the *hq* retina. The activation of microglial cells and OP functional deficits of the inner retina coincide at two months and indicate the loss of homeostasis and neuronal synaptic malfunction.

### *4.4 The hqX mouse demonstrates slower disease progression of the inner retina*

The *hq* carrier mouse phenotype displays a moderate, extended disease phenotype in comparison to the hemizygous or homozygous disease mice.[93,102,103] The functionality of the inner retina, as measured by OPs of the ERG, demonstrate consistent moderate phenotypic results. In fact, no OP initial latency or frequency changes were observed in

the *hq* carrier mice at any age. This is indicative of no periodicity change in the retina of the *hq* carrier mice and sufficient responses of the synapsis between ONL: INL and INL:GCL neurons and overall vitality of the ONL photoreceptors. However, decreases in both amplitude and analogous energy and power indicate inner retinal cell losses and decreases in INL and GCL function at eleven months of age. Retinal thinning in the *hq* carrier retina is not evident until approximately fifteen months when structural losses of the INL and ONL occur.[103] Therefore OPs identify physiological changes of the INL (bipolar and amacrine cells) prior to any structural cell loss and reveal a diagnostic parameter to assess retinal health before cell death has occurred.

### *4.5 hqY OP functional losses mimic retinopathy and may help reveal the origin of OPs*

Mammalian retinopathy begins with photoreceptor loss in the ONL. Retinopathy leads to hyperoxia in the inner retina caused by oxidative challenges, neovascularization, and inflammation.[143,144] Recent studies, of both human and rat scotopic ERGs have demonstrated the functional disease progression of retinopathy and its effect on OPs. Retinopathy leads to decreases in all OP amplitudes, particularly that of early OPs, indicative of persistent dysfunction of photoreceptors.[66,78] Deterioration of OP amplitudes and total OP energy in *hq* disease mice indicates similar disease mechanisms to that of retinopathy as health of photoreceptors is diminished.

Aging has been associated with nuclear losses in the INL and GCL leading to compromised retinal function with senescence.[66,145,146] Aging leads to the progressive

loss in OP periodicity (initial latency and frequency) in wild-type rats and humans,[66,146] analogous to periodicity changes in the *hq* retina. The deficits in *hq* OPs demonstrate persistent effects of hypomorphic AIF on retinal function leading to mitochondrial dysfunction, photoreceptor cell death, retinal degeneration and an advanced aging phenotype. A thorough histological characterization of *hq* retina neuron losses indicates OP are generated in the INL and GCL and are helpful in the investigation of the source of OP production in the retina.[102,132]

### *4.6 Non-metric multidimensional scaling offers a comprehensive visualization of inner retinal function with genotype and age*

The measurement of each OP amplitude and latency in the time domain provided a total of eight measurements for each flash intensity (excluding OP1 due to inconsistencies and photoreceptor contamination). Four flash intensities (0.63, 4, 10 and 25 cd •s/$m^2$) were examined as they all contained strong and measureable OP responses. Across the four flash intensities 32 measurements were taken in the time domain and 12 measurements in the frequency domain for each mouse.

NMDS computationally-derived coordinates fitted to 32 time-domain variables into two dimensions and 12 frequency-domain variables into two dimensions. The stress associated with modelling multiple parameters into two dimensions was low across all four analyses and demonstrates a valid, comprehensive evaluation of OPs across multiple stimulus intensities. NMDS analysis provided a valuable interpretable aid in examining disease progression and provides translational relevance in determining origins of disease

and potentially identifying drug targets. Pearson's correlation coefficients were used to examine the correlation of each axis with each of the fitted variables to determine which variables participate most into axis determination. For example, flash eight OP2 amplitude may be highly positively correlated with the x-axis and therefore any sample with high flash eight OP2 amplitude will receive a high ordination on the x-axis. NMDS of OP parameters both in the time domain and frequency domain provided a visual aid in examination of disease progress as well as an interpretation of OP parameters and their impact on disease.

### *4.7 NMDS of hqY mice reveals distinct functional retinal changes by two months of age*

NMDS of time-domain OP parameters reveals that young, *hq*Y mice (two months of age) cluster distinctly from wild-type mice and demonstrate early characteristics of retinal dysfunction. Through axis interpretation with Pearson's correlation coefficients it is evident that young, *hq*Y mice (two months of age) cluster in regions of low, early OP amplitudes (OP2-OP3) as well as decreasing initial latencies across all flash intensities. Age-matched wild-type mice cluster in regions of high, late OP amplitudes (OP4-OP5) at all flash intensities as well as short initial latencies across all flash intensities. It is therefore apparent that mechanisms of the *hq* disease lead to early OP latency increases and amplitude loss followed by both latency increases and amplitude reductions across all OPs later in life. This is consistent with previous findings indicating that *hq* mice experience ONL losses at four months of age.[19,93] However, this evidence suggests that functional changes may occur as early as two months in the *hq* photoreceptors and INL

cells. An interesting observation is that ten-month-old wild-type mice cluster similarly to that of two-month-old *hq* mice indicating that young *hq* mice show retinal functional losses similar to that of middle-age wild-type mice. Ageing has been shown to affect rod photoreceptor function leading to a 40% reduction in mouse rods.[147] This suggests that *hq* mice exhibit ERG features similar to an advanced aging phenotype leading to photoreceptor losses and decreased INL and GCL function.

In the frequency domain, young two-month-old *hq*Y mice cluster distinctly with reductions in power and frequency in comparison to wild-type mice across all flash intensities. Wild-type mice cluster in regions of high energy, power and frequency across all ages with minimal OP changes with age. Aging of the *hq* mouse demonstrates dramatic reductions in OP frequency, power and energy, particularly between two and three months of age. This is indicative of reduced radial current feedback in the *hq* retina due to reductions in periodicity and overall INL and GCL function resulting in reduced neural retina response and OP generation.

### *4.8 NMDS of hqX mice reveals distinct retinal changes at eleven months of age*

NMDS of time-domain parameters indicates that middle-aged (eleven months of age) *hq*X mice cluster distinctly with reductions in both early and later OP amplitudes (OP2-OP5) as well as shorter overall latencies. Age-matched wild-type mice indicate slight reductions in all OP amplitudes but shortened overall latencies across all flash intensities. These functional decreases would indicate that the *hq*X mice lose the functionality of the overall retinal response and likely experience neurite losses in both

the OPL and IPL. Cell loss and subsequent retinal thinning does not occur in the INL and GCL until fifteen months of age in the *hq*X mice,[103] however functional changes are evident early through NMDS of time-domain OPs.

In the frequency domain, middle-aged *hq*X mice (eleven months of age) cluster distinctly with large overall reductions in OP power and energy across all flash intensities and increases in OP frequency with age. Wild-type mice of similar ages cluster in regions of sustained OP power and energy with increased frequency. Functional losses in total OP energy and power indicate a delayed and stunted response of the radial current feedback of the INL and GCL. This is prior to any structural losses and indicates an early functional diagnosis of the *hq*X retinal disease.

### *4.9 The hq mouse retina maintains an intact inner and outer blood-retinal barrier*

Assessments of the blood-retinal barrier via Evans Blue circulation indicate no increase in EB concentrations in the retina of *hq* mice when compared to age-matched wild-type mice. Although endothelial cells of the inner and epithelial cells of the outer retina (RPE) blood barrier are highly metabolic, they retain functional tight junctions with limited diffusion of exogenous EB from the vasculature into the sensitive inner retinal space. This is consistent with the alternate hypothesis of activation of *hq* retinal microglial cells from an endogenous source due to diminished AIF function leading to cell stress and loss of retinal neurons. Although retinal endothelial and epithelial vasculature are rich in mitochondria and highly metabolic, a probable explanation of integrity is due to maintenance by glia.[148] Glial cells rely heavily on glycolytic ATP as

well as lactate and therefore a deficiency in OXPHOS will not compromise glial function.[119] Glial cells have been shown to enhance blood-retinal barrier properties by increasing tight junction protein expression, endothelial-1,[149] as well as providing neuronal support[150] for both the outer[151] and inner[33] retina. It would be expected that a reduction in complex I functionality and ATP production accompanying *hq* mice leads to a blood-retinal barrier malfunction but continued support from aerobic glial cells promotes the continued formation of tight junctions and maintenance of the blood-retinal barrier.

### *4.10 Transcriptome changes demonstrate Aif downregulation*

Gene expression analysis of *hq Aif* is consistent with previous findings suggesting a global downregulation of *Aif* mRNA transcript by over 80%.[93] Contrary to previous findings downregulation of *Aif* in the retina surpasses an 80% reduction in the retina of four-, three-, and two-month-old mice to a downregulation by 91.16%, 94.22% and 91.88% respectively. This finding is consistent with quantified protein expression in the *hq* retina indicating minimal to nil endogenous AIF expression and complex I efficiency in the *hq* retina.[95,98] Regulation of *hq Aif* gene expression occurs prior to transcription and specifies that the regulatory region of intron 1 is more vital in the retina than other tissues. The significant downregulation of *Aif* in the *hq* retina may explain the rapid onset of retinal degeneration preceding other tissue malfunctions. Functional retinal deficits begin at two months of age and an early reduction of *Aif* mRNA expression may be the catalyst to early retinal degeneration in the *hq* mouse.

### *4.11 The hq retinal transcriptome suggests alternative metabolism*

As functional losses occur in the ONL of the *hq* retina, it is important to characterize endogenous activation of microglial cells and changes that lead to cell loss. The loss of *Aif* efficacy leads to reduced complex I function and expression resulting in reduced ATP yield across a variety of tissues.[95,98,118] As predicted, the *hq* retina at two-, three- and four-months of age are unable to upregulate early, key enzymatic reactions of the glycolytic cycle as demonstrated by *Hexokinase I* (*Hk1*). *Hk1* catalyzes the first regulatory, enzymatic reaction of glycolysis in the cytoplasm by phosphorylating glucose to glucose 6-phosphate (Figure 4.2A).[152] Overexpression of *Hk1* drives high rates of aerobic glycolysis, largely in cancers.[153] *Hk1* demonstrated no change in transcript levels in the *hq* retina even after microarray data suggested it may be upregulated.

Previous studies suggest the role of increased glucose uptake in *hq* mesodermal/endodermal tissues as a result of OXPHOS deficiency and a reliance on glycolytic ATP.[98,118] Glycolytic flux is believed to be primarily controlled at the level of glucose uptake and phosphorylation of glucose by *Hk1*.[154] In agreement with no glycolytic changes in the *hq* retina, the expression of *Glucose transporter 4* (*Glut4*), a glucose transporter in the retina,[155] demonstrates no significant changes in mRNA expression. *Glut4* is a rapid, time-scale glucose transporter that translocates to the plasma membrane from the endoplasmic reticulum when insulin binds its receptors on the cell surface (Figure 4.2A).[156] This translocation is mediated by *TBC1 Domain Family, Member 4* (*TBC1D4*)[157] which also showed no regulation changes in the *hq* retina at any age. The regulation of *Glut* and *Hk1* exhibit the high control over glycolytic flux[154] and

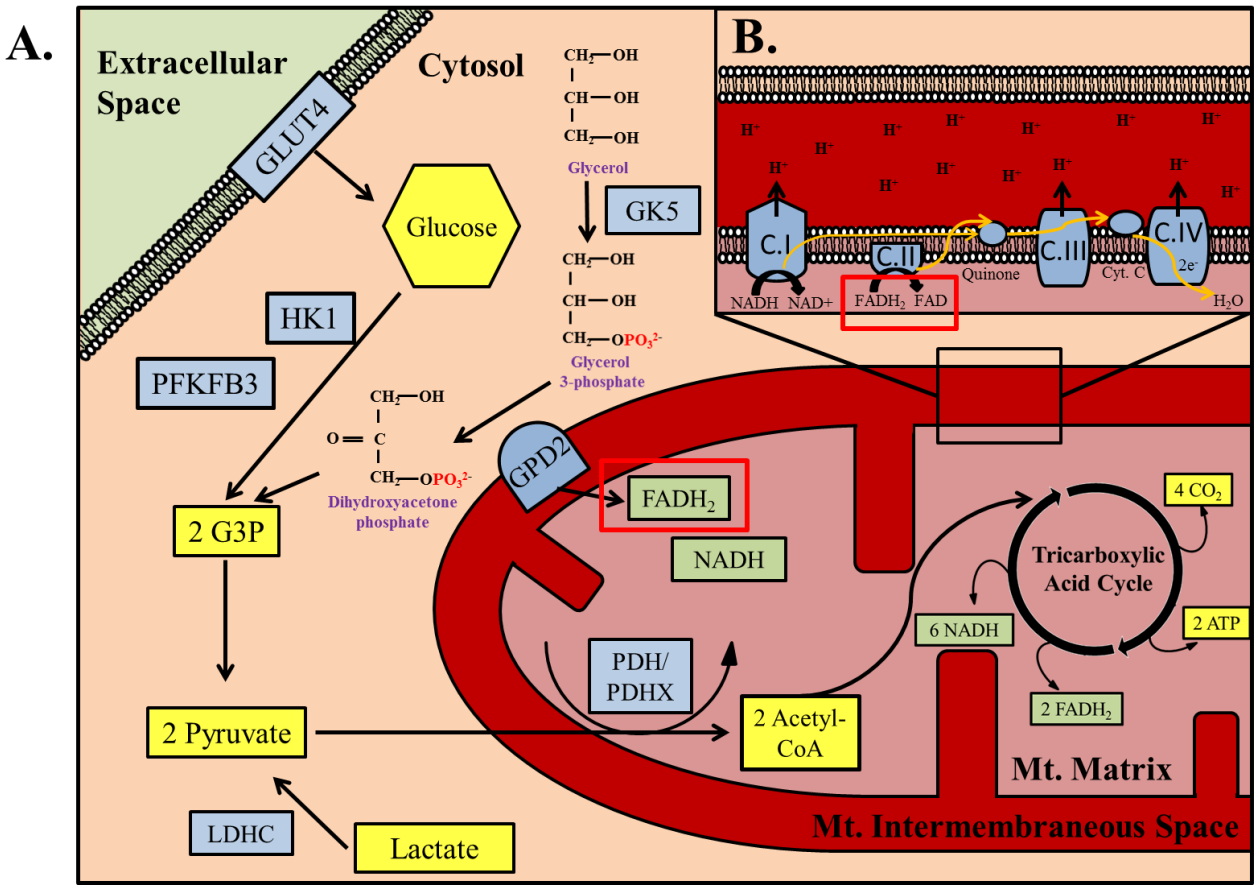
A.
Extracellular Space
Cytosol
GLUT4
Glucose
HK1
PFKFB3
2 G3P
2 Pyruvate
LDHC
Lactate
Glycerol
GK5
Glycerol 3-phosphate
Dihydroxyacetone phosphate
GPD2
FADH2
NADH
PDH/ PDHX
2 Acetyl-CoA
Tricarboxylic Acid Cycle
4 CO2
2 ATP
6 NADH
2 FADH2
Mt. Matrix
Mt. Intermembraneous Space
B.
C.I
C.II
C.III
C.IV
Quinone
Cyt. C
2e-
NADH NAD+
FADH2 FAD
H2O

**Figure 4.2. Proposed mechanisms of altered metabolism in the hq mouse based on significant alterations in the *hq* retinal transcriptome.** Boxes coloured: blue indicate enzymes, yellow indicate substrates/metabolites and green indicate reducing equivalents. (A) Glucose metabolism in the hq retina, beginning with the uptake of glucose from the extracellular space by GLUT4 and followed by regulatory steps of glycolysis (HK1, PFKFP3) remain essentially unchanged. Metabolism of glycerol in the *hq* retina is differentially upregulated beginning with the conversion of glycerol to glycerol 3-phosphate by GK5. Mitochondrial bound GPD2 facilitates the conversion of glycerol 3-phosphate to dihydroxyacetone phosphate by reducing FAD to FADH2. The glycerol shuttle shuttles FADH2 into the mitochondria. In addition, the formation of dihydroxyacetone phosphate from glycerol metabolism feeds into glycolysis and through the formation of glyceraldehyde 3-phosphate (G3P). The dysfunction of complex I in the hq retina causes an accumulation of NADH and decreased ATP production. (B) FADH2, produced by the glycerol shuttle, can donate electrons distal to complex I and allow improved functionality of OXPHOS in the *hq* retina.

show no differential expression in the *hq* retina (Figure 4.2A). These observations support no upregulation of transcript levels of glycolytic compensatory mechanisms for neuronal ATP deficits cause by AIF dysfunction. This further confirms that neurons may be unable to upregulate glycolysis as increased glycolytic rate leads to oxidative stress and apoptotic cell death.[45]

Neuronal and glial cells do not preferentially metabolize triglyceride components under healthy conditions.[158] β-oxidation of fatty acids is not favoured in neurons because; 1) it requires high levels of oxygen thereby increasing risk of becoming hypoxic 2) it leads to generation of superoxides and 3) has a slower ATP turnover *in vivo*.[158] Glycerol however, can traverse the blood-brain-barrier[159] and be utilized as a neuronal metabolite.[160] A suspected similar mechanism may occur in the retina during periods of ATP depletion and metabolic need. Glycerol metabolism is highly energetic as it fuels ATP formation as well the ability to participate in the glycerol-3-phosphate (G3P) shuttle by transferring reducing agents into the mitochondrion and leading to the formation of $FADH_2$ (Figure 4.2AB).[160] The oxidative metabolism of glycerol leads to the formation of one $FADH_2$ reducing molecule before forming 3-carbon, dihydroxyacetone phosphate which can enter the glycolytic pathway (Figure 4.2A). *Glycerol-3-phosphate dehydrogenase* (*Gpd2*) and *Glycerol kinase 5* (*Gk5*) encode the primary and

secondary enzymatic mediators leading to and facilitating glycerol metabolism in the brain (Figure 4.2A).[160] Both *Gpd2* and *Gk5* transcript levels were upregulated in the *hq* retina at four months of age inferring neuronal metabolism of glycerol as a metabolic means for ATP and $FADH_2$ production. GK5 facilitates the primary step of glycerol metabolism by phosphorylating glycerol to L-glycerol 3-phosphate and was upregulated

at two-months of age and suggests a potential link between early *hq* disease and glycerol metabolism.

Since OXPHOS of the *hq* mouse becomes dysfunctional, alternative mechanisms for generation of ATP must occur in order for neurons of the retina to remain viable. Excess glycerol fed into the later stages of glycolysis would lead to a bottleneck of pyruvate oxidation (pyruvate dehydrogenase) and as expected the *Pyruvate dehydrogenase complex component X* (*Pdhx*) of pyruvate dehydrogenase is upregulated at four months. *Pdhx* is a structural component of the pyruvate dehydrogenase complex that links the catalytic and regulatory subunits of the functional complex.[161] Pyruvate dehydrogenase complex is the metabolic link between glycolysis and the Tricarboxylic (TCA) acid cycle by decarboxylating pyruvate to form acetyl-CoA (Figure 4.2A). Deficiencies in *Pdhx* cause pyruvate dehydrogenase malfunction and have been associated with neurological dysfunction and lactate acidosis.[161] Although the directionality of *Pdhx* expression based on Taqman® assay and microarray for *Pdhx* do not agree, dysregulation infers an intracellular mechanism that may lead to lactate acidosis in the *hq* retina and/or enhanced production of acetyl-CoA as a result of increased glycerol metabolism. *In vivo* examination of PDHX activity may help resolve its exact function in the *hq* retina.

OXPHOS complex I reduction in the *hq* mouse[98] likely results in the inadequate processing and utilization of reducing agents (NADH and $FADH_2$) produced by the mitochondrial TCA Cycle (Tricarboxylic Acid Cycle) (Figure 4.2). This is of particular importance for NADH, which is primarily oxidized by the NADH dehydrogenase complex (complex I) of the electron transport chain. A dysfunction of NADH

dehydrogenase may disrupt the NAD+ pool, increasing the NADH/NAD+ ratio thereby altering the redox state of the cell.[162] In 80% of patients with complex I deficiency, high levels of lactate/pyruvate were evident with severe increases in NADH/NAD+ ratios.[163] Since it is likely that *hq* OXPHOS has compromised utilization of NADH, the mitochondria may compensate by decreasing the throughput of the TCA Cycle (high NADH concentrations decrease the activity of malate dehydrogenase, the primary step of the TCA cycle[164]) and increase glycerol metabolism as a means to increase $FADH_2$ production. $FADH_2$ electrons enter the electron transport chain distal to complex I and therefore can be used as an alternative electron source for driving the electron transport chain in order to maintain its function.[165]

Severe increases in NADH/NAD+ are also associated with ketoacidosis and lactate acidosis as a result of acetyl-CoA being converted into acetoacetic acid and beta-hydroxybutyric acid or lactate.[166,167] Neuronal excitability is affected by intracellular acid-base homeostasis,[168] where a rise in pH is associated with increased neuronal excitability, and a drop in pH reducing neuronal excitability.[169,170] Acidic buffering to maintain pH, decreases intracellular concentration of $HCO_3^-$ and further reduces buffering capabilities of the cell.[171] Consequently, two key intracellular pH regulators and bicarbonate transporters are transcriptionally upregulated in the *hq* retina at four-months. *Solute carrier family 4, sodium bicarbonate transporter, member 10* (*Slc4a10*) is a sodium-coupled bicarbonate transporter that exploits the transmembrane $Na^+$ gradient in neurons to uptake $HCO_3^-$ and reduces acid load.[172] *Adenylate cyclase 10* (*Adcy10*) is believed to be a universal, evolutionarily conserved bicarbonate sensor.[173] Unlike other intracellular pH regulators, *Adcy10* functions as a bicarbonate sensor rather than a proton

sensor which allows a more direct regulation of bicarbonate to maintain pH homeostasis.[174] Almost every cellular protein is sensitive to fluctuations in pH, however ADCY10 exhibits a unique ability to remain functional during extreme pH fluctuations.[173] In addition, ADCY10 exhibits the ability to regulate the TCA cycle. Discrepancy between generation and utilization of reducing agents (NADH and $FADH_2$) produced mainly by the TCA cycle, leads to ROS production and becomes harmful for the cell.[174] *Adcy10* uses $CO_2$ produced by the TCA cycle to serve as a metabolic signal for TCA cycle turnover and can reduce the intra-mitochondrial cAMP concentration leading to reduced output of the TCA cycle.[174] *Adcy10* is upregulated in both the four-month *hq* retina and the four-month *hq* cerebellum inferring an increased cellular need for pH homeostasis and TCA cycle regulation. High NADH/NAD+ ratios will also push increased lactate production which has been observed in *Aif*-deficient cells and tissues of the *hq* mouse.[95,98,118] Expression analysis of *Lactate dehydrogenase C* (*Ldhc*), which catalyzes the reverse reaction of lactate to pyruvate, was not examined due to low transcript levels of the gene (Figure 4.2A

Previous transcriptome studies of the *hq*-mouse retina performed by our laboratory are consistent with ammonia toxicity and protein degradation leading to amino acid metabolism as a source for ATP generation *in vivo*.[175] The catabolism of amino acids is associated with the production of aldehyde by-products which can lead to glycation of amino-acids,[176,177] and subsequent inflammatory responses. Thereby, *Aldehyde dehydrogenase 2* (*Aldh2*) is likely transcriptionally upregulated in the *hq* retina to eliminate toxic aldehydes as a consequence of increased amino acid catabolism.[178]

### *4.12 The limitations of transcriptome analyses and future in vivo examinations*

The transcriptome of the *hq* retina identifies many useful preliminary therapeutic targets and potential early disease mechanisms, however many limitations exist with transcriptome investigation. Transcriptional analysis occurs prior to post-transcriptional processing, translation and post-translational regulation and therefore does not reflect the quantity or functionality of the enzyme/protein *in vivo*. In addition, other interacting targets may be responsible for the phenotype observed. Further examinations at the level of the proteome are important for characterizing changes and complete interactions as a result of the *Aif* downregulation *in vivo.* One recommendation is the examination of key enzymatic factors of the glycerol pathway, GK5 and GPD2, to determine if increased neuronal glycerol metabolism is a feasible mechanism for $FADH_2$ production. In addition to proteome analysis, gas-chromatography mass spectrophotometry could be used to determine the *in vivo* concentrations of metabolites such as NADH, NAD+, lactate, pyruvate, dihydroxyacetone phosphate, and $FADH_2$ in comparison to the wild type. This will give us better insight into the mechanisms that occur in the *hq* retina to cope with NADH dehydrogenase dysfunction and reduced ATP production.

### *4.13 Preliminary suggestions for hq mitochondrial dysfunction therapy*

In addition to transcriptome quantification, a preliminary study of metabolic rate suggests that *hq* mice are hyperphagic and require increased food consumption. This is likely the result of reduced OXPHOS function causing a reduced ratio of ATP produced per molecule of glucose. *hq* mice are resistant to progressive weight gain and lipid

accumulation when fed a high fat diet inferring potential reliance and utilization of triglycerides as predicted.[118] This is likely due to the fact that fatty acids and glycerol yield a much higher $FADH_2$ and NADH than glucose and are commonly used for treatment of complex I deficiencies.[162]

From a therapeutic point of view, treatment of *hq* mice must take a direct approach to correcting mitochondrial dysfunction. Increased glycerol metabolism in the *hq* mouse predicts an increased reliance on $FADH_2$ as the primary reducing agent in the mitochondria. The benefits' of a high fat diet are likely to reduce the severity of the *hq* phenotype, although the benefits are unlikely to provide continued treatment due to NADH accumulation in the cell. Thereby, a probable treatment may be in the form of Riboflavin (vitamin $B_2$). Riboflavin is a flavoprotein precursor and is the central component of FAD. Treatment with riboflavin will allow the cell to produce more $FADH_2$ and facilitate the enzymatic reactions of the TCA cycle.[179] Complex I and II deficiencies show betterment of symptoms and delayed disease progression following treatment with riboflavin.[180–182] In addition, riboflavin has been used to treat human patients with OXPHOS deficiency caused by an *Aif* amino-acid deletion (*R201 del*).[183] Riboflavin treatment improves neurological symptoms and increases the functionality of OXPHOS in these patients.[183] Although the *hq* disease is associated with a severe downregulation of *Aif* as opposed to a deletion of an amino acid, riboflavin supplementation demonstrates a promising preliminary therapeutic treatment for improving the *hq* disease.

### *4.14 Conclusions*

Retinal degeneration in the *hq* mouse is characterized by mitochondrial dysfunction leading to parainflammation and closely mimics aging and mitochondrial-associated retinal degeneration. Early disease mechanisms resulting in degeneration of the *hq* retina are associated with early neurite losses and photoreceptor cell losses that can be characterized by diagnostic oscillatory potentials. This study has developed a novel framework for the analysis of the entire OP profile across multiple stimuli, allowing functional examination of all retinal cell types and their health when combined with a-wave and b-wave analyse. We have identified diagnostic ERG markers associated with the *hq* disease as well as a pipeline for identifying diagnostic ERG markers in other models of retinal disease. Parainflammation in the *hq* retina is more likely the result of endogenous retinal AIF deficiency and transcriptome alterations are consistent with compensatory mechanisms of ATP production such as glycerol metabolism. Studies aimed at a thorough characterization of glycerol metabolism as well as the accumulation of specific primary metabolites will help elucidate the role of AIF and bring us closer to understanding mitochondrial-associated retinal degeneration.

## Chapter 5. Bibliography


1. Kondo, K. Rising prevalence of neurodegenerative diseases worldwide. *Intern. Med.* **35,** 238 (1996).

2. Mayeux, R. Epidemiology of neurodegeneration. *Annu. Rev. Neurosci.* **26,** 81–104 (2003).

3. George, M., Norris, M., Nault, F., Loh, S. & Dai, S. *Population Projections for Canada, Provinces and Territories 2009-2036.* 1–248 (2009). at <http://www.popline.org/node/290587>

4. CNIB Report. *The Cost of Vision Loss in Canada*. 1–26 (2009). at <http://www.cnib.ca/eng/CNIB Document Library/Research/Summaryreport_Covl.pdf>

5. Jager, R. D., Mieler, W. F. & Miller, J. W. Age-related macular degeneration. *N. Engl. J. Med.* **358,** 2606–17 (2008).

6. Wang, L. *et al.* Abundant lipid and protein components of drusen. *PLoS One* **5,** e10329 (2010).

7. Kolb, H. How the retina works. *Am. Sci.* **91,** 27–35 (2003).

8. Antonetti, D. A., Klein, R. & Gardner, T. W. Diabetic retinopathy. *N. Engl. J. Med.* **366,** 1227–39 (2012).

9. Kwon, Y. H., Fingert, J. H., Kuehn, M. H. & Alward, W. L. M. Primary open-angle glaucoma. *N. Engl. J. Med.* **360,** 1113–24 (2009).

10. Alward, W. L. M. Medical management of glaucoma. *N. Engl. J. Med.* **339,** 1298–1307 (1998).

11. Smith, R., Joh, S., Nishina, P. & Sandberg, J. *Systematic Evaluation of the Mouse Eye: Anatomy, Pathology, and Biomethods*. **20012478,** 1–384 (CRC Press, 2001).

12. Dowling, J. E. Organization of vertebrate retinas. *Invest. Ophthalmol.* **9,** 655–80 (1970).

13. Thompson, D. A. & Gal, A. Vitamin A metabolism in the retinal pigment epithelium: genes, mutations, and diseases. *Prog. Retin. Eye Res.* **22,** 683–703 (2003).

14. Baylor, D. How photons start vision. *Proc. Natl. Acad. Sci. U. S. A.* **93,** 560–5 (1996).

15. Strauss, O. The retinal pigment epithelium in visual function. *Physiol. Rev.* **85,** 845–881 (2005).

16. Kolb, H. Photoreceptors. *Webvision Organ. Retin. Vis. Syst.* (2014). at <http://webvision.med.utah.edu/book/part-ii-anatomy-and-physiology-of-the-retina/photoreceptors/>

17. Müller, B. & Peichl, L. Horizontal cells in the cone-dominated tree shrew retina: morphology, photoreceptor contacts, and topographical distribution. *J. Neurosci. Off. J. Soc. Neurosci.* **13,** 3628–46 (1993).

18. Masland, R. H. The neuronal organization of the retina. *Neuron* **76,** 266–80 (2012).

19. MacPherson, T. C. Ocular phenotyping in the harlequin mouse model of retinal degeneration: a framework for therapeutic testing. 1–265 (2009).

20. Arshavsky, V. Y., Lamb, T. D. & Pugh, E. N. G proteins and phototransduction. *Annu. Rev. Physiol.* **64,** 153–87 (2002).

21. Koutalos, Y. & Ebrey, T. Recent progress in vertebrate photoreception. *Photochem. Photobiol.* **44,** 809–817 (1986).

22. Fu, Y. Phototransduction in rods and cones. *Webvision Organ. Retin. Vis. Syst.* (2014). at <http://webvision.med.utah.edu/book/part-v-phototransduction-in-rods-and-cones/phototransduction-in-rods-and-cones/>

23. Wang, T. & Montell, C. Phototransduction and retinal degeneration in Drosophila. *Pflügers Arch. Eur. J. Physiol.* **454,** 821–47 (2007).

24. Wu, J., Seregard, S. & Algvere, P. V. Photochemical damage of the retina. *Surv. Ophthalmol.* **51,** 461–81 (2006).

25. Kolb, H. Glial cells of the retina. *Webvision Organ. Retin. Vis. Syst.* (2014). at <http://webvision.med.utah.edu/book/part-ii-anatomy-and-physiology-of-the-retina/glial-cells-of-the-retina/>

26. Tsacopoulos, M. & Magistretti, P. Metabolic coupling glia and neurons. *J. Neurosci.* **76,** 877–885 (1996).

27. Matsui, K., Hosoi, N. & Tachibana, M. Active role of glutamate uptake in the synaptic transmission from retinal nonspiking neurons. *J. Neurosci.* **19,** 6755–66 (1999).

28. Long, K. O., Fisher, S. K., Fariss, R. N. & Anderson, D. H. Disc shedding and autophagy in the cone-dominant ground squirrel retina. *Exp. Eye Res.* **43,** 193–205 (1986).

29. Tout, S., Chan-ling, T., Hollander, H. & Stone, J. The role of Muller cells in the formation of the blood-retina barrier. *Neuroscience* **55,** 291–301 (1993).

30. Reichenbach, A., Henke, A., Eberhardt, W., Reichelt, W. & Dettmer, D. K+ ion regulation in the retina. *Can. J. Physiol. Pharmacol.* **70,** 239–47 (1992).

31. Biissow, H. The astrocytes in the retina and optic nerve head of mammals: a special glia for the ganglion cell axons. *Cell Tissue Res.* **206,** 367–378 (1980).

32. Stone, J. & Dreher, Z. Relationship between astrocytes, ganglion cells and vasculature of the retina. *J. Comp. Neurol.* **255,** 35–49 (1987).

33. Gardner, T. W. *et al.* Astrocytes increase barrier properties and ZO-1 expression in retinal vascular endothelial cells. *Invest. Ophthalmol. Vis. Sci.* **38,** 2423–7 (1997).

34. Tao-Cheng, J. H., Nagy, Z. & Brightman, M. W. Tight junctions of brain endothelium in vitro are enhanced by astroglia. *J. Neurosci.* **7,** 3293–3299 (1987).

35. Hanisch, U. Microglia as a source and target of cytokines. *Glia* **40,** 140–55 (2002).

36. Streit, W. J. Microglia as neuroprotective, immunocompetent cells of the CNS. *Glia* **40,** 133–9 (2002).

37. Graeber, M. B. & Streit, W. J. Microglia: biology and pathology. *Acta Neuropathol.* **119,** 89–105 (2010).

38. Kono, H. & Rock, K. L. How dying cells alert the immune system to danger. *Nat. Rev. Immunol.* **8,** 279–289 (2008).

39. Stahl, W. L. The Na, K-ATPase of nervous tissue. *Neurochem. Int.* **8,** 449–476 (1986).

40. Wong-Riley, M. Energy metabolism of the visual system. *Eye Brain* **2,** 99–116 (2010).

41. Vilchez, D. *et al.* Mechanism suppressing glycogen synthesis in neurons and its demise in progressive myoclonus epilepsy. *Nat. Neurosci.* **10,** 1407–13 (2007).

42. Brown, A. M. Brain glycogen re-awakened. *J. Neurochem.* **89,** 537–52 (2004).

43. Rapoport, S. I. Functional brain imaging in the resting state and during activation in Alzheimer's disease. *Ann. N. Y. Acad. Sci.* **893,** 138–153 (2006).

44. Bélanger, M., Allaman, I. & Magistretti, P. J. Brain energy metabolism: focus on astrocyte-neuron metabolic cooperation. *Cell Metab.* **14,** 724–38 (2011).

45. Herrero-Mendez, A. *et al.* The bioenergetic and antioxidant status of neurons is controlled by continuous degradation of a key glycolytic enzyme by APC/C-Cdh1. *Nat. Cell Biol.* **11,** 747–52 (2009).

46. Runkle, E. A. & Antonetti, D. A. in *Blood-Brain Other Neural Barriers Rev. Protoc. Methods Mol. Biol.* **686,** 133–148 (2011).

47. Hori, S., Ohtsuki, S., Hosoya, K., Nakashima, E. & Terasaki, T. A pericyte-derived angiopoietin-1 multimeric complex induces occludin gene expression in brain capillary endothelial cells through Tie-2 activation in vitro. *J. Neurochem.* **89,** 503–13 (2004).

48. Kniesel, U. & Wolburg, H. Tight junction complexity in the retinal pigment epithelium of the chicken during development. *Neurosci. Lett.* **149,** 71–4 (1993).

49. Austin, B. A., Liu, B., Li, Z. & Nussenblatt, R. B. Biologically active fibronectin fragments stimulate release of MCP-1 and catabolic cytokines from murine retinal pigment epithelium. *Invest. Ophthalmol. Vis. Sci.* **50,** 2896–2902 (2010).

50. Caldwell, R. B. *et al.* Vascular endothelial growth factor and diabetic retinopathy: pathophysiological mechanisms and treatment perspectives. *Diabetes. Metab. Res. Rev.* **19,** 442–55 (2003).

51. Cunha-Vaz, J., Faria de Abreu, J. R. & Campos, a J. Early breakdown of the blood-retinal barrier in diabetes. *Br. J. Ophthalmol.* **59,** 649–56 (1975).

52. Penn, R. & Hagins, W. Signal transmission along retinal rods and the origin of the electroretinographic a-wave. *Nature* **223,** 201–205 (1969).

53. Müller, R. & Dowling, J. Intracellular responses of the Müller (glial) cells of mudpuppy retina: their relation to b-wave of the electroretinogram. *J. Neurophysiol.* **33,** 323–41 (1970).

54. Wachtmeister, L. Oscillatory potentials in the retina: what do they reveal. *Prog. Retin. Eye Res.* **17,** 485–521 (1998).

55. Heynen, H., Wachtmeister, L. & Vvan Norren, D. Origin of the oscillatory potentials in the primate retina. *Vision Res.* **25,** 1365–1373 (1985).

56. Dong, C.-J., Agey, P. & Hare, W. A. Origins of the electroretinogram oscillatory potentials in the rabbit retina. *Vis. Neurosci.* **21,** 533–43 (2004).

57. Granit, R. Two types of retinae and their electrical responses to intermittent stimuli in light and dark adaptation. *J. Physiol.* **85,** 421–438 (1935).

58. Jeon, C. J., Strettoi, E. & Masland, R. H. The major cell populations of the mouse retina. *J. Neurosci.* **18,** 8936–46 (1998).

59. Cotlier, E., Weinreb, R., Tzekov, R. & Arden, G. B. The electroretinogram in diabetic retinopathy. *Surv. Ophthalmol.* **44,** 53–60 (1999).

60. Lachapelle, P., Benoit, J., Little, J. M. & Faubert, J. The diagnostic use of the second oscillatory potential in clinical electroretinography. *Doc. Ophthalmol.* **73,** 327–36 (1989).

61. Bui, B. V, Edmunds, B., Cioffi, G. A. & Fortune, B. The gradient of retinal functional changes during acute intraocular pressure elevation. *Invest. Ophthalmol. Vis. Sci.* **46,** 202–13 (2005).

62. Li, Q., Zemel, E., Miller, B. & Perlman, I. Early retinal damage in experimental diabetes: electroretinographical and morphological observations. *Exp. Eye Res.* **74,** 615–25 (2002).

63. Hancock, H. A. Oscillatory potential analysis and ERGs of normal and diabetic rats. *Invest. Ophthalmol. Vis. Sci.* **45,** 1002–1008 (2004).

64. Hara, A. & Miura, M. Decreased inner retinal activity in branch retinal vein occlusion. *Doc. Ophthalmol.* **88,** 39–47 (1994).

65. Yonemura, D., Aoki, T. & Tsuzuki, K. Electroretinogram in diabetic retinopathy. *Arch. Ophthalmol.* **68,** 19–24 (1962).

66. Akula, J. D., Mocko, J. A., Moskowitz, A., Hansen, R. M. & Fulton, A. B. The oscillatory potentials of the dark-adapted electroretinogram in retinopathy of prematurity. *Invest. Ophthalmol. Vis. Sci.* **48,** 5788–97 (2007).

67. Marmor, M. F. *et al.* ISCEV standard for full-field clinical electroretinography (2008 update). *Doc. Ophthalmol.* **118,** 69–77 (2009).

68. Meklenburg, J., Clancy, E. A. & Tzekov, R. Signal processing techniques for oscillatory potential extraction in the electroretinogram: automated highpass cutoff frequency estimation. *Doc. Ophthalmol.* **125,** 101–11 (2012).

69. Zhang, K., Yao, G., Gao, Y., Hofeldt, K. J. & Lei, B. Frequency spectrum and amplitude analysis of dark- and light-adapted oscillatory potentials in albino mouse, rat and rabbit. *Doc. Ophthalmol.* **115,** 85–93 (2007).

70. Lei, B., Yao, G., Zhang, K., Hofeldt, K. J. & Chang, B. Study of rod- and cone-driven oscillatory potentials in mice. *Invest. Ophthalmol. Vis. Sci.* **47,** 2732–8 (2006).

71. Hood, D. C. & Birch, D. G. Rod phototransduction in retinitis pigmentosa: estimation and interpretation of parameters derived from the rod a-wave. *Invest. Ophthalmol. Vis. Sci.* **35,** 2948–61 (1994).

72. Granit, R. The componenets of the retinal action potential in mammals and their relation to the discharge in the optic nerve. *J physiol* **77,** 207–239 (1933).

73. Lamb, T. D. & Pugh, E. N. A quantitative account of the activation steps involved in phototransduction in amphibian photoreceptors. *J. Physiol.* **449,** 719–758 (1992).

74. Hood, D. C. & Birch, D. G. Phototransduction in human cones measured using the alpha-wave of the ERG. *Vision Res.* **35,** 2801–10 (1995).

75. Bui, B. V., Armitage, J. A. & Vingrys, A. J. Extraction and modelling of oscillatory potentials. *Doc. Ophthalmol.* **104,** 17–36 (2002).

76. Li, X. X. & Yuan, N. Measurement of the oscillatory potentials of the electroretinogram in the domains of frequency and time. *Doc. Ophthalmol.* **76,** 65–71 (1990).

77. Moskowitz, A., Hansen, R. M. & Fulton, A. B. ERG oscillatory potentials in infants. *Doc. Ophthalmol.* **110,** 265–70 (2005).

78. Liu, K. *et al.* Development of the electroretinographic oscillatory potentials in normal and ROP rats. *Invest. Ophthalmol. Vis. Sci.* **47,** 5447–52 (2006).

79. Mactier, H., Bradnam, M. S. & Hamilton, R. Dark-adapted oscillatory potentials in preterm infants with and without retinopathy of prematurity. *Doc. Ophthalmol.* **127,** 33–40 (2013).

80. Vallabhan, G., Kristiansen, S., Price, J. & Young, R. S. Effect of adaptation and wavelength on the power spectrum of human oscillatory potentials. *Doc. Ophthalmol.* **69,** 145–51 (1988).

81. Van der Torren, K., Groeneweg, G. & van Lith, G. Measuring oscillatory potentials: fourier analysis. *Doc. Ophthalmol.* **69,** 153–9 (1988).

82. Everitt, B. & Hothorn, T. *An Introduction to Applied Multivariate Analysis with R*. 1–273 (Springer Science, 2011).

83. Kruskal, J. B. Multidimensional scaling by optimizing goodness of fit to a nonmetric hypothesis. *Psychometrika* **29,** 1–27 (1964).

84. Shepard, R. The analysis of proximities: multidimensional scaling with an unknown distance function. *Psychometrika* **27,** 125–140 (1962).

85. Holland, S. M. *Non-metric multidimensional scaling (MDS)*. 1–7 (2008). at <http://strata.uga.edu/6370/lecturenotes/multidimensionalScaling.html>

86. Jarrett, S. G., Lin, H., Godley, B. F. & Boulton, M. E. Mitochondrial DNA damage and its potential role in retinal degeneration. *Prog. Retin. Eye Res.* **27,** 596–607 (2008).

87. Niven, J. E. & Laughlin, S. B. Energy limitation as a selective pressure on the evolution of sensory systems. *J. Exp. Biol.* **211,** 1792–1804 (2008).

88. Anderson, B. & Saltzman, H. Retinal oxygen utilization measured by hyperbaric blackout. *Arch. Ophthalmol.* **72,** 792–795 (1964).

89. Yu, D. Y. & Cringle, S. J. Oxygen distribution and consumption within the retina in vascularised and avascular retinas and in animal models of retinal disease. *Prog. Retin. Eye Res.* **20,** 175–208 (2001).

90. Barot, M., Gokulgandhi, M. R. & Mitra, A. K. Mitochondrial dysfunction in retinal diseases. *Curr. Eye Res.* **36,** 1069–77 (2011).

91. Chung, S., Lee, A. & Chung, S. Mouse models for human diseases. *Hong Kong Med. J.* **3,** 201–209 (1997).

92. Tsonis, P. *Animal Models in Eye Research*. 1–215 (Elsevier Ltd, 2008).

93. Klein, J. A. *et al.* The harlequin mouse mutation down-regulates apoptosis-inducing factor. *Nature* **419,** 367–374 (2002).

94. Susin, S. A. *et al.* Molecular characterization of mitochondrial apoptosis-inducing factor. *Nature* **397,** 441–6 (1999).

95. Bénit, P., Goncalves, S., Dassa, E. P., Brière, J. J. & Rustin, P. The variability of the harlequin mouse phenotype resembles that of human mitochondrial-complex I-deficiency syndromes. *PLoS One* **3,** e3208 (2008).

96. Brown, D. *et al.* Loss of Aif function causes cell death in the mouse embryo, but the temporal progression of patterning is normal. *Proc. Natl. Acad. Sci. U. S. A.* **103,** 9918–23 (2006).

97. Joza, N. *et al.* Essential role of the mitochondrial apoptosis-inducing factor in programmed cell death. *Nature* **410,** 549–54 (2001).

98. Vahsen, N. *et al.* AIF deficiency compromises oxidative phosphorylation. *EMBO J.* **23,** 4679–89 (2004).

99. Maté, M. J. *et al.* The crystal structure of the mouse apoptosis-inducing factor AIF. *Nat. Struct. Biol.* **9,** 442–6 (2002).

100. Modjtahedi, N., Giordanetto, F., Madeo, F. & Kroemer, G. Apoptosis-inducing factor: vital and lethal. *Trends Cell Biol.* **16,** 264–72 (2006).

101. Chinta, S. J. *et al.* Reactive oxygen species regulation by AIF- and complex I-depleted brain mitochondria. *Free Radic. Biol. Med.* **46,** 939–947 (2010).

102. Laliberté, A. M., MacPherson, T. C., Micks, T., Yan, A. & Hill, K. A. Vision deficits precede structural losses in a mouse model of mitochondrial dysfunction and progressive retinal degeneration. *Exp. Eye Res.* **93,** 833–41 (2011).

103. Laliberte, A. M. DNA-damage-independent mitochrondrial dysfunction drives a loss of retina function prior to neuron death in the harlequin model of aging. *Biol. London Univ. West. Ontario* 1–145 (2010).

104. Mayers, J. Microglial activation in the harlequin mouse retina as a mechanism for early retinal degeneration. 1–132 (2012).

105. Prtenjaca, A. Cerebellar degeneration in harlequin mice is associated with inflammation unaltered by a phenobarbital hormetic treatment. *Biol. London Univ. West. Ontario* 1–258 (2012).

106. Riemer, J. & Kins, S. Axonal transport and mitochondrial dysfunction in Alzheimer's disease. *Neurodegener. Disord.* **12,** 111–124 (2013).

107. Perier, C. & Vila, M. Mitochondrial biology and Parkinson's disease. *Cold Spring Harb. Perspect. Med.* **2,** a009332 (2012).

108. Leoni, V. & Caccia, C. Study of cholesterol metabolism in Huntington's disease. *Biochem. Biophys. Res. Commun.* **446,** 697–701 (2014).

109. Faes, L. & Callewaert, G. Mitochondrial dysfunction in familial amyotrophic lateral sclerosis. *J. Bioenerg. Biomembr.* **43,** 587–92 (2011).

110. Chen, H. & Chan, D. C. Mitochondrial dynamics--fusion, fission, movement, and mitophagy--in neurodegenerative diseases. *Hum. Mol. Genet.* **18,** R169–76 (2009).

111. Verstreken, P. *et al.* Synaptic mitochondria are critical for mobilization of reserve pool vesicles at Drosophila neuromuscular junctions. *Neuron* **47,** 365–78 (2005).

112. Du, H. *et al.* Early deficits in synaptic mitochondria in an Alzheimer's disease mouse model. *Proc. Natl. Acad. Sci.* **107,** 18670–18675 (2014).

113. Gunter, T. E., Buntinas, L., Sparagna, G., Eliseev, R. & Gunter, K. Mitochondrial calcium transport: mechanisms and functions. *Cell Calcium* **28,** 285–96 (2000).

114. Mbaya, E. *et al.* Calcium signalling-dependent mitochondrial dysfunction and bioenergetics regulation in respiratory chain complex II deficiency. *Cell Death Differ.* **17,** 1855–66 (2010).

115. Simpson, P. B. & Russell, J. T. Role of mitochondrial Ca2+ regulation in neuronal and glial cell signalling. *Brain Res. Brain Res. Rev.* **26,** 72–81 (1998).

116. Ichas, F. & Mazat, J. From calcium signaling to cell death: two conformations for the mitochondrial permeability transition pore. Switching from low- to high-conductance state. *Biochim. Biophys. Acta1* **1366,** 33–50 (1998).

117. Joza, N. *et al.* Muscle-specific loss of apoptosis-inducing factor leads to mitochondrial dysfunction, skeletal muscle atrophy, and dilated cardiomyopathy. *Mol. Cell. Biol.* **25,** 10261–10272 (2005).

118. Pospisilik, J. A. *et al.* Targeted deletion of AIF decreases mitochondrial oxidative phosphorylation and protects from obesity and diabetes. *Cell* **131,** 476–91 (2007).

119. Almeida, A., Almeida, J., Bolaños, J. P. & Moncada, S. Different responses of astrocytes and neurons to nitric oxide: the role of glycolytically generated ATP in astrocyte protection. *Proc. Natl. Acad. Sci. U. S. A.* **98,** 15294–9 (2001).

120. Schapira, A. H. V, Cooper, T. S. J. M., Clark, J. B., Jenner, P. & Marsden, T. C. D. Mitochondrial complex I deficiency in Parkinson's disease. *J. Neurochem.* **54,** 823–827 (1990).

121. Xu, H., Chen, M. & Forrester, J. V. Para-inflammation in the aging retina. *Prog. Retin. Eye Res.* **28,** 348–368 (2009).

122. Medzhitov, R. & Janeway, C. The toll receptor family and microbial recognition. *Trends Microbiol.* **8,** 452–6 (2000).

123. Bianchi, M. E. DAMPs, PAMPs and alarmins: all we need to know about danger. *J. Leukoc. Biol.* **81,** 1–5 (2007).

124. Medzhitov, R. & Janeway, C. A. Decoding the patterns of self and nonself by the innate immune system. *Science (80-. ).* **296,** 298–300 (2002).

125. Scaffidi, P., Misteli, T. & Bianchi, M. E. Release of chromatin protein HMGB1 by necrotic cells triggers inflammation. *Nature* **418,** 191–5 (2002).

126. Herold, K. *et al.* Receptor for advanced glycation end products (RAGE) in a dash to the rescue: inflammatory signals gone awry in the primal response to stress. *J. Leukoc. Biol.* **82,** 204–12 (2007).

127. Spiteller, G. Peroxyl radicals: inductors of neurodegenerative and other inflammatory diseases. Their origin and how they transform cholesterol, phospholipids, plasmalogens, polyunsaturated fatty acids, sugars, and proteins into deleterious products. *Free Radic. Biol. Med.* **41,** 362–87 (2006).

128. Stamatovic, S. M., Keep, R. F., Kunkel, S. L. & Andjelkovic, A. V. Potential role of MCP-1 in endothelial cell tight junction "opening": signaling via Rho and Rho kinase. *J. Cell Sci.* **116,** 4615–28 (2003).

129. Nimmerjahn, A., Kirchhoff, F. & Helmchen, F. Resting microglial cells are highly dynamic surveillants of brain parenchyma in vivo. *Science* **308,** 1314–8 (2005).

130. Haynes, S. E. *et al.* The P2Y12 receptor regulates microglial activation by extracellular nucleotides. *Nat. Neurosci.* **9,** 1512–9 (2006).

131. Langmann, T. Microglia activation in retinal degeneration. *J. Leukoc. Biol.* **81,** 1345–51 (2007).

132. MacPherson, T. Ocular phenotyping in the harlequin mouse model of retinal degeneration: A framework for therapeutic testing. *Biol. London Univ. West. Ontario* 271 (2009).

133. Ibbotson, C. Assessment of retinal dysfunction in memantine-treated and untreated harlequin and wild-type mice using five parameters of the electroretinogram. 1–42 (2012).

134. Xu, Q., Qaum, T. & Adamis, A. P. Sensitive blood – retinal barrier breakdown quantitation using Evans blue. *Invest. Ophthalmol. Vis. Sci.* **42,** 789–794 (2001).

135. Chen, K. B. *et al.* Increase in Evans blue dye extravasation into the brain in the late developmental stage. *Neuroreport* **23,** 699–701 (2012).

136. Radu, M. & Chernoff, J. An in vivo assay to test blood vessel permeability. *J Vis Exp* **73,** e50062 (2013).

137. Matragoon, S. & Liou, G. RNA extraction from single mouse retinas by sand homogenizatoin and the RNeasy Mini procedure. *Qiagen News* **5,** 10–11 (1996).

138. Suzuki, T., Higgins, P. & Crawford, D. Control selection for RNA quantitation. *Biotechniques* **29,** 332–337 (2000).

139. Bustin, S. A. Absolute quantification of mRNA using real-time reverse transcription polymerase chain reaction assays. *J. Mol. Endocrinol.* **25,** 169–93 (2000).

140. Livak, K. J. & Schmittgen, T. D. Analysis of relative gene expression data using real-time quantitative PCR and the 2(-Delta Delta C(T)) Method. *Methods* **25,** 402–408 (2001).

141. Huang, D. W., Sherman, B. T. & Lempicki, R. A. Bioinformatics enrichment tools: paths toward the comprehensive functional analysis of large gene lists. *Nucleic Acids Res.* **37,** 1–13 (2009).

142. Huang, D. W., Sherman, B. T. & Lempicki, R. A. Systematic and integrative analysis of large gene lists using DAVID bioinformatics resources. *Nat. Protoc.* **4,** 44–57 (2009).

143. Cunningham, S. *et al.* A novel model of retinopathy of prematurity simulating preterm oxygen variability in the rat. *Invest. Ophthalmol. Vis. Sci.* **41,** 4275–80 (2000).

144. Hong, H. *et al.* Neonatal systemic inflammation in rats alters retinal vessel development and simulates pathologic features of retinopathy of prematurity. *J. Neuroinflammation* **11,** 87 (2014).

145. Gao, H. & Hollyfield, J. G. Aging of the human retina. *Invest. Ophthalmol. Vis. Sci.* **33,** 1–17 (1992).

146. Kergoat, H., Kergoat, M. J. & Justino, L. Age-related changes in the flash electroretinogram and oscillatory potentials in individuals age 75 and older. *J. Am. Geriatr. Soc.* **49,** 1212–7 (2001).

147. Kolesnikov, A. V, Fan, J., Crouch, R. K. & Kefalov, V. J. Age-related deterioration of rod vision in mice. *J. Neurosci.* **30,** 11222–31 (2010).

148. Dai, D.-F., Rabinovitch, P. S. & Ungvari, Z. Mitochondria and cardiovascular aging. *Circ. Res.* **110,** 1109–24 (2012).

149. Abbott, N. J., Rönnbäck, L. & Hansson, E. Astrocyte-endothelial interactions at the blood-brain barrier. *Nat. Rev. Neurosci.* **7,** 41–53 (2006).

150. Shen, W. *et al.* Conditional Müllercell ablation causes independent neuronal and vascular pathologies in a novel transgenic model. *J. Neurosci.* **32,** 15715–27 (2012).

151. Constable, P. A. & Lawrenson, J. G. Glial cell factors and the outer blood retinal barrier. *Ophthalmic Physiol. Opt.* **29,** 557–64 (2009).

152. Wolf, A. *et al.* Hexokinase 2 is a key mediator of aerobic glycolysis and promotes tumor growth in human glioblastoma multiforme. *J. Exp. Med.* **208,** 313–26 (2011).

153. Bustamante, E. & Pedersen, P. L. High aerobic glycolysis of rat hepatoma cells in culture: role of mitochondrial hexokinase. *Proc. Natl. Acad. Sci. U. S. A.* **74,** 3735–9 (1977).

154. Gatenby, R. A. & Gillies, R. J. Why do cancers have high aerobic glycolysis? *Nat. Rev. Cancer* **4,** 891–9 (2004).

155. Sánchez-Chávez, G., Peña-Rangel, M. T., Riesgo-Escovar, J. R., Martínez-Martínez, A. & Salceda, R. Insulin stimulated-glucose transporter Glut 4 is expressed in the retina. *PLoS One* **7,** e52959 (2012).

156. Uldry, M. & Thorens, B. The SLC2 family of facilitated hexose and polyol transporters. *Pflugers Arch.* **447,** 480–9 (2004).

157. Park, S. Y., Jin, W., Woo, J. R. & Shoelson, S. E. Crystal structures of human TBC1D1 and TBC1D4 (AS160) RabGTPase-activating protein (RabGAP) domains reveal critical elements for GLUT4 translocation. *J. Biol. Chem.* **286,** 18130–8 (2011).

158. Schönfeld, P. & Reiser, G. Why does brain metabolism not favor burning of fatty acids to provide energy? Reflections on disadvantages of the use of free fatty acids as fuel for brain. *J. Cereb. Blood Flow Metab.* **33,** 1493–9 (2013).

159. Meyer, J. S. *et al.* Circulatory and metabolic effects of glycerol infusion in patients with recent cerebral infarction. *Circulation* **51,** 701–712 (1975).

160. Nguyen, N. H. T., Bråthe, A. & Hassel, B. Neuronal uptake and metabolism of glycerol and the neuronal expression of mitochondrial glycerol-3-phosphate dehydrogenase. *J. Neurochem.* **85,** 831–842 (2003).

161. Brown, R. M. *et al.* Pyruvate dehydrogenase E3 binding protein (protein X) deficiency. *Dev. Med. Child Neurol.* **48,** 756–60 (2006).

162. Smeitink, J. A. M. *et al.* Cell biological consequences of mitochondrial NADH: ubiquinone oxidoreductase deficiency. *Curr. Neurovasc. Res.* **1,** 29–40 (2004).

163. Munnich, A. *et al.* Clinical presentations and laboratory investigations in respiratory chain deficiency. *Eur. J. Pediatr.* **155,** 262–74 (1996).

164. Rosenthal, M. D. & Glew, R. H. *Medical Biochemistry: Human Metabolism in Health and Disease*. 1–440 (Science, 2011).

165. Roef, M. J. *et al.* Triacylglycerol infusion improves exercise endurance in patients with mitochondrial myopathy due to complex I deficiency. *Am. J. Clin. Nutr.* **75,** 237–44 (2002).

166. McGuire, L. C., Cruickshank, A. M. & Munro, P. T. Alcoholic ketoacidosis. *Emerg. Med. J.* **23,** 417–20 (2006).

167. Kurtzman, N. A. & Sabatini, S. Bicarbonate therapy in severe metabolic acidosis. *J. Am. Soc. Nephrol.* **20,** 692–695 (2008).

168. Rose, C. R. & Deitmer, J. W. Evidence that glial cells modulate extracellular pH transients induced by neuronal activity in the leech central nervous system. *J. Physiol.* **481 ( Pt 1,** 1–5 (1994).

169. Somjen, G. G. & Balestrino, M. Concentration of carbon dioxide, interstitial pH and synaptic transmission in hippocampal formation of the rat. *J. Physiol.* **396,** 247–266 (1988).

170. Kaila, K. & Ransom, B. R. *pH and Brain Function*. 1–688 (Wiley-Liss, 1998).

171. Brandis, K. Acid-Base Physiology. *Anaesth. MCQ* (2008). at <http://www.anaesthesiamcq.com/AcidBaseBook/ab8_2.php>

172. Jacobs, S. *et al.* Mice with targeted Slc4a10 gene disruption have small brain ventricles and show reduced neuronal excitability. *Proc. Natl. Acad. Sci. U. S. A.* **105,** 311–6 (2008).

173. Chen, Y. Soluble adenylyl cyclase as an evolutionarily conserved bicarbonate sensor. *Science (80-. ).* **289,** 625–628 (2000).

174. Chang, J. C. & Oude-Elferink, R. P. J. Role of the bicarbonate-responsive soluble adenylyl cyclase in pH sensing and metabolic regulation. *Front. Physiol.* **5,** 42 (2014).

175. Li, A. Elucidating early mechanisms of retinal and cerebellar degeneration in the harlequin mouse. 1–45 (2014).

176. Vasiliou, V., Pappa, a & Petersen, D. R. Role of aldehyde dehydrogenases in endogenous and xenobiotic metabolism. *Chem. Biol. Interact.* **129,** 1–19 (2000).

177. O'Brien, P. J., Siraki, A. G. & Shangari, N. Aldehyde sources, metabolism, molecular toxicity mechanisms, and possible effects on human health. *Crit. Rev. Toxicol.* **35,** 609–662 (2005).

178. Mera, K. *et al.* Effect of reactive-aldehydes on the modification and dysfunction of human serum albumin. *J. Pharm. Sci.* **99,** 1614–1625 (2010).

179. Parikh, S. *et al.* A modern approach to the treatment of mitochondrial disease. *Curr Treat Options Neurol* **11,** 414–430 (2013).

180. Bernsen, P. L., Gabreëls, F. J., Ruitenbeek, W. & Hamburger, H. L. Treatment of complex I deficiency with riboflavin. *J. Neurol. Sci.* **118,** 181–7 (1993).

181. Bugiani, M. *et al.* Effects of riboflavin in children with complex II deficiency. *Brain Dev.* **28,** 576–81 (2006).

182. Scholte, H., Busch, H., Bakker, H., Bogaard, J. & Luyt-Houwen, I. Riboflavin-responsive complex I deficiency. *Biochim. Biophys. Acta* **1271,** 75–83 (1995).

183. Ghezzi, D. *et al.* Severe X-linked mitochondrial encephalomyopathy associated with a mutation in apoptosis-inducing factor. *Am. J. Hum. Genet.* **86,** 639–49 (2010).

184. Maglott, D., Ostell, J., Pruitt, K. D. & Tatusova, T. Entrez Gene: gene-centered information at NCBI. *Nucleic Acids Res.* **39,** D52–7 (2011).

**Appendix A. The Canadian Council on Animal Care and The Animal Use Subcommittee of The University Council on Animal Care approval for animal use in research.**

This appendix contains a copy of the 2012 annual approval (**A**) for animal use by the Hill laboratory as well as the 2013 annual approval (**B**) for animal use by the Hill laboratory. Approved by The Canadian Council on Animal Care and The Animal Use Subcommittee of The University Council on Animal Care

# A.

2009-033::3:

**AUP Number:** 2009-033
**AUP Title:** Mutational Mechanisms: Relevance and Role of Oxidative Stress

**Approval Date:** 08/18/2009

The YEARLY RENEWAL to Animal Use Protocol (AUP) 2009-033 has been approved.

1. This AUP number must be indicated when ordering animals for this project.
2. Animals for other projects may not be ordered under this AUP number.
3. Purchases of animals other than through this system must be cleared through the ACVS office. Health certificates will be required.

**REQUIREMENTS/COMMENTS**
Please ensure that individual(s) performing procedures on live animals, as described in this protocol, are familiar with the contents of this document.

The holder of this Animal Use Protocol is responsible to ensure that all associated safety components (biosafety, radiation safety, general laboratory safety) comply with institutional safety standards and have received all necessary approvals. Please consult directly with your institutional safety officers.

**B.**

**AUP Number:** 2009-033

**AUP Title:** Mutational Mechanisms

**Approval Date:** 09/04/2013

**Official Notice of Animal Use Subcommittee (AUS) Approval**: Your new Animal Use Protocol (AUP) entitled "Mutational Mechanisms

" has been APPROVED by the Animal Use Subcommittee of the University Council on Animal Care. This approval, although valid for four years, and is subject to annual Protocol Renewal.2009-033::5

1. This AUP number must be indicated when ordering animals for this project.
2. Animals for other projects may not be ordered under this AUP number.
3. Purchases of animals other than through this system must be cleared through the ACVS office. Health certificates will be required.

The holder of this Animal Use Protocol is responsible to ensure that all associated safety components (biosafety, radiation safety, general laboratory safety) comply with institutional safety standards and have received all necessary approvals. Please consult directly with your institutional safety officers.

## Appendix B. Supplementary Figures and Tables

This appendix contains figures and tables to assist with understanding of presented material.

**Table B.1. PCR Primers used for *Aif* Genotyping**

| Primer Position | Sequence (5' to 3') | Amplicon Length (bp) |
|---|---|---|
| Forward | AGTGTCCAGTCAAAGTACCGGG | 537 (WT) |
| Proviral Forward | GAACAAGGAAGTACAGAGAGAGGC | 725 (*hq*) |
| Reverse | CTATGCCCTTCTCCATGTAGTT | |

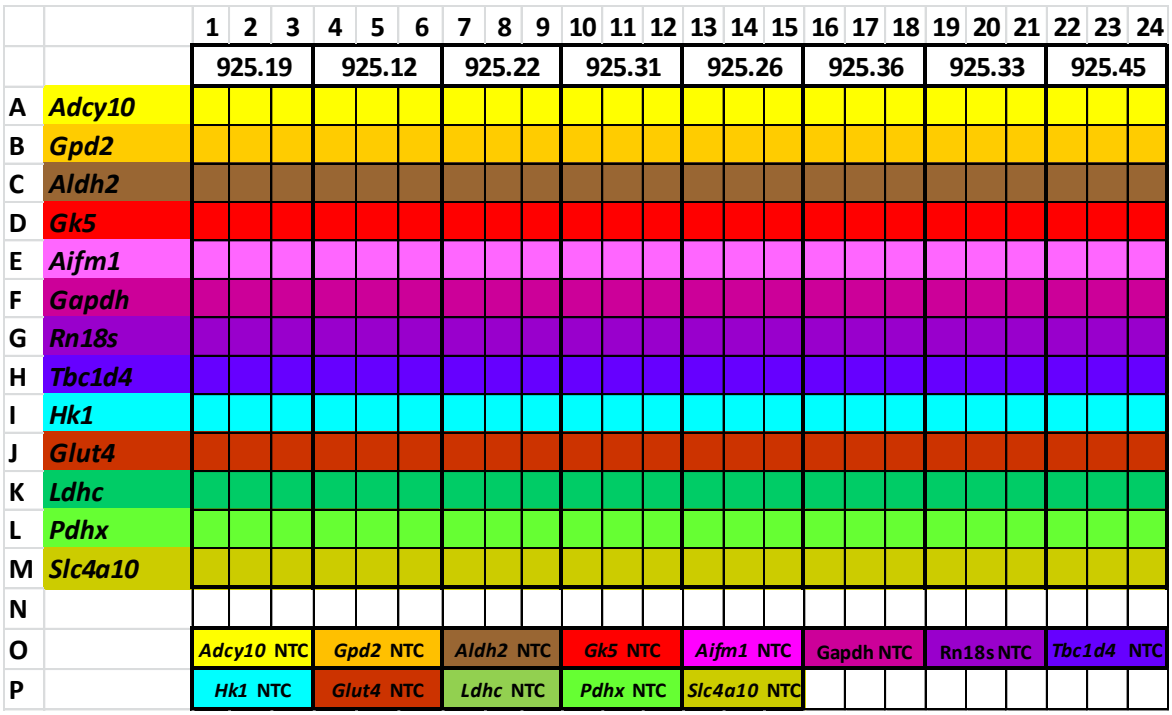


**Figure B.1. A representative diagram of Taqman® block design for 3 month mice.** The 384-well plate is divided into columns of three for each mouse and genes assayed are represented by rows. A total of 13 genes were assayed per mouse in triplicate. A no-template control (NTC) for each gene was assayed in rows O & P to ensure no false amplification and was also assayed in triplicate.

**Table B.2. Pearson's correlation coefficients from nonmetric multidimensional scaling analysis of *hq*Y time-domain OP parameters. Tables are ordered by ascending Coordinate 1 value (left chart) and ascending Coordinate 2 value (right chart) to assist with axis interpretation.**

| Measurement | Coordinate 1 | Coordinate 2 |
|---|---|---|
| *F11 Latency OP2* | *-0.859006334* | *-0.151377761* |
| *F11 Latency OP3* | *-0.853657492* | *-0.15753476* |
| *F9 Latency OP3* | *-0.846274465* | *-0.169707181* |
| *F10 Latency OP2* | *-0.841057093* | *-0.193566945* |
| *F8 Latency OP3* | *-0.830526046* | *-0.065715862* |
| *F10 Latency OP3* | *-0.822981718* | *-0.208552355* |
| *F9 Latency OP2* | *-0.82194351* | *-0.125478715* |
| *F9 Latency OP4* | *-0.80694756* | *-0.298008836* |
| *F8 Latency OP4* | *-0.799695375* | *-0.207521146* |
| *F8 Latency OP2* | *-0.742677191* | *-0.101943569* |
| *F9 Latency OP5* | *-0.733660057* | *-0.250762361* |
| *F10 Latency OP5* | *-0.685039837* | *-0.356267863* |
| *F10 Latency OP4* | *-0.684617696* | *-0.529856532* |
| *F11 Latency OP4* | *-0.638909514* | *-0.589130854* |
| *F11 Latency OP5* | *-0.468400077* | *-0.541219708* |
| *F8 Latency OP5* | *-0.344040045* | *-0.265368694* |
| *F11 Amplitude OP2* | *0.424307269* | *-0.412374408* |
| *F10 Amplitude OP5* | *0.481785605* | *0.164778075* |
| *F10 Amplitude OP2* | *0.543878698* | *-0.644420042* |
| *F9 Amplitude OP2* | *0.560034669* | *-0.66660931* |
| *F11 Amplitude OP5* | *0.578306152* | *0.186810407* |
| *F8 Amplitude OP3* | *0.599566532* | *-0.557316795* |
| *F8 Amplitude OP2* | *0.618144453* | *-0.461141832* |
| *F9 Amplitude OP5* | *0.65045626* | *-0.111703757* |
| *F8 Amplitude OP5* | *0.672790759* | *-0.40557432* |
| *F8 Amplitude OP4* | *0.684464179* | *-0.552811113* |
| *F9 Amplitude OP4* | *0.728464308* | *-0.343319214* |
| *F9 Amplitude OP3* | *0.729042222* | *-0.615488338* |
| *F10 Amplitude OP4* | *0.748886709* | *0.043278448* |
| *F11 Amplitude OP4* | *0.799065572* | *0.162761807* |
| *F10 Amplitude OP3* | *0.812086192* | *-0.448484634* |
| *F11 Amplitude OP3* | *0.870065089* | *-0.178484534* |

| Measurement | Coordinate 1 | Coordinate 2 |
|---|---|---|
| *F9 Amplitude OP2* | *0.560034669* | *-0.66660931* |
| *F10 Amplitude OP2* | *0.543878698* | *-0.644420042* |
| *F9 Amplitude OP3* | *0.729042222* | *-0.615488338* |
| *F11 Latency OP4* | *-0.638909514* | *-0.589130854* |
| *F8 Amplitude OP3* | *0.599566532* | *-0.557316795* |
| *F8 Amplitude OP4* | *0.684464179* | *-0.552811113* |
| *F11 Latency OP5* | *-0.468400077* | *-0.541219708* |
| *F10 Latency OP4* | *-0.684617696* | *-0.529856532* |
| *F8 Amplitude OP2* | *0.618144453* | *-0.461141832* |
| *F10 Amplitude OP3* | *0.812086192* | *-0.448484634* |
| *F11 Amplitude OP2* | *0.424307269* | *-0.412374408* |
| *F8 Amplitude OP5* | *0.672790759* | *-0.40557432* |
| *F10 Latency OP5* | *-0.685039837* | *-0.356267863* |
| *F9 Amplitude OP4* | *0.728464308* | *-0.343319214* |
| *F9 Latency OP4* | *-0.80694756* | *-0.298008836* |
| *F8 Latency OP5* | *-0.344040045* | *-0.265368694* |
| *F9 Latency OP5* | *-0.733660057* | *-0.250762361* |
| *F10 Latency OP3* | *-0.822981718* | *-0.208552355* |
| *F8 Latency OP4* | *-0.799695375* | *-0.207521146* |
| *F10 Latency OP2* | *-0.841057093* | *-0.193566945* |
| *F11 Amplitude OP3* | *0.870065089* | *-0.178484534* |
| *F9 Latency OP3* | *-0.846274465* | *-0.169707181* |
| *F11 Latency OP3* | *-0.853657492* | *-0.15753476* |
| *F11 Latency OP2* | *-0.859006334* | *-0.151377761* |
| *F9 Latency OP2* | *-0.82194351* | *-0.125478715* |
| *F9 Amplitude OP5* | *0.65045626* | *-0.111703757* |
| *F8 Latency OP2* | *-0.742677191* | *-0.101943569* |
| *F8 Latency OP3* | *-0.830526046* | *-0.065715862* |
| *F10 Amplitude OP4* | *0.748886709* | *0.043278448* |
| *F11 Amplitude OP4* | *0.799065572* | *0.162761807* |
| *F10 Amplitude OP5* | *0.481785605* | *0.164778075* |
| *F11 Amplitude OP5* | *0.578306152* | *0.186810407* |

**Table B.3. Pearson's correlation coefficients from nonmetric multidimensional scaling analysis of *hq*Y frequency-domain OP parameters. Tables are ordered by ascending Coordinate 1 value (left chart) and ascending Coordinate 2 value (right chart) to assist with axis interpretation.**

| Measurement | Coordinate 1 | Coordinate 2 |
|---|---|---|
| *F10 Total Energy* | *-0.97963505* | *-0.080079919* |
| *F11 Total Energy* | *-0.968656764* | *0.088457664* |
| *F9 Total Energy* | *-0.938426703* | *-0.236289954* |
| *F11 Gaussian Power* | *-0.837221842* | *-0.260841987* |
| *F10 Gaussian Frequency* | *-0.821513771* | *0.543230455* |
| *F8 Total Energy* | *-0.817230902* | *-0.292346888* |
| *F9 Gaussian Frequency* | *-0.810590977* | *0.546777937* |
| *F8 Gaussian Frequency* | *-0.784149192* | *0.563671382* |
| *Frequency* | *-0.776138181* | *0.594753436* |
| *F10 Gaussian Power* | *-0.735730899* | *-0.563367817* |
| *F9 Gaussian Power* | *-0.590242553* | *-0.770721391* |
| *F8 Gaussian Power* | *-0.439755859* | *-0.745030923* |

| Measurement | Coordinate 1 | Coordinate 2 |
|---|---|---|
| *F9 Gaussian Power* | *-0.590242553* | *-0.770721391* |
| *F8 Gaussian Power* | *-0.439755859* | *-0.745030923* |
| *F10 Gaussian Power* | *-0.735730899* | *-0.563367817* |
| *F8 Total Energy* | *-0.817230902* | *-0.292346888* |
| *F11 Gaussian Power* | *-0.837221842* | *-0.260841987* |
| *F9 Total Energy* | *-0.938426703* | *-0.236289954* |
| *F10 Total Energy* | *-0.97963505* | *-0.080079919* |
| *F11 Total Energy* | *-0.968656764* | *0.088457664* |
| *F10 Gaussian Frequency* | *-0.821513771* | *0.543230455* |
| *F9 Gaussian Frequency* | *-0.810590977* | *0.546777937* |
| *F8 Gaussian Frequency* | *-0.784149192* | *0.563671382* |
| *F11 Gaussian Frequency* | *-0.776138181* | *0.594753436* |

**Table B.4. Pearson's correlation coefficients from nonmetric multidimensional scaling analysis of *hq*X frequency-domain OP parameters. Tables are ordered by ascending Coordinate 1 value (left chart) and ascending Coordinate 2 value (right chart) to assist with axis interpretation.**

| Measurement | Coordinate 1 | Coordinate 2 |
|---|---|---|
| *F10 Latency OP2* | *-0.8465227* | *-0.33263146* |
| *F9 Latency OP2* | *-0.84122833* | *-0.26833499* |
| *F10 Latency OP3* | *-0.8286985* | *-0.28526331* |
| *F11 Latency OP3* | *-0.7839018* | *-0.39646655* |
| *F9 Latency OP4* | *-0.78382521* | *-0.21714434* |
| *F10 Latency OP5* | *-0.77789174* | *-0.07591251* |
| *F8 Latency OP2* | *-0.75190675* | *-0.47672993* |
| *F8 Amplitude OP3* | *-0.74317829* | *-0.22739861* |
| *F11 Latency OP2* | *-0.73761625* | *-0.47558814* |
| *F8 Amplitude OP4* | *-0.73351111* | *-0.04430713* |
| *F9 Latency OP5* | *-0.72513157* | *-0.46055913* |
| *F10 Latency OP4* | *-0.67806932* | *-0.06781597* |
| *F11 Latency OP4* | *-0.63576058* | *-0.55236009* |
| *F9 Latency OP3* | *-0.61737348* | *-0.35646637* |
| *F8 Amplitude OP5* | *-0.59553985* | *-0.2987983* |
| *F11 Latency OP5* | *-0.27739875* | *-0.23479761* |
| *F10 Amplitude OP5* | *0.12469163* | *-0.71649367* |
| *F11 Amplitude OP5* | *0.1437659* | *-0.68752732* |
| *F9 Amplitude OP5* | *0.33357947* | *-0.71742454* |
| *F9 Amplitude OP4* | *0.37176222* | *-0.87729291* |
| *F10 Amplitude OP4* | *0.3800024* | *-0.8572363* |
| *F8 Amplitude OP4* | *0.42295653* | *-0.74131346* |
| *F11 Amplitude OP4* | *0.48735872* | *-0.64154307* |
| *F8 Amplitude OP5* | *0.50542379* | *-0.54592269* |
| *F9 Amplitude OP3* | *0.59040284* | *-0.36471528* |
| *F8 Amplitude OP3* | *0.61054609* | *-0.72685793* |
| *F10 Amplitude OP3* | *0.64286454* | *-0.50677443* |
| *F8 Amplitude OP2* | *0.65078245* | *-0.34984908* |
| *F9 Amplitude OP2* | *0.68950648* | *-0.52237812* |
| *F10 Amplitude OP2* | *0.76133209* | *-0.36759832* |
| *F11 Amplitude OP3* | *0.76840952* | *-0.57446596* |
| *F11 Amplitude OP2* | *0.78171173* | *-0.41812742* |

| Measurement | Coordinate 1 | Coordinate 2 |
|---|---|---|
| *F9 Amplitude OP4* | *0.37176222* | *-0.87729291* |
| *F10 Amplitude OP4* | *0.3800024* | *-0.8572363* |
| *F8 Amplitude OP4* | *0.42295653* | *-0.74131346* |
| *F8 Amplitude OP3* | *0.61054609* | *-0.72685793* |
| *F9 Amplitude OP5* | *0.33357947* | *-0.71742454* |
| *F10 Amplitude OP5* | *0.12469163* | *-0.71649367* |
| *F11 Amplitude OP5* | *0.1437659* | *-0.68752732* |
| *F11 Amplitude OP4* | *0.48735872* | *-0.64154307* |
| *F11 Amplitude OP3* | *0.76840952* | *-0.57446596* |
| *F11 Latency OP4* | *-0.63576058* | *-0.55236009* |
| *F8 Amplitude OP5* | *0.50542379* | *-0.54592269* |
| *F9 Amplitude OP2* | *0.68950648* | *-0.52237812* |
| *F10 Amplitude OP3* | *0.64286454* | *-0.50677443* |
| *F8 Latency OP2* | *-0.75190675* | *-0.47672993* |
| *F11 Latency OP2* | *-0.73761625* | *-0.47558814* |
| *F9 Latency OP5* | *-0.72513157* | *-0.46055913* |
| *F11 Amplitude OP2* | *0.78171173* | *-0.41812742* |
| *F11 Latency OP3* | *-0.7839018* | *-0.39646655* |
| *F10 Amplitude OP2* | *0.76133209* | *-0.36759832* |
| *F9 Amplitude OP3* | *0.59040284* | *-0.36471528* |
| *F9 Latency OP3* | *-0.61737348* | *-0.35646637* |
| *F8 Amplitude OP2* | *0.65078245* | *-0.34984908* |
| *F10 Latency OP2* | *-0.8465227* | *-0.33263146* |
| *F8 Amplitude OP5* | *-0.59553985* | *-0.2987983* |
| *F10 Latency OP3* | *-0.8286985* | *-0.28526331* |
| *F9 Latency OP2* | *-0.84122833* | *-0.26833499* |
| *F11 Latency OP5* | *-0.27739875* | *-0.23479761* |
| *F8 Amplitude OP3* | *-0.74317829* | *-0.22739861* |
| *F9 Latency OP4* | *-0.78382521* | *-0.21714434* |
| *F10 Latency OP5* | *-0.77789174* | *-0.07591251* |
| *F10 Latency OP4* | *-0.67806932* | *-0.06781597* |
| *F8 Amplitude OP4* | *-0.73351111* | *-0.04430713* |

**Table B.5. Pearson's correlation coefficients from nonmetric multidimensional scaling analysis of *hq*X frequency-domain OP parameters. Tables are ordered by ascending Coordinate 1 value (left chart) and ascending Coordinate 2 value (right chart) to assist with axis interpretation.**

| Measurement | Coordinate 1 | Coordinate 2 |
|---|---|---|
| ***F9 Total Energy*** | *-0.969372022* | *0.053267539* |
| ***F10 Total Energy*** | *-0.96440625* | *0.209308386* |
| ***F11 Gaussian Power*** | *-0.947405504* | *0.019228962* |
| ***F10 Gaussian Power*** | *-0.936559689* | *-0.249515924* |
| ***F8 Total Energy*** | *-0.925313065* | *0.134905804* |
| ***F11 Total Energy*** | *-0.898996534* | *0.364182853* |
| ***F9 Gaussian Power*** | *-0.852374157* | *-0.462860557* |
| ***F8 Gaussian Power*** | *-0.778672152* | *-0.477976579* |
| ***F8 Gaussian Frequency*** | *-0.103790027* | *0.939471085* |
| ***F9 Gaussian Frequency*** | *-0.088637167* | *0.951935284* |
| ***F10 Gaussian Frequency*** | *-0.062301485* | *0.980003901* |
| ***F11 Gaussian Frequency*** | *-0.045683178* | *0.969829489* |

| Measurement | Coordinate 1 | Coordinate 2 |
|---|---|---|
| ***F8 Gaussian Power*** | *-0.778672152* | *-0.477976579* |
| ***F9 Gaussian Power*** | *-0.852374157* | *-0.462860557* |
| ***F10 Gaussian Power*** | *-0.936559689* | *-0.249515924* |
| ***F11 Gaussian Power*** | *-0.947405504* | *0.019228962* |
| ***F9 Total Energy*** | *-0.969372022* | *0.053267539* |
| ***F8 Total Energy*** | *-0.925313065* | *0.134905804* |
| ***F10 Total Energy*** | *-0.96440625* | *0.209308386* |
| ***F11 Total Energy*** | *-0.898996534* | *0.364182853* |
| ***F8 Gaussian Frequency*** | *-0.103790027* | *0.939471085* |
| ***F9 Gaussian Frequency*** | *-0.088637167* | *0.951935284* |
| ***F11 Gaussian Frequency*** | *-0.045683178* | *0.969829489* |
| ***F10 Gaussian Frequency*** | *-0.062301485* | *0.980003901* |

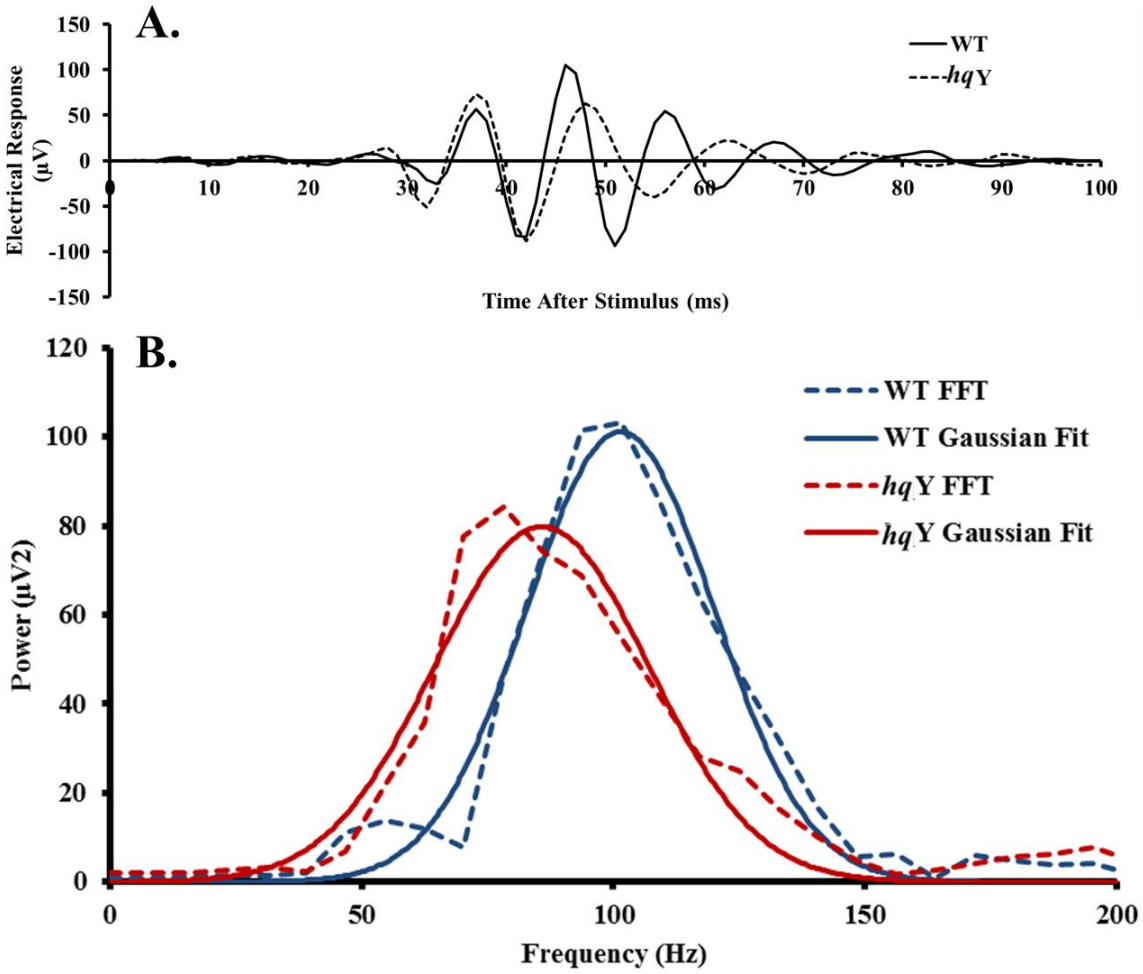


**Figure B.2. A schematic representation of OP parameters elicited by a three month *hq*Y and wild-type mouse (10 cd•s/m$^2$ stimulus).** (**A**) Time-domain representation of ERG OP parameters indicate functional changes as early as three months of age with changes in OP periodicity. (**B**) Frequency-domain representation of ERG OP parameters at three months indicate functional changes in OP frequency. It is evident that power, and total energy are decreased in this schematic representation.

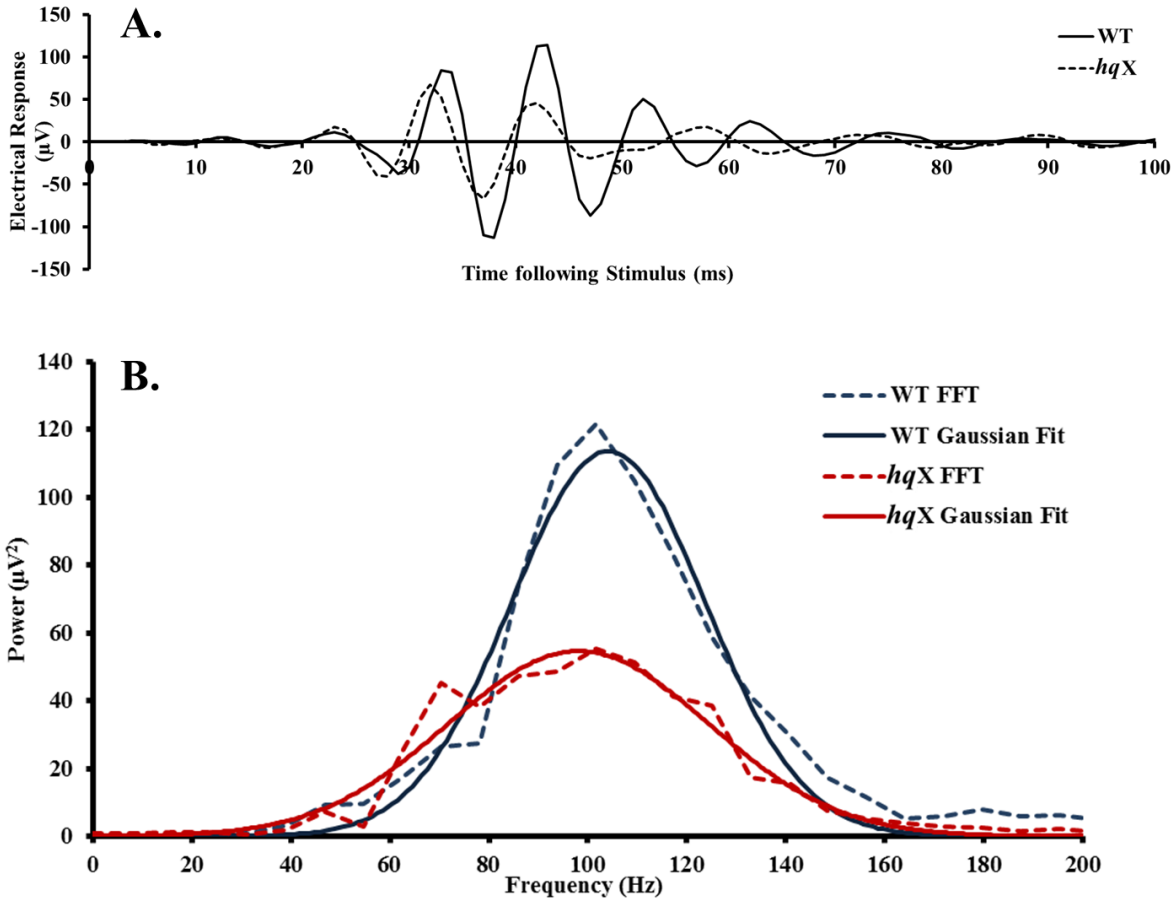


**Figure B.3. A schematic representation of OP parameters elicited by an eleven month *hq*X and wild-type mouse (10 cd•s/m$^2$ stimulus).** (**A**) Time-domain representation of ERG OP parameters indicate functional changes at eleven months of age with changes in OP amplitude. (**B**) Frequency-domain representation of ERG OP parameters at eleven months indicate functional changes in OP total energy and power. It is evident that OP frequency remains unchanged in this schematic representation.

**Table B.6. Two-way ANOVA's performed in Excel [Microsoft, Redmond, VA] on oscillatory potentials parameters both in the time and frequency domain to explore the effect of age on genotype. Significance is equal to $p < 0.05$.**

**A.**

| ***hq*Y Time-Domain Parameters** | | |
|---|---|---|
| **Initial Latency** | | **Summed Amplitude** |
| Genotype ($p < 0.001$) | | Genotype ($p < 0.001$) |
| Age ($p = 0.07337$) | | Age = ($p < 0.001$) |
| Interaction ($p = 0.212$) | | Interaction ($p < 0.01$) |

**B.**

| ***hq*Y Frequency-Domain Parameters** | | |
|---|---|---|
| **Peak Frequency** | **Peak Power** | **Total Energy** |
| Genotype ($p < 0.001$) | Genotype ($p < 0.05$) | Genotype ($p < 0.01$) |
| Age ($p < 0.001$) | Age ($p < 0.01$) | Age ($p < 0.01$) |
| Interaction ($p < 0.05$) | Interaction ($p < 0.01$) | Interaction ($p < 0.01$) |

**C.**

| ***hq*X Time-Domain Parameters** | | |
|---|---|---|
| **Initial Latency** | | **Summed Amplitude** |
| Genotype ($p < 0.01$) | | Genotype ($p < 0.001$) |
| Age ($p < 0.001$) | | Age ($p = 0.63994$ ) |
| Interaction ($p = 0.212$) | | Interaction ($p = 0.15089$) |

**D.**

| ***hq*X Frequency-Domain Parameters** | | |
|---|---|---|
| **Peak Frequency** | **Peak Power** | **Total Energy** |
| Genotype ($p < 0.01$) | Genotype ($p < 0.001$) | Genotype ($p < 0.001$) |
| Age ($p < 0.001$) | Age ($p < 0.01$) | Age ($p = 0.7796$) |
| Interaction ($p = 0.88369$) | Interaction ($p = 0.16913$) | Interaction ($p = 0.13802$) |

**Table B.7. Concentrations and quality assurance measures for extracted retinal and cerebellar RNA samples.**

| | | Retina | | | | Cerebellum | | | |
|---|---|---|---|---|---|---|---|---|---|
| | | **Sample ID** | **Concentration (ng/µL)** | **A260/A280** | **RIN** | **Sample ID** | **Concentration (ng/µL)** | **A260/A280** | **RIN** |
| 4 Month | *hq* | ***924.3** | 33.9 | 2.06 | 9.6 | ***924.3** | 257.2 | 2.028 | 9.3 |
| | | ***925.16** | 41.7 | 2.04 | 9.6 | ***925.16** | 185.6 | 2.053 | 9.2 |
| | | ***925.77** | 44.9 | 2.03 | 9.5 | ***925.77** | 232 | 2.064 | 8.8 |
| | | ***925.83** | 72.2 | 2.21 | 8.9 | **925.83** | 287.6 | 2.043 | 8.7 |
| | | **925.89** | n/a | n/a | n/a | ***925.89** | 231.2 | 2.141 | 8.8 |
| | | **925.90** | 24 | 2.1 | 9.1 | **925.90** | n/a | n/a | n/a |
| | | ***925.93** | 72.3 | 2.13 | 9.2 | **925.93** | n/a | n/a | n/a |
| | WT | **924.4** | n/a | n/a | n/a | ***924.4** | 273.2 | 1.957 | 9.3 |
| | | ***924.5** | 16.3 | 2.43 | 8.9 | **924.5** | n/a | n/a | n/a |
| | | ***924.11** | 23.7 | 2.01 | 9.3 | **924.11** | n/a | n/a | n/a |
| | | ***925.14** | 34.1 | 2.02 | 9.2 | ***925.14** | 140 | 1.977 | 8.8 |
| | | **925.72** | n/a | n/a | n/a | **925.72** | 146 | 2.086 | 9.1 |
| | | ***925.73** | 29.1 | 2.18 | 8.8 | ***925.73** | 140 | 2.077 | 8.9 |
| | | **925.75** | 12.1 | 2.59 | 8.4 | ***925.75** | 210 | 2.315 | 9.2 |
| | | ***925.95** | 41.1 | 2.11 | 9.1 | **925.95** | n/a | n/a | n/a |
| 3 Month | *hq* | ***925.19** | 32.7 | 2.15 | 8.8 | ***925.19** | 212 | 2.008 | 8 |
| | | ***925.22** | 16.2 | 1.85 | 8.2 | ***925.22** | 210 | 2.05 | 9.1 |
| | | ***925.26** | 32 | 2.04 | 9.6 | **925.26** | 216 | 2.050 | 7.5 |
| | | **925.27** | 35.6 | 2.05 | 9 | ***925.27** | 240 | 2.040 | 8.2 |
| | | ***925.33** | 33.6 | 2.02 | 9.8 | ***925.33** | 154 | 1.873 | 9.1 |
| | WT | ***925.12** | 43.9 | 2.05 | 8.9 | ***925.12** | 353.6 | 2.007 | 7.7 |
| | | **925.13** | 12.8 | 2.23 | None | **925.13** | 240 | 1.911 | 7.6 |
| | | ***925.31** | 53.4 | 2.03 | 9.8 | ***925.31** | 84 | 1.812 | 8.8 |
| | | ***925.36** | 29.6 | 2.1 | 9.4 | ***925.36** | 214 | 2.030 | 8.3 |
| | | ***925.45** | 47.1 | 2.18 | 9.9 | ***925.45** | 85 | 2.095 | 9.2 |
| 2 Month | *hq* | ***925.53** | 26.6 | 2.12 | 9.5 | ***925.53** | 215 | 2.011 | 8.8 |
| | | **925.54** | 8.2 | 2.21 | 9.2 | ***925.54** | 182 | 1.97 | 8.8 |
| | | ***925.55** | 52.9 | 2.11 | 9.6 | **925.55** | 199.6 | 1.965 | 9.3 |
| | | ***925.69** | 27 | 2.13 | 9.2 | ***925.69** | 221.6 | 1.965 | 8.9 |
| | | ***925.70** | 50.2 | 2.1 | 9.6 | ***925.70** | 167.2 | 2.133 | 9.1 |
| | WT | ***925.39** | 44.4 | 2.1 | 9.8 | **925.39** | 110 | 2.202 | 8.9 |
| | | ***925.43** | 31 | 2.18 | 9.6 | ***925.43** | 310 | 2.102 | 8.5 |
| | | ***925.51** | 32.3 | 2.03 | 9.4 | ***925.51** | 194 | 2.008 | 9 |
| | | ***925.58** | 36.1 | 2.15 | 9.1 | ***925.58** | 188 | 1.983 | 8.6 |
| | | **925.57** | 17 | 2.36 | 8.6 | ***925.57** | 209.2 | 2.135 | 9 |

*Indicates sample that was chosen for transcriptome analysis. In addition, light shadings indicate that the sample was not used.

## Appendix C. MATLAB functions and Scripts

This appendix contains MATLAB scripts for the isolation of oscillatory potentials from the original ERG waveform and fast Fourier transformation.

**MATLAB Script A. "P3fit" function written into MATLAB for modelling photoreceptor contribution to the ERG.**

```
function err = p3fit(rktd)

global datatofit timestofit

options.MaxFunEvals=1000000;

i = find(timestofit<rktd(3));

model(i) = 0;

j = find(timestofit>=rktd(3));

model(j)      =      rktd(1)*(1-exp(-rktd(2)*(timestofit(j)-
rktd(3)).*(timestofit(j)-rktd(3))));

err = sum((model' - datatofit).^2);
```

**MATLAB Script B. "P3driver" function written into MATLAB for modelling photoreceptor contribution to the ERG, followed by a fifth order Butterworth transformation (65-300Hz) for oscillatory potential waveform extraction.**

```
global datatofit timestofit

options.MaxFunEvals=1000000;
for icol = 16:19

clear model

%modelling the p3
%details
minval = min(data(:,icol));
imin = find(data(:,icol) == minval);
iremain = data(imin+1:200,icol);
timestofit = data(1:imin,1);
datatofit = data(1:imin,icol);
datatofit = datatofit - datatofit(1);

initialguess = [ min(datatofit) 0.5 0];

rktd = fminsearch(@p3fit,initialguess);

i = find(timestofit<rktd(3));
model(i) = 0;
j = find(timestofit>=rktd(3));
model(j)      =      rktd(1)*(1-exp(-rktd(2)*(timestofit(j)-
rktd(3)).*(timestofit(j)-rktd(3))));
k = (find(iremain)+(imin));
model(k) = min(model);
```

```
timestoplot(i) = i;
timestoplot(j) = j;
timestoplot(k) = k;

%Subtracting model from data to form p2

p2(i) = ((data(i,icol)-data(1,icol)) - model(i)');
p2(j) = ((data(j,icol)-data(1,icol)) - model(j)');
p2(k) = ((data(k,icol)-data(1,icol)) - model(k)');

%Butterworth filtering the p2
Wn = [65 300] / 500;
[B,A] = butter(5,Wn);
fildata = filter(B,A,p2);

%Plots to see how things are going
figure
subplot(2,1,1),hold on,
plot(data(:,1),data(:,icol)-data(1,icol));
plot(timestoplot,model,'r');
plot(timestoplot,p2,'g');
plot(timestoplot,fildata,'black');
subplot(2,1,2),plot(timestoplot,fildata,'black');

end
```

**MATLAB Script C. "P3driverFFT" function written into MATLAB for modelling photoreceptor contribution to the ERG, followed by a fifth order Butterworth transformation (65-300Hz) and fast Fourier transformation (Gaussian).**

```
global datatofit timestofit

options.MaxFunEvals=1000000;
for icol = 16;

clear model

%modelling the p3

%details
minval = min(data(:,icol));
imin = find(data(:,icol) == minval);
iremain = data(imin+1:200,icol);
timestofit = data(1:imin,1);
datatofit = data(1:imin,icol);
datatofit = datatofit - datatofit(1);

initialguess = [ min(datatofit) 0.5 0];

rktd = fminsearch(@p3fit,initialguess);

i = find(timestofit<rktd(3));
model(i) = 0;
j = find(timestofit>=rktd(3));
model(j)      =      rktd(1)*(1-exp(-rktd(2)*(timestofit(j)-
rktd(3)).*(timestofit(j)-rktd(3))));
k = (find(iremain)+(imin));
model(k) = min(model);
timestoplot(i) = i;
timestoplot(j) = j;
timestoplot(k) = k;

%Subtracting model from data to form p2

p2(i) = ((data(i,icol)-data(1,icol)) - model(i)');
p2(j) = ((data(j,icol)-data(1,icol)) - model(j)');
p2(k) = ((data(k,icol)-data(1,icol)) - model(k)');

%Butterworth filtering the p2
Wn = [65 300] / 500;
[B,A] = butter(5,Wn);
fildata = filter(B,A,p2);
```

```
fs = 1000;                              % Sample frequency (Hz)
t = 0:1/fs:0.2-1/fs;                    % 10 sec sample
x = (fildata);

b = fildata(1:128);           % Window length
m = length(b);
n = pow2(nextpow2(m));  % Transform length
y = fft(x,n);           % DFT
f = (0:n-1)*(fs/n);     % Frequency range
p = sqrt(y.*conj(y)/n);   % Power of the DFT


plot(f(1:floor(n/2)),p(1:floor(n/2)))
xlabel('Frequency (Hz)')
ylabel('Power')
title('{\bf Periodogram}')

A=((p(1)/2 +sum (p(2:end-1) + p(end)/2))/2) % area under
the curve

%Plots to see how things are going
%figure
%subplot(2,1,1),hold on,
%plot(data(:,1),data(:,icol)-data(1,icol));
%lot(timestoplot,model,'r');
%plot(timestoplot,p2,'g');
%plot(timestoplot,fildata,'black');
%subplot(2,1,2),plot(timestoplot,fildata,'black');


g = fit(f.',p.','gauss2')

plot(g)

end
```

## Appendix D. Non-metric multidimensional scaling R code.

This appendix contains R code for performing non-metric multidimensional scaling on oscillatory potential parameters in both the time and frequency domain.

**NMDS R-code A. Non-metric multidimensional scaling performed by calculating Euclidean distances between samples followed by subsequent correlation analysis.**

```
> getwd()
# This will list the location that R will read files from

> list.files()
#List of all files in the working directory

> data <- read.csv("ZSCORES HQY&XY FFT DATA.csv")
# Information in file will become a variable named "data"

> data
# View "data" variable

> (D <- dist(data))
# This will calculate Euclidean distance between each
sample based on input z-scores. Presented as a
#dissimilarity matrix, assigned as variable D.

> summary (D)
# Displays dissimilarity matrix

> library ("MASS")
# Reads in library package to perform NMDS
# Install the HSAUR2 package

> data_mds <- isoMDS(D)
# This will perform NMDS on the dissimilarity matrix (D)
based on 50 iterations. Assigns NMDS as #data_mds

> x <- data_mds$Points[,1]
# Assigns the first coordinate of the NMDS variables to the
variable x

> y <- data_mds$Points [,2]
# Assigns the first coordinate of the NMDS variables to the
variable y
# Variables plotted in excel
# NMDS coordinates put into a new z-score file and read
into excel for correlation analysis

> x <- read.csv("ZSCORES (Coorelation) HQY&XY FFT DATA
(ERIC DOLINAR).csv")
```

```
# Assigns variable x to z-score file with NMDS coordinates

> cor(x, use = "complete.obs", method = "pearson")
# Performs a Pearson's correlation on the variable x

# Shepard plots

> MDS.sh <- Shepard (D, data_mds$points)

> plot(MDS.sh, pch =".")

> plot(MDS.sh, pch =".", xlab = "Dissimilarity", ylab =
"Distance")

> lines(MDS.sh$x, MDS.sh$yf, type="S")
```

## Appendix E. Functional annotation of differentially expressed retinal genes

This appendix contains functional annotations based on NCBI Gene searches[184] of 521 retinal genes differentially expressed in *hq* mice at four months of age. Differential expression is based on a retinal gene expression microarray [Affymetrix, Mouse Gene 1.0 ST Array, Santa Clara] previously performed by the Hill laboratory.[102]

**Table E.1. Functional annotation of 521 differentially expressed retinal genes based on microarray data from four-month-old *hq* disease mice.[*]**

| Gene Symbol | p-value‡ | Fold Change | Annotation/Function† |
|---|---|---|---|
| *Aifm1* | 0.000163 | -6.01196 | Mitochondrial intermembrane flavoprotein involved in OXPHOS and apoptosis |
| *Cyp3a25* | 0.0307866 | -4.68949 | Cytochrome P450 variant involved in metal binding and oxidoreductase activity |
| *Hc* | 0.0116071 | -3.90775 | Complement activation (C5) and innate immune response |
| *Ttc18* | 0.0024609 | -3.43071 | Extracellular vesicular exosome important to ciliated cells |
| *Trim36* | 0.0275573 | -3.41135 | Ubiquitin ligase activity with zinc-binding protein activity |
| *Abca6* | 0.0450953 | -3.09029 | ATP-binding cassette involved in macrophage lipid metabolism and homeostasis |
| *Iqgap2* | 0.0440039 | -3.01678 | Regulates cell morphology and mobility through interaction with the cytoskeleton |
| *Myh6* | 0.0058866 | -2.90362 | Encodes heavy chain of myosin, an intracellular motor protein |
| *Slc4a10* | 0.0266117 | -2.87259 | Neuronal intracellular bicarbonate transporter and pH regulator |
| *Robo3* | 0.0008035 | -2.81071 | Controls neurite outgrowth and axonal navigation |
| *Olfm4* | 0.015151 | -2.77354 | Antiapoptotic protein and facilitates cell adhesion |
| *Haus6* | 0.0362302 | -2.70602 | Microtubule and kinetochore assembly |
| *Atm* | 0.0358792 | -2.69275 | Cell cycle checkpoint kinase protein |
| *Nbr1* | 0.0227154 | -2.64043 | Peroxisome autophagic degradation |
| *BC030307* | 0.0060405 | -2.62532 | Unknown |
| *Slc26a4* | 0.0160909 | -2.60606 | Sulfate and chloride transporter |
| *Dpy19l1* | 0.0274067 | -2.54374 | Unknown |
| *Ppp1r9a* | 0.0149737 | -2.53199 | Phosphatase I involved in cytoskeleton organization |
| *4930519F16Rik* | 0.0061143 | -2.51977 | Unknown |
| *Wdr60* | 0.0071325 | -2.51121 | Cell cycle regulator and formation of cilia |
| *D19Ertd652e* | 0.0298091 | -2.50222 | Unknown |
| *Pdhx* | 0.0161061 | -2.48204 | Structural component of pyruvate dehydrogenase, binds subunits together |
| *Aqp4* | 0.0018312 | -2.47148 | Neuronal aquaporin to allow water-selective transport |
| *Pkd1l2* | 0.0066857 | -2.46823 | Cation channel pore, cation transport |
| *Siglece* | 0.0321588 | -2.46084 | Sialic acid binding protein involved in immune cell response |
| *BC055324* | 0.0449079 | -2.40619 | Unknown |
| *Garnl1* | 0.0495052 | -2.38863 | Activation of Ral GTPase |
| *Smc1b* | 0.0466303 | -2.3795 | Mitotic and meiotic DNA recombination and chromatid formation |
| *Klra5* | 0.0094125 | -2.36588 | Membrane protein involved in cellular adhesion during immune response |
| *Pear1* | 0.0419941 | -2.35637 | Responsible for platelet aggregation |

| | | | |
|---|---|---|---|
| *Trio* | 0.0159855 | -2.345 | Promotes leukocyte transendotheial migration |
| *Adal* | 0.0032844 | -2.3368 | Purine, drug and small molecule catabolism |
| *Kmo* | 0.0428267 | -2.32506 | Mitochondrial protein involved in NADH oxidase activity and FAD binding |
| *4922505G16Rik* | 0.0380333 | -2.30153 | Unknown |
| *Mansc1* | 0.03965 | -2.28514 | Plasma membrane component |
| *Rbms3* | 0.0109571 | -2.27729 | Cytoplasmic RNA metabolism |
| *Golga3* | 0.0392264 | -2.27699 | Golgi apparatus transport of proteins and lipids to nucleus during mitosis |
| *Car1* | 0.0257676 | -2.2678 | Catalyzes to reversible hydration of carbon dioxide |
| *Hdc* | 0.0008771 | -2.23775 | Conversion of L-histidine to histamine involved in neurotransmission |
| *Ankfy1* | 0.0015828 | -2.23773 | Cytoplasmic protein and vesicle transport |
| *Msh3* | 0.0048097 | -2.2069 | Initiates post-replication DNA mismatch repair |
| *Dnahc2* | 0.0235939 | -2.20618 | Involved in axonemal microtubule formation |
| *Apaf1* | 0.0367202 | -2.19996 | Cytoplasmic initiator of apoptosis through formation of apoptosome |
| *Col7a1* | 0.0174913 | -2.19387 | Component of collagen and extracellular remodelling |
| *Sall2* | 0.0137244 | -2.18272 | Involved in transcriptional regulation during growth and development of neurons |
| *Katnal2* | 0.0307008 | -2.1754 | Microtubule severing through ATPase activity |
| *Slc38a11* | 0.0438682 | -2.17502 | Plasma membrane amino acid and sodium transporter |
| *Col4a2* | 0.02681 | -2.16956 | Component of collagen involved in inhibiting angiogenesis |
| *Npy2r* | 0.0213178 | -2.16915 | Neuropeptide signalling activity |
| *Rad50* | 0.0452278 | -2.16269 | DNA double-stranded break repair and cell cycle regulation |
| *Nmbr* | 0.039171 | -2.15422 | Binds neuromedin B to promote mitosis |
| *Tada3l* | 0.0106471 | -2.15409 | Promotes DNA-binding of transcriptional factors |
| *Nlrp3* | 0.0341535 | -2.15371 | NF-kappa B signalling to regulated inflammation and immune response |
| *Dhx29* | 0.0398495 | -2.15276 | Involved in mRNA translation initiation |
| *Col9a2* | 0.0063438 | -2.14271 | Component of collagen involved in extracellular remodelling and axon guidance |
| *Abca16* | 0.0127381 | -2.13578 | ATP-binding cassette, function unknown |
| *Duox2* | 0.0052049 | -2.11419 | NADH oxidase activity and cytokine release |
| *Wrn* | 0.0050367 | -2.1116 | RNA and DNA helicase |
| *Pard3b* | 0.0249889 | -2.10666 | Involved in cell cycle and tight junction formation |
| *Ptpru* | 0.0008582 | -2.10598 | Protein binding regulation of cell growth, differentiation and mitosis |
| *Clasp2* | 0.048169 | -2.08765 | Microtubule end binding and anchoring |
| *Grin2b* | 0.0422529 | -2.0848 | Glutamate receptor for prominent neurotransmitter in the retina |
| *Dnahc11* | 0.0020171 | -2.06752 | Ciliary dynein protein from microtubule motor activity |
| *4921528I07Rik* | 0.0376126 | -2.06285 | Unknown |
| *Ms4a4c* | 0.0019349 | -2.06017 | Unknown |

| | | | |
|---|---|---|---|
| *Tg* | 0.0232324 | -2.06013 | Thyroglobin (thyroid hormone) |
| *Nudt13* | 0.0313719 | -2.05882 | Unknown |
| *Oca2* | 0.0226697 | -2.05639 | Integral membrane protein - tyrosine transport |
| *Itgal* | 0.013379 | -2.05613 | Integrin expressed in leukocytes for intracellular adhesions |
| *Scn5a* | 0.0192309 | -2.04663 | Sodium channel, voltage-gated |
| *Spna1* | 0.0108579 | -2.04024 | Actin cytoskeleton organization |
| *Dpp10* | 0.0499214 | -2.03872 | Serine protease and binds K+ channels and alters functionality |
| *Coq7* | 0.0001781 | -2.03198 | Coenzyme Q involved in ubiquinone biosynthesis |
| *Rfc1* | 0.0063545 | -2.02704 | DNA replication factor C for DNA replication |
| *Telo2* | 0.008154 | -2.00621 | S-phase checkpoint protein |
| *Nlrc5* | 0.0164919 | -2.0028 | Inhibits NF-kappa-B activation and interferon signalling |
| *Brca1* | 0.021531 | -2.00024 | Tumour suppressor acts as a DNA damage sensor and mediates repairs |
| *Casc5* | 0.0081067 | -1.99927 | Microtubule-kinetochore attachments and chromosome separation |
| *L3mbtl* | 0.0497075 | -1.99779 | Chromatin modification and cell cycle regulation |
| *2310033E01Rik* | 0.0307551 | -1.98669 | Phospholipidase inhibitor |
| *Lctl* | 0.00774 | -1.96934 | Glycosidase |
| *Tcp10b* | 0.0271985 | -1.96595 | Unknown |
| *Mfn1* | 0.0067646 | -1.96589 | Mediates mitochondrial fusion |
| *Pfkfb3* | 0.0191326 | -1.96108 | Activator of the glycolysis pathway through early primary steps |
| *2610034M16Rik* | 0.0169822 | -1.96036 | Unknown |
| *Lars2* | 0.0062127 | -1.95613 | Aminoacyl-tRNA synthetase |
| *Aox4* | 0.0361653 | -1.94431 | Aldehyde oxidase involved in biosynthesis of retinoic acid |
| *Cdh23* | 0.0006493 | -1.94368 | Intracellular adhesion glycoprotein |
| *Ptbp2* | 0.0088319 | -1.94299 | Neuronal RNA regulatory protein |
| *Pla2g4d* | 0.0325627 | -1.94056 | Phospholipidase, liberates fatty acids |
| *Wdr52* | 0.0464484 | -1.93782 | mRNA processing and/or cytoskeleton assembly |
| *Csmd1* | 0.0052928 | -1.93496 | Integral membrane protein |
| *Txndc3* | 0.0474444 | -1.93491 | Unknown |
| *BC059842* | 0.0456172 | -1.93344 | Unknown, potential for CNS development |
| *Scnn1b* | 0.0456916 | -1.93172 | Sodium channel, voltage-gated control of electrolytes across epithelia |
| *C1qtnf5* | 0.001318 | -1.92401 | Basement membrane and cell adhesion |
| *Ift140* | 0.0364322 | -1.91511 | Microtubule formation of cilia |
| *Cdx4* | 0.0260372 | -1.9096 | RNA polymerase core promoter binding protein |
| *Hephl1* | 0.006727 | -1.90675 | Copper ion transport |
| *Slc5a4a* | 0.0281977 | -1.90241 | Unknown, transporter protein |
| *9030420J04Rik* | 0.0062036 | -1.90156 | Unknown |
| *Nphp4* | 0.0382606 | -1.89934 | Microtubule development and function |

| | | | |
|---|---|---|---|
| *Kif2c* | 0.0299502 | -1.89863 | Kinesin-like microtubule motor protein, mitotic chromosome segregation |
| *Hkdc1* | 0.0242806 | -1.8967 | Hexokinase activity and glucose metabolism |
| *Nbeal2* | 0.0373284 | -1.89554 | Regulates neurotransmitter receptor trafficking |
| *Pole* | 0.019369 | -1.89426 | DNA polymerase subunit |
| *Gucy2c* | 0.0005898 | -1.89361 | Enterotoxin receptor |
| *Acot12* | 0.0272659 | -1.89312 | Acetyl-CoA hydrolase activity |
| *Lhx8* | 0.0443032 | -1.89031 | DNA binding transcription factor |
| *1700040L02Rik* | 0.0025767 | -1.88678 | Unknown, important for cilia function |
| *Abcc5* | 0.0410045 | -1.88581 | ATP-binding cassette involved in export of cyclic nucleotides |
| *Cep152* | 0.0360524 | -1.88357 | Microtubule centrosome function |
| *Gm6190* | 0.0055903 | -1.87934 | Unknown |
| *Lrp2* | 0.0249245 | -1.8778 | Uptake of lipoproteins, sterols, hormones and vitamins from extracellular space |
| *Stag3* | 0.0005808 | -1.87163 | Cohesion of sister chromatids during mitosis |
| *4930555F03Rik* | 0.0406336 | -1.8666 | Unknown |
| *Prkdc* | 0.0292855 | -1.86298 | Protein kinase mediates double-stranded break DNA repair |
| *Vps13c* | 0.0425298 | -1.85981 | Unknown |
| *Optc* | 0.0157026 | -1.85973 | Binds collagen fibrils and regulations fibril formation and morphology |
| *Col27a1* | 0.0486116 | -1.85899 | Component of structural extracellular matrix |
| *Enoph1* | 0.0344511 | -1.85735 | Unknown, amino-acid metabolism |
| *Cd2ap* | 0.0110717 | -1.85617 | Scaffolding protein involved in organization of actin cytoskeleton |
| *Mcm5* | 0.0444294 | -1.85324 | Facilitates cell cycle and mitosis initiation |
| *Usp33* | 0.0228026 | -1.85306 | Deubiquinating enzyme |
| *Lcp2* | 0.0018684 | -1.85165 | T-cell receptor and immune response |
| *Senp6* | 0.0247478 | -1.85165 | Ubiquitin-like molecule |
| *Hsd17b3* | 0.0295071 | -1.84551 | Conversion of androstenedione to testosterone |
| *2010204N08Rik* | 0.0058221 | -1.84151 | High carbohydrates induces histone acetylation |
| *Setdb1* | 0.0326697 | -1.83627 | Mediates gene silencing and transcriptional repression |
| *Lef1* | 0.0049875 | -1.8353 | Transcription factor for T-cell receptors |
| *Kndc1* | 0.0267347 | -1.8341 | Regulates Ras GTPase activity and dendrite morphogenesis |
| *Gm6986* | 0.0120064 | -1.82782 | Unknown |
| *Col6a2* | 0.020632 | -1.8273 | Component of collagen binds extracellular matrix proteins |
| *Ippk* | 0.0300244 | -1.82475 | Mediates DNA repair and endocytosis through inositol-phosphate signalling |
| *Timeless* | 0.0430905 | -1.82091 | Involved in DNA polymerase activity, telomere maintenance and cell morphology |
| *C730048C13Rik* | 0.0126639 | -1.82063 | Unknown, solute carrier |
| *Slc9a10* | 0.0313326 | -1.82026 | Na+ transporting carboxylic acid decarboxylase |
| *Enah* | 0.011655 | -1.81313 | Axon guidance and T-cell receptor signalling |

| | | | |
|---|---|---|---|
| *Zfp597* | 0.0215991 | -1.81127 | Unknown |
| *Mbd2* | 0.0030594 | -1.81122 | Binds methylated DNA and represses transcription |
| *4430402I18Rik* | 0.0030179 | -1.80948 | Unknown |
| *B3galtl* | 0.0208824 | -1.80685 | Beta 1,3-galactosyltransferase |
| *Vps13b* | 0.0355605 | -1.80646 | Intracellular vesicle protein transport of CNS |
| *Lgr5* | 0.0418022 | -1.8045 | G-protein-coupled receptor |
| *Chd1l* | 0.039933 | -1.80225 | DNA helicase for DNA repair |
| *Rnf10* | 0.0066076 | -1.80152 | Ring finger protein DNA binding and transcription regulation |
| *Hmcn1* | 0.0369989 | -1.79986 | Immunoglobin, involved in anchorage of neurons to epidermis |
| *Wdr90* | 0.0235019 | -1.79898 | Unknown |
| *Ccdc33* | 0.032919 | -1.79699 | Unknown |
| *Pcsk5* | 0.0191332 | -1.79594 | Protein trafficking through the endoplasmic reticulum |
| *Htr3b* | 0.049761 | -1.79425 | Ion channel for fast, depolarizing response in neurons |
| *Myh7b* | 0.000595 | -1.79347 | Heavy chain of myosin (transport) |
| *F11* | 0.0400904 | -1.79324 | Factor 11 in blood coagulation |
| *Col4a3* | 0.0341158 | -1.79188 | Component of collagen |
| *Zbtb17* | 0.0187941 | -1.78929 | Regulation of c-myc (transcription factor) |
| *Srrt* | 0.031086 | -1.78731 | Regulation of transcription |
| *Chkb* | 0.0003588 | -1.78714 | Formation of phosohocholine or phosphoethanolamine by kinase activity |
| *Tecrl* | 0.0019138 | -1.7857 | Unknown |
| *Alg13* | 0.0429268 | -1.78543 | Lipid oligosaccharide biosynthesis |
| *Ank3* | 0.0474462 | -1.78453 | Ankyrin, cytoskeleton anchoring and cell mobility |
| *Hnf1a* | 0.0046702 | -1.78376 | Liver transcription factor |
| *Clic6* | 0.0270728 | -1.78355 | Chloride channel, intracellular transport |
| *Myo7a* | 0.01778 | -1.78178 | Myosin component, compromised in retinal degeneration |
| *Ubr2* | 0.0197904 | -1.78082 | Ubiquitin protein ligase, targets proteins for degradation |
| *Clcn1* | 0.0254486 | -1.77847 | Chloride channel, voltage-sensitive (muscle) |
| *Cdkl4* | 0.0059487 | -1.777 | Cyclin dependent kinase, cell cycle regulation |
| *Hdac7* | 0.0285512 | -1.77682 | Histone deacetylase, transcription and cell cycle regulation |
| *Eme2* | 0.0158106 | -1.77538 | Endonuclease involved in DNA repair |
| *Myh15* | 0.0186594 | -1.77466 | Myosin component, motor activity |
| *Myo15* | 0.0261537 | -1.77444 | Myosin component, motor activity |
| *Lypd6b* | 0.0207377 | -1.77414 | Unknown |
| *Reg3d* | 0.0443465 | -1.77411 | Enhances glucose tolerance, unknown function |
| *Vti1a* | 0.0191915 | -1.76861 | Vesicle transporting, SNARE interactions |
| *Tyr* | 0.035644 | -1.76852 | Facilitates conversion of tyrosine to melanin |
| *Morc1* | 0.0141049 | -1.76743 | Potential in regulating apoptosis |
| *Ciz1* | 0.0417301 | -1.76299 | Zinc-finger protein for CDKN1A interaction |
| *Itgb2l* | 0.0265953 | -1.76047 | Integrin, intracellular adhesions |
| *C8a* | 0.0459502 | -1.76019 | C8 of complement system |

| | | | |
|---|---|---|---|
| *Cenpk* | 0.0417527 | -1.75707 | Kinetochore assembly and mitosis progression |
| *Ahctf1* | 0.0486254 | -1.75615 | Transcription factor for mitotic gene transcription |
| *Ltbp2* | 0.0023953 | -1.75599 | Growth factor, involved in cell adhesion |
| *Dnahc12* | 0.0032213 | -1.75459 | Dynein, microtubule motor activity |
| *Chd4* | 0.0391803 | 1.75029 | DNA helicase, histone modifications |
| *Plg* | 0.0028306 | 1.75042 | Inhibitor of angiogenesis |
| *Fras1* | 0.0203383 | 1.75069 | Extracellular matrix protein for cell adhesion |
| *Rbl2* | 0.0395343 | 1.75129 | Retinoblasma-like involved in cell cycle regulation |
| *Steap3* | 0.0263896 | 1.75146 | Ferrireductase |
| *Ldlr* | 0.0340576 | 1.75369 | Low density lipoprotein receptor, endocytosis, cholesterol metabolism |
| *Ostf1* | 0.0028003 | 1.75443 | Cell adhesion, unknown function |
| *Nusap1* | 0.0061925 | 1.75444 | Nucleus spindle microtubule formation and integrity |
| *Esyt1* | 0.0333224 | 1.75465 | Unknown |
| *Cdh19* | 0.0447529 | 1.75584 | Cadherin, glycoprotein involved in cell adhesion |
| *Ptpn14* | 0.0377965 | 1.75649 | Mitosis, microtubule associated |
| *Plbd2* | 0.0444493 | 1.75824 | Phospholipase B, lipid metabolism |
| *Trim37* | 0.0419797 | 1.75946 | Protein-protein interactions |
| *Mov10l1* | 0.0119256 | 1.76008 | RNA helicase (testis) |
| *Asap3* | 0.0050632 | 1.76035 | Promotes differentiation, cell morphology and mobility |
| *Plcb2* | 0.0048519 | 1.76224 | Phospholipase C, lipid metabolism, synaptic function |
| *Rictor* | 0.0231411 | 1.76235 | Component of MTOR, growth factor |
| *Arfgap3* | 0.0098453 | 1.76245 | GTPase activity, promotes vesicle transport |
| *Col5a3* | 0.0262117 | 1.76265 | Component of collagen |
| *Scn11a* | 0.0163679 | 1.76309 | Sodium channel, voltage gated, ion regulation |
| *Lbp* | 0.0303646 | 1.76368 | Immune response, binds lipopolysaccharides |
| *Aire* | 0.0118822 | 1.76399 | Binds CREB, regulates expression of immunity genes |
| *Dkc1* | 0.0101854 | 1.76501 | DNA damage repair |
| *Hepacam2* | 0.0296601 | 1.76551 | Promotes mitosis and metaphase |
| *Mmp14* | 0.0165032 | 1.76592 | Extracellular matrix remodelling |
| *Nln* | 0.02361 | 1.76613 | Formation of neurotensin |
| *Plcb3* | 0.0120545 | 1.76731 | Phospholipase C, lipid metabolism, signal transduction |
| *Ubash3b* | 0.0103796 | 1.7674 | Ubiquitin domain inhibits endocytosis of growth factor |
| *Psat1* | 0.0206356 | 1.77061 | Phosphoserine aminotransferase involved in schizophrenia |
| *Skap2* | 0.0081311 | 1.771 | Responsible for src signalling pathway |
| *Strc* | 0.0479517 | 1.77119 | Stereocilin involved in stereocilia formation |
| *Atf5* | 0.0004549 | 1.77199 | Transcription factor inhibiting astrocyte differentiation |
| *Fam83b* | 0.0452632 | 1.77223 | MAPK activation and epithelial cell transformation |
| *Vwf* | 0.0212629 | 1.77274 | Glycoprotein involved in blood coagulation |
| *Irak3* | 0.0261513 | 1.77409 | Interleukin receptor, inhibits Toll-like receptors in glial cells |
| *Cchcr1* | 0.0388618 | 1.77477 | Cellular organization and proliferation |
| *Pls3* | 0.0403178 | 1.77554 | Plastin involved in actin-binding |

| | | | |
|---|---|---|---|
| *Ifih1* | 0.0230229 | 1.77892 | RNA helicase to remove secondary structure, ribosomal formation |
| *Patz1* | 0.0384599 | 1.77933 | DNA binding transcription factor and chromatin remodelling |
| *Siae* | 0.0263821 | 1.78277 | Deacetylation of sialic acids |
| *Qk* | 0.0243801 | 1.78342 | RNA binding protein for oligodendrocyte differentiation |
| *Ctnna3* | 0.0031298 | 1.7871 | Intercellular interactions, cell adhesion |
| *Plin3* | 0.0392788 | 1.78726 | Mannose receptor for transport of lysosomal hydrolase to endosome |
| *Col3a1* | 0.0050813 | 1.78733 | Component of collagen |
| *Dock9* | 0.0227907 | 1.78862 | Mediator of cytokinesis |
| *Cdkn1a* | 0.0200694 | 1.7907 | Cell checkpoint cell, mediates DNA damage repair |
| *Cd53* | 0.0165928 | 1.7919 | Cell growth and mobility, recruits T cells and macrophages |
| *Fam129b* | 0.0432193 | 1.79195 | Junction protein, can inhibit apoptosis processes *in vivo* |
| *Mtmr12* | 0.0174133 | 1.79408 | Lipid phosphatase |
| *Trpv5* | 0.0410751 | 1.79854 | Calcium channel involved in ion regulation |
| *Cbx1* | 0.0095426 | 1.80234 | Heterochromatin protein to maintain chromatin structure |
| *Unc93b1* | 0.0204658 | 1.80241 | Regulates Toll-receptors trafficking from endoplasmic reticulum, immune response |
| *Clic4* | 0.038684 | 1.80258 | Chloride channel, intracellular pH and transport |
| *Nsun2* | 0.0348147 | 1.80296 | mRNA translation, ensures codon/anti-codon matching |
| *Trpm5* | 0.0190737 | 1.80627 | Cation channel, ion homeostasis |
| *Tmem2* | 0.0164632 | 1.80853 | Extracellular organization |
| *Dpyd* | 0.017076 | 1.80883 | Uracil and thymidine metabolism, rate-limiting pyrimidine metabolism |
| *Slc4a4* | 0.0342031 | 1.80922 | Bicarbonate transported for intracellular pH maintenance |
| *Slc25a30* | 0.0216791 | 1.81068 | Small molecule inner mitochondrial matrix transporter |
| *Spef2* | 0.011715 | 1.81131 | Unknown |
| *Slamf7* | 0.0089023 | 1.81231 | Inhibits production of inflammatory cytokines |
| *Rap1gap* | 0.0231372 | 1.81419 | GTPase activity |
| *Atp5g1* | 0.0464895 | 1.81564 | Mitochondrial ATP synthase for proton transport during OXPHOS |
| *E030010N08Rik* | 0.0221112 | 1.81575 | Unknown |
| *Rbl1* | 0.0417279 | 1.81876 | Retinoblasma-like involved in cell cycle regulation |
| *Brip1* | 0.0323628 | 1.81949 | Interacts with BRAC1 to mediate double-stranded DNA break repair |
| *Gbp10* | 0.0079526 | 1.82162 | Immune response via interferon activation |
| *Erbb2* | 0.0414782 | 1.82236 | Epidermal growth factor involved in mitosis activation |
| *Ano5* | 0.0304613 | 1.82246 | Anoctamin calcuium-cholride channel |
| *Atp13a5* | 0.025178 | 1.82328 | ATPase, unknown function |
| *Ifltd1* | 0.0465649 | 1.8238 | Unknown |
| *Depdc1b* | 0.0204587 | 1.82578 | GTPase activation |
| *Rnf213* | 0.0016575 | 1.82609 | Zinc-finger protein for inter-protein interaction |
| *Lrp2bp* | 0.0483587 | 1.82778 | Unknown |

| | | | |
|---|---|---|---|
| *Klhl4* | 0.037315 | 1.82864 | Actin binding, unknown function |
| *Dapk2* | 0.0441918 | 1.82947 | Regulator of pre-programmed cell death |
| *Ddx60* | 0.0002651 | 1.83023 | RNA helicase to remove secondary structure |
| *Fyttd1* | 0.0002602 | 1.83227 | Unknown |
| *Lcp1* | 0.0305862 | 1.83464 | B-cell and T-cell activation and cell migration |
| *Sh3pxd2a* | 0.0016584 | 1.8374 | Regulates invadopodia (extracellular protrusions) |
| *Ccnb3* | 0.0017382 | 1.838 | Cyclin involved in cell cycle regulation |
| *Cfb* | 0.0018594 | 1.83836 | Complement factor B for complement activation and leukocyte recruitment |
| *Tmc3* | 0.0438492 | 1.84376 | Ion transport, unknown function |
| *Nmt2* | 0.0001749 | 1.84398 | N-myristoyltransferase 2 |
| *Naip5* | 0.0364918 | 1.84443 | Apoptosis inhibitory protein, inhibits proteins involved in apoptosis |
| *Plcg2* | 0.0092755 | 1.84448 | Phospholipase C, signal transduction and cellular messaging |
| *Dock1* | 0.0133594 | 1.84479 | Dedicator of cytokinesis, induces cell migration and phagocytosis |
| *Gbp5* | 0.0440096 | 1.84668 | Stimulates inflammation response to foreign antigens |
| *Cyp27a1* | 0.0372999 | 1.84918 | Cytochrome P450 variant, drug metabolism |
| *Zfp330* | 0.0358616 | 1.85066 | Zinc finger protein, unknown function |
| *Ttc12* | 0.0098723 | 1.85072 | Unknown |
| *Wdr64* | 0.0307521 | 1.85187 | Unknown |
| *Cadps2* | 0.0171056 | 1.85342 | Calcium secretion, synaptic function in neurons |
| *Itga8* | 0.0114879 | 1.85524 | Integrin, intracellular adhesions, cytoskeleton formation |
| *Atp1a4* | 0.0212119 | 1.85636 | ATPase, Na+/K+ transporter, neuron electrochemical gradient maintenance |
| *Tmem77* | 0.007951 | 1.85869 | Cellular apoptosis inducing |
| *Slc25a13* | 0.0030538 | 1.86195 | Mitochondrial glutamate/aspartate transfer |
| *Parp12* | 0.018547 | 1.86243 | mRNA post-translational modifications, ADP ribose |
| *Hydin* | 0.0313929 | 1.86592 | Cilia formation |
| *Oprm1* | 0.0181287 | 1.87057 | Opioid receptor, neuronal G-protein |
| *Rps6ka1* | 0.0374657 | 1.87268 | Ribosomal protein kinase, controls cell differentiation |
| *Gpr64* | 0.025621 | 1.87376 | G protein-coupled receptor, transmembrane |
| *Mthfd2* | 0.0019253 | 1.87397 | Nuclear mitochondrial NAD sequestering |
| *Nid2* | 0.0172362 | 1.87464 | Binds collagen, involved in cell adhesion |
| *Lsp1* | 0.0468358 | 1.8747 | Immune cell expression, involved in cell adhesion and extracellular remodelling |
| *Ppfia4* | 0.0098483 | 1.87761 | Protein tyrosine phosphatase, receptor type, tyrosine phosphorylation |
| *1700003E16Rik* | 0.0106796 | 1.88475 | Unknown |
| *Btk* | 0.0300985 | 1.88622 | Formation and functionality of B-cells |
| *Maged1* | 0.0174606 | 1.88731 | Programmed cell death, cancer antigen presentation |
| *Slc22a4* | 0.0382704 | 1.89398 | Solute carrier, cations and zwitterion transport |
| *Egfr* | 0.0279557 | 1.89959 | Epidermal growth factor receptor, cell proliferation |
| *Fanci* | 0.0060002 | 1.90404 | Fanconi anemia, complementation group I activation |

| | | | |
|---|---|---|---|
| *Muc5b* | 0.0041903 | 1.90453 | Mucin 5B, glycosylated protein involved in mucus formation |
| *Sympk* | 0.0036757 | 1.90828 | Post-transcriptional processing, involved in polyadenylation |
| *Meox1* | 0.019515 | 1.9114 | Developmental signalling |
| *Atp2c2* | 0.0266884 | 1.91293 | ATPase, cation transporter, neuron function |
| *Ano1* | 0.0409161 | 1.91376 | Anoctamin 1, calcium activated chloride channel, epithelial repair |
| *Padi2* | 0.0202878 | 1.91377 | Post-translational modifications mediated by calcium, CNS |
| *Apoe* | 0.0235635 | 1.9157 | Apolipoprotein E, metabolism of triglycerides (liver) |
| *Ncf2* | 0.0177262 | 1.91758 | Oxidoreductase activity, neutrophil specific |
| *Map3k6* | 0.0247556 | 1.91763 | Mitotic activated protein kinase |
| *Dock11* | 0.0036392 | 1.91909 | Dedicator of cytokinesis 11, extracellular remodelling |
| *BC057079* | 0.0142697 | 1.92342 | Focadhesin, cell adhesion, unknown function |
| *Col6a3* | 0.0133423 | 1.92357 | Component of collagen, extracellular matrix binding |
| *Ppp1r12c* | 0.0066925 | 1.92469 | Protein phosphatase 1, cytoskeleton formation and organization |
| *Elmo3* | 0.0392572 | 1.92727 | Engulfment of apoptotic cells, inflammation |
| *Ccdc88c* | 0.0496785 | 1.93007 | Developmental interactions, wnt signalling |
| *Abca8b* | 0.0061563 | 1.9319 | ATP-binding cassette, unknown function |
| *Dnahc17* | 0.0288871 | 1.93335 | Dynein, microtubule motor activity |
| *Lrrfip1* | 0.026914 | 1.9367 | DNA, RNA binding, regulation of transcription |
| *Slc7a7* | 0.0483406 | 1.94032 | Solute carrier, amino acid transporter (cationic and neutral) |
| *4833423E24Rik* | 0.0361036 | 1.94104 | Unknown |
| *Sytl1* | 0.0258357 | 1.94714 | GTPase activating protein |
| *Rtkn* | 0.0205158 | 1.9493 | Rhotekin scaffold protein inhibits GTPase Rho |
| *Orc6l* | 0.0257836 | 1.95019 | Initiates DNA replication in the nucleus |
| *Sec24d* | 0.045669 | 1.95193 | Vesicle transporting *in vivo* |
| *Pnldc1* | 0.0114914 | 1.95203 | Binds poly-A tail of mRNA, unknown function |
| *Ppp2r1b* | 0.0226536 | 1.95427 | Protein phosphatase, regulates protein function *in vivo*, cancer associated |
| *Abca14* | 0.0374404 | 1.95828 | ATP-binding cassette, unknown function |
| *Grhl3* | 0.0425524 | 1.96065 | Developmental transcription factor, endothelial cell migration |
| *Sorbs2* | 0.0308871 | 1.96262 | Cytoskeleton modifications |
| *Hk1* | 0.0367158 | 1.96385 | Hexokinase, glucose metabolism and glycolysis regulation |
| *Itpr3* | 0.0090388 | 1.96463 | Inositol 1,4,5-trisphosphate receptor, regulates calcium homeostasis |
| *Pyroxd2* | 0.0302111 | 1.96623 | Unknown |
| *Soat1* | 0.0179412 | 1.96706 | Formation of fatty acids and cholesterol |
| *Eng* | 0.043215 | 1.97004 | Vascular endothelial glycoprotein receptor |
| *Slc7a1* | 0.0123391 | 1.97223 | Solute carrier, cationic amino acids |
| *Trim6* | 0.0210848 | 1.9726 | Unknown |

| | | | |
|---|---|---|---|
| *Fbxl13* | 0.0324725 | 1.97696 | Cleave ubiquitin from ubiquitination products |
| *Spata6* | 0.0456238 | 1.9815 | Spermatogenesis, cell differentiation, unknown function |
| *Lrrc9* | 0.0356599 | 1.9848 | Unknown |
| *Myh3* | 0.0268801 | 1.98504 | Myosin component, motor activity, cell transport |
| *Zfp599* | 0.0370838 | 1.9856 | Zinc finger protein, unknown function |
| *2310008H04Rik* | 0.0400248 | 1.98643 | Unknown |
| *Cacna1h* | 0.0118042 | 1.98808 | Calcium channel, voltage-dependent, maintenance of membrane potentials |
| *Tbc1d4* | 0.0315198 | 1.99166 | Mediates transport of GLUT4 from endoplasmic reticulum to plasma membrane |
| *Dhx40* | 0.0420537 | 1.99427 | RNA metabolism, helicase |
| *Cep250* | 0.0243675 | 1.99597 | Centrosome formation and function during mitosis |
| *Gk5* | 0.0480136 | 1.99773 | Primary, regulatory step of glycerol metabolism |
| *Slc12a1* | 0.0416418 | 1.99777 | Solute carrier, unknown function |
| *Abca9* | 0.0438495 | 1.99907 | ATP-binding cassette, unknown function |
| *Klk1b16* | 0.0251047 | 2.00083 | Unknown |
| *Lama2* | 0.01227 | 2.0026 | Laminin component, extracellular component for remodelling and organization |
| *Atp8b1* | 0.0192593 | 2.00292 | Aminophospholipid transporter |
| *Baiap3* | 0.0003945 | 2.00342 | Angiogenesis regulator in the brain, involved in synaptic function |
| *Igfbp3* | 0.0358018 | 2.00685 | Insulin-like growth factor binding protein |
| *Lmna* | 0.0164179 | 2.00747 | Nuclear lamin, nucleus stability and chromatin structure |
| *Ephx1* | 0.0429007 | 2.00765 | Conversion of epoxides to trans-dihydrodoils for excretion |
| *Scn4b* | 0.0418185 | 2.0079 | Sodium channel, voltage-gated |
| *Samd4* | 0.0318405 | 2.00926 | RNA-binding, postranscriptional regulation |
| *Cyfip1* | 0.0210452 | 2.0136 | Regulates cytoskeleton and axon growth/formation |
| *Fbln2* | 0.0057021 | 2.01365 | Extracellular, neuronal structure development |
| *Ankrd26* | 0.0291523 | 2.02058 | Ankyrin, protein-protein interactions |
| *Eya4* | 0.0268545 | 2.02241 | Eye development, transcription activation |
| *Mx2* | 0.0307161 | 2.02348 | Dynamin and GTPase activity, heterochromatin formation |
| *Ifnar2* | 0.0370614 | 2.02687 | Interferon receptor, activates Janus kinases |
| *Wdr62* | 0.0108659 | 2.03409 | Cerebral development, function unknown |
| *Kif14* | 0.0261951 | 2.03591 | Kinesin, microtubule motor protein for transport |
| *Aldh1l1* | 0.0205617 | 2.03926 | Aldehyde dehydrogenase for removal of cytotoxic aldehydes |
| *Syk* | 0.0130348 | 2.04443 | Tyrosine kinase involved in cell proliferation, differentiation and phagocytosis |
| *Ddb2* | 0.0142656 | 2.04721 | DNA damage repair from UV light damage |
| *Flnc* | 0.0458499 | 2.04823 | Filamin involved in anchoring of actin cytoskeleton |
| *4930452B06Rik* | 0.0425945 | 2.05001 | Unknown |
| *Kntc1* | 0.0116476 | 2.05073 | Mitotic chromosome separation during anaphase |
| *Arhgef10* | 0.0173248 | 2.0533 | Rho GTPase, stimulates G-proteins |

| | | | |
|---|---|---|---|
| *Lamc2* | 0.0297158 | 2.05539 | Laminin component, extracellular component for remodelling and organization |
| *Stab1* | 0.0215188 | 2.05942 | Stabilin, receptor that endocytoses AGES, bacteria and lipoproteins |
| *Notch1* | 0.0027652 | 2.06196 | Intracellular signalling pathway mediator |
| *BC006779* | 0.0150289 | 2.06524 | DNA helicase, transcriptional activation |
| *Klf4* | 0.0404938 | 2.06701 | Transcription regulation and activation |
| *Sfmbt2* | 0.0316905 | 2.07112 | Regulation of transcription |
| *Rgs22* | 0.0449781 | 2.0731 | Regulator of G-protein signalling |
| *Atp8b4* | 0.0050661 | 2.07605 | Cation ATPase channel for phospholipid transport |
| *Pde2a* | 0.0162072 | 2.07675 | Phosphodiesterase, regulates endothelial cell proliferation and angiogenesis |
| *Col25a1* | 0.0282262 | 2.07705 | Component of collagen, brain specific |
| *Tmbim1* | 0.0386395 | 2.07758 | Inhibits apoptosis by reducing FAS trafficking |
| *Abcc3* | 0.0025065 | 2.07795 | ATP-binding cassette, transport of anions |
| *Msn* | 0.0492673 | 2.07988 | Moesin, links plasma membrane to actin as well as filopodia formation |
| *Sult5a1* | 0.0181227 | 2.08116 | Unknown |
| *Baiap2l1* | 0.0451011 | 2.08365 | Remodelling of the plasma membrane and cytoskeleton pedestal formation |
| *Col19a1* | 0.0015986 | 2.08366 | Component of collagen, maintenance of extracellular matrix |
| *Pnpla7* | 0.0413459 | 2.08459 | Lipid metabolism, function unknown |
| *Col5a2* | 0.0343231 | 2.08489 | Component of collagen |
| *Tap2* | 0.0128675 | 2.08507 | ATP-binding cassette, transport of peptides to endoplasmic reticulum |
| *Fgfr2* | 0.0317797 | 2.08935 | Fibroblast growth factor receptor, mitosis and differentiation |
| *Fblim1* | 0.0248279 | 2.10192 | Cell-cell adhesion modifications |
| *Ecm2* | 0.0480193 | 2.10255 | Extracellular matrix protein, function unknown |
| *Dock2* | 0.0211604 | 2.10412 | Cytoskeleton modifications for lymphocyte mobility |
| *Taf1d* | 0.0085981 | 2.11135 | RNA transcription regulation |
| *Col1a2* | 0.0138499 | 2.11752 | Component of collagen |
| *Magt1* | 0.023233 | 2.12737 | Magnesium transporter, N-glycosylation associated |
| *Nckap1l* | 0.0115969 | 2.12884 | Cell morphology regulation (hematopoietic) |
| *Ccdc150* | 0.0115571 | 2.12925 | Unknown |
| *Cd68* | 0.0202543 | 2.13446 | Glycoprotein in microglial cells, promotes activation of macrophages |
| *Svep1* | 0.0457553 | 2.13766 | Unknown |
| *Frem2* | 0.0232823 | 2.13927 | Basement membrane epithelia protein |
| *Vwa1* | 0.008256 | 2.14086 | Extracellular matrix protein |
| *Pebp4* | 0.0195098 | 2.14353 | Lipid binding, unknown |
| *Lrrk1* | 0.0116593 | 2.14701 | Unknown |
| *Gbp4* | 0.0277205 | 2.15078 | Guanylate binding protein, interferon induced |
| *Plcl2* | 0.009802 | 2.152 | Phospholipase C, modifications to GABA receptors |
| *Sgsm1* | 0.0143354 | 2.15698 | G-protein signalling, GTPase activity |

| | | | |
|---|---|---|---|
| *Ccl24* | 0.0205018 | 2.15907 | Cytokine CC, activates T-lymphocytes |
| *Kitl* | 0.0309238 | 2.16085 | Tyrosine-kinase receptor, neural cell development, cell mobility |
| *Kif20a* | 0.0312462 | 2.16108 | Kinesin, microtubule motor protein for transport |
| *Dnahc1* | 0.0089948 | 2.17058 | Dynein, microtubule motor activity |
| *Calcrl* | 0.0195045 | 2.17483 | Calctonin receptor |
| *Abcc4* | 0.0495595 | 2.18036 | ATP-binding cassette involved in anion cycling |
| *Abca13* | 0.0068074 | 2.18061 | ATP-binding cassette, transport (unknown function) |
| *H2-D1* | 0.0232616 | 2.1838 | Major histocompatibility component |
| *Hpse* | 0.0361428 | 2.18872 | Heparanase, component of extracellular matrix and cell mobility |
| *Nt5dc1* | 0.0014142 | 2.19853 | 5'-nucleotidase protein |
| *Abca12* | 0.0210858 | 2.20527 | ATP-binding cassette, small molecule transport |
| *Ecm1* | 0.0133792 | 2.20762 | Cell structure interaction for extracellular remodelling |
| *Pth1r* | 0.0414317 | 2.21192 | Parathyroid hormone receptor |
| *Mertk* | 0.0157256 | 2.21711 | MER/AXL/TYRO3 receptor kinase, involved in RPE phagocytosis regulation |
| *Myom2* | 0.0104973 | 2.21919 | Myomesin 2, muscle cell component |
| *Clca1* | 0.0381724 | 2.22377 | Chloride channel accessory protein |
| *Pappa2* | 0.0093243 | 2.22752 | Regulates intracellular insulin-like growth factor availability |
| *AW551984* | 0.0204154 | 2.23252 | Unknown |
| *Nrap* | 0.0457788 | 2.23485 | Nebulin-related anchoring protein, actin binding |
| *Myo5c* | 0.0035317 | 2.23524 | Myosin component, actin motor activity |
| *Pld2* | 0.0463916 | 2.23549 | Hydrolysis of phosphatidylcholine, cell cycle and transcription regulation |
| *Serpina3a* | 0.0458079 | 2.23824 | Serine peptidase inhibitor |
| *Iqgap3* | 0.0152522 | 2.23908 | GTPase activation |
| *Ermp1* | 0.026493 | 2.24009 | Endoplasmic reticulum metallopeptidase |
| *Tnxb* | 0.0431861 | 2.24326 | Tenascin, reduces cell adhesion |
| *Fut8* | 0.0406937 | 2.24542 | Transfers fucose to glycopeptides |
| *4933428G20Rik* | 0.0347269 | 2.24603 | Unknown |
| *Mpa2l* | 0.0362691 | 2.24733 | Macrophage activation like, GTPase activity |
| *Trpm4* | 0.0428844 | 2.25314 | Calcium ion channel, non-selective |
| *Myof* | 0.0059642 | 2.27105 | Membrane vesicle formation, membrane fusion |
| *Pkhd1l1* | 0.0083783 | 2.2745 | Potential role in immune response |
| *Poln* | 0.0388691 | 2.2817 | DNA polymerase subunit |
| *Fn1* | 0.0160342 | 2.2906 | Fibronectin glycoprotein, cell mobility |
| *Sfrp4* | 0.0167618 | 2.29162 | Regulates Wnt signalling, receptor protein |
| *Myh11* | 0.02687 | 2.30494 | Myosin, microtubule motor activity |
| *Plin1* | 0.0405267 | 2.30902 | Lipid storage, lipolysis regulation and inhibition |
| *Ccdc46* | 0.0344049 | 2.31067 | Unknown |
| *Efcab7* | 0.0026008 | 2.32595 | Unknown |
| *Scml2* | 0.033619 | 2.33493 | Transcription regulation (inhibition), polycomb protein |

| | | | |
|---|---|---|---|
| *Myo15b* | 0.0067032 | 2.33608 | Myosin, microtubule motor activity |
| *Cd93* | 0.0376391 | 2.33913 | Immune response to apoptotic cells, cellular migration |
| *Aldh2* | 0.0450249 | 2.34462 | Aldehyde dehydrogenase for removal of cytotoxic aldehydes |
| *Kynu* | 0.0160715 | 2.34696 | Amino acid metabolism of tryptophan, NAD regeneration |
| *C920025E04Rik* | 0.0365824 | 2.34911 | Major histocompatibility binding protein |
| *Galnt3* | 0.0292916 | 2.35444 | Polypeptide N-acetylgalactosaminyltransferase |
| *Dse* | 0.0420728 | 2.36637 | Induces immune response |
| *Gpd2* | 0.0399365 | 2.37661 | Secondary step of glycerol metabolism, glycerol shuttle |
| *Pdzrn4* | 0.0249827 | 2.39325 | Zinc-ring finger protein, unknown function |
| *Adhfe1* | 0.0358737 | 2.39843 | Alcohol dehydrogenase |
| *Vipr1* | 0.0160948 | 2.40598 | Activation of adenylate cyclase |
| *Fxyd5* | 0.0435462 | 2.40968 | Ion transport regulator, functions during high chemokine production |
| *B2m* | 0.0238666 | 2.42012 | Major histocompatibility complex heavy chain associated, microglial activation |
| *Renbp* | 0.0156324 | 2.42411 | N-acetylglucosamine metabolism |
| *Dlec1* | 0.0277845 | 2.4261 | Deleted in cancer progression, unknown function |
| *Itpr2* | 0.039317 | 2.43982 | Inositol 1,4,5-trisphosphate receptor, cell signalling |
| *Slc44a5* | 0.0399251 | 2.44105 | Solute carrier, unknown function |
| *Igtp* | 0.0366583 | 2.44422 | Interferon gamma subunit |
| *Fas* | 0.0160064 | 2.45018 | TNF receptor for cell apoptosis |
| *Mvp* | 0.0233917 | 2.45571 | Regulates MAP kinase for drug metabolism |
| *Ncapd2* | 0.0265338 | 2.46031 | Binds histones during mitosis |
| *Sec16b* | 0.0451595 | 2.46535 | Endoplasmic reticulum organizational transport of mature proteins |
| *Tspan12* | 0.0455787 | 2.47621 | Cell surface tetraspanin for cell growth and mobility |
| *Slc15a1* | 0.0488859 | 2.48534 | Oligopeptide transporter for protein metabolism |
| *Osmr* | 0.0118207 | 2.49015 | Interleukin receptor for inflammation response |
| *Gm7298* | 0.0104095 | 2.49301 | Unknown |
| *Thsd7b* | 0.0234948 | 2.51864 | Unknown |
| *1700011F14Rik* | 0.0159698 | 2.53491 | Unknown |
| *Clic5* | 0.0454731 | 2.54845 | Chloride intracellular channel |
| *Diap1* | 0.038375 | 2.54863 | Axon guidance and elongation |
| *Nup133* | 0.0421358 | 2.54899 | Formation of nuclear envelope during mitosis |
| *Mmel1* | 0.0193461 | 2.56265 | Endopeptidase for phosphate homeostasis |
| *Atp10d* | 0.0486888 | 2.57034 | ATPase ion transport across concentration and electrochemical gradients |
| *Obfc2a* | 0.0140833 | 2.57695 | Single-stranded DNA binding protein for replication, repair and recombination |
| *Nos2* | 0.0316639 | 2.58763 | Nitric oxide synthase for regulation of nitric oxide |
| *F3* | 0.0378579 | 2.58869 | Factor 3 in blood coagulation |
| *Dnahc8* | 0.0312568 | 2.60645 | Dynein, microtubule motor activity |
| *Sdk2* | 0.0422683 | 2.60932 | Immunoglobin, synaptic maintenance |

| | | | |
|---|---|---|---|
| *Pola1* | 0.0082495 | 2.61239 | Subunit of DNA polymerase involved in initiation of DNA replication |
| *Myo1e* | 0.0024885 | 2.61773 | Non-muscle myosin for actin motor activity |
| *Dysf* | 0.0130688 | 2.64452 | Membrane repair and regeneration |
| *Zfp748* | 0.0486775 | 2.67676 | Unknown, zinc-finger protein |
| *Csmd2* | 0.00496 | 2.68896 | Unknown |
| *Mllt4* | 0.0447334 | 2.70289 | Organization of cell junctions and extracellular interactions |
| *Cast* | 0.0018883 | 2.71118 | Calpain inhibitor which is involved in neuronal vesicle trafficking |
| *Aox3l1* | 0.0153934 | 2.71173 | Retinol and amino-acid metabolism |
| *Asah2* | 0.0132518 | 2.71609 | Production of sphingosine, induce apoptosis |
| *Fndc3c1* | 0.0074993 | 2.72731 | Fibronectin |
| *Lama3* | 0.0032464 | 2.78592 | Extracellular remodelling and migration |
| *Rassf2* | 0.0486192 | 2.78738 | Tumor suppressor gene, Ras associated |
| *Mug1* | 0.0151463 | 2.80096 | Unknown |
| *Cps1* | 0.0242031 | 2.81088 | Primary, regulatory step of urea cycle and ammonia removal |
| *Il18r1* | 0.0389371 | 2.81156 | Interleukin receptor for microglial activation and cytokine release |
| *Myh9* | 0.0255247 | 2.82263 | Non-muscle myosin for cell mobility and morphology |
| *B230120H23Rik* | 0.0352319 | 2.82642 | Unknown |
| *Utp20* | 0.0292205 | 2.84246 | Small nucleolar RNA for 18S assembly |
| *Abca15* | 0.0133014 | 2.84975 | ATP-binding cassette |
| *Adcy10* | 0.0050507 | 2.85833 | Intracellular bicarbonate sensor and pH regulator |
| *Dock10* | 0.0090131 | 2.89996 | Directs cytokinesis |
| *Hhip* | 0.0086926 | 2.91551 | Involved in hedgehog recruitment for development |
| *Nrk* | 0.0136839 | 2.94234 | Activates JNK pathway |
| *Clspn* | 0.0035071 | 2.94334 | Cell cycle checkpoint protein, arrests cell cycle |
| *Gmnn* | 0.0215492 | 2.99088 | Inhibits DNA replication, cell cycle checkpoint protein |
| *Cd97* | 0.0149192 | 2.99546 | Intercellular interactions, involved in leukocyte activation and recruitment |
| *Xdh* | 0.0064959 | 3.00028 | Metabolism of purines, involved in microglial activation |
| *Myo1c* | 0.0374662 | 3.00731 | Myosin component for actin motor transport |
| *Als2cl* | 0.0282106 | 3.0433 | Protein localization and transport |
| *Myo1f* | 0.0001664 | 3.04358 | Myosin component for microtubule transport |
| *H2-K1* | 0.0371741 | 3.06774 | Major histocompatibility component |
| *Nfkbil2* | 0.0214434 | 3.14832 | Inhibits NF-kappa-B activation |
| *F13a1* | 0.0234937 | 3.21301 | Factor 13 in blood coagulation |
| *Plec1* | 0.0253006 | 3.22776 | Unknown |
| *Kif4* | 0.0073226 | 3.3724 | Kinesin microtubule motor activity |
| *Trpm6* | 0.0435942 | 3.47521 | Ion channel for magnesium transport in epithelial cells |
| *Csmd3* | 0.0211546 | 3.53038 | Unknown |
| *Bub1b* | 0.0050054 | 3.78249 | Spindle checkpoint to inhibit cell cycle until proper chromosome separation |

| | | | |
|---|---|---|---|
| *Dpp4* | 0.0179589 | 4.02866 | T-cell activation, involved in immune response |
| *Muc5ac* | 0.0183852 | 4.03264 | Extracellular remodelling |

***** Microarray was performed by A. Laliberté (2010).[103] Cut-offs set at: Fold change > ± 1.75, $p < 0.05$.

† Annotation based on NCBI Gene[184] [National Center for Biotechnology Information, U.S. National Library of Medicine, Bethesda MD]

‡ Pathway is ordered by increasing p-value.

**Curriculum vitae:**

# Eric Dolinar

Department of Biology, The University of Western Ontario
1151 Richmond St. North, London, Ontario

## EDUCATION

**Western University** — **London, Canada**
*Masters of Science in Biology Candidate – Cell and Molecular Biology* — Expected: August 2014

- **Supervisor:** Dr. Kathleen Hill
- **Proposed Thesis Title:** Early Mechanisms of Retinal Degeneration in the *harlequin* Mouse

**Western University** — **London, Canada**
*Bachelor of Science (Honors) – Honors Specialization in Genetics* — 2012

**Université de Moncton** — **Moncton, Canada**
*Completed the Explore 5-week Summer Immersion French Program* — Summer 2008

## SCHOLARSHIPS & ACADEMIC HONORS

| | |
|---|---|
| **Best Graduate Presentation Travel Award – Ophthalmology Research Day ($1000)** | **2014** |
| **Ontario Graduate Scholarship ($15K)** | **2013-2014** |
| **Western Science Graduate Entrance Scholarship ($2500)** | **2012** |
| **Dean's Honor List, Faculty of Science, Western University** | **2010-2012** |
| **Laurene Paterson Estate Scholarship ($2000)** | **2011-2012** |
| **James F. Birch Bursary ($650)** | **2011-2012** |
| **William F.M. and Helen M. Haight 125th Anniversary Alumni Bursary ($1000)** | **2009-2010** |
| **Western Scholarship of Excellence ($2000)** | **2008-2012** |
| **Queen Elizabeth Aiming for the Top Scholarship ($3500)** | **2008-2009** |
| **Governor General Academic Medal (Bronze)** | **2008** |

## PRESENTATIONS AND ABSTRACTS

**Dolinar EA**, MacPherson TC, Laliberté AM, Van Gaalen J, Hutnik CML, Hill KA. Non-metric Multidimensional Scaling of Electroretinogram Oscillatory Potential Data achieves Early Diagnosis of Retinal Degeneration in a Mouse Model of Mitochondrial Dysfunction. The Association for Research in Vision and Ophthalmology 2014, *poster presentation*.

**Dolinar EA**, Van Gaalen J, MacPherson TC, Hutnik CML, Hill KA. Electroretinogram Oscillatory Potentials provide a Non-invasive Diagnostic Analysis of Retinal Cell Function in a Mouse Model of Mitochondrial Dysfunction and Retinal Degeneration. Ophthalmology Research Day 2013 - Ivey Eye Institute, London Ontario, *oral presentation*

Li A, **Dolinar EA,** Van Gaalen J, MacPherson TC, Hutnik CML, Hill KA**.** Memantine Treatment does not shift the Aberrant Electroretinogram Oscillatory Potential Profiles of the Harlequin Mouse Model of Retinal Degeneration due to Mitochondrial Dysfunction. Ophthalmology Research Day 2013 - Ivey Eye Institute, London Ontario, *oral presentation*

Van Gaalen J, Bedore, J, McDonald I, **Dolinar EA,** Li A, Martyns A, Prado V, Prado M. Impaired Retinal Function is Associated with a Lack of Acetylcholine-Mediated Retinal Waves during Development. Ophthalmology Research Day 2013 - Ivey Eye Institute, London Ontario, *oral presentation*

Faraz, MA, Li A, **Dolinar, EA**, Hill KA. Assessment of the Integrity of the Blood Retina Barrier in a Mouse Mimic of Oculodentodigital Dysplasia (ODDD)-Related Glaucoma. Ophthalmology Research Day 2013 - Ivey Eye Institute, London Ontario, *oral presentation*

**Dolinar EA**, Wagner J, Faraz MA, Cadesky A, Hill KA. An Eye to the Future: Identifying Early Disease Mechanisms in a Mouse Model of Retinal Degeneration. Biology Graduate Research Forum 2013 – Department of Biology, London, Ontario, *oral presentation*

Faraz, MA, Li A, Mayers J, **Dolinar EA**, Hill KA. Early mechanisms of retinal degeneration in a mouse mimic of oculodentodigital dysplasia (ODDD)-related glaucoma. International Conference on Clinical & Experimental Ophthalmology 2014, *oral presentation*

## RESEARCH & TEACHING EXPERIENCE

**Western University** **London, Canada**
*Graduate Student – Department of Biology*
2012-2013

- Managed the Experimental Eye Research Facility and animal colony for the duration of my project
- Technical Molecular biology skills include: PCR, DNA and RNA isolation, qPCR, histology, cloning, fully body mouse dissection including brain and retina, injections, and fluorescent microscopy
- Developed protocols for mathematically modelling (MATLAB) retinal waveforms using electroretinography
- Responsible for continual organization of all molecular biology-based projects for five undergraduate students including NSERC scholarship winners and fourth-year honors thesis students

**Western University** **London, Canada**
*Teaching Assistant – Gene Regulation (3597), Advanced Genetics (3595) and Organismal Physiology (2601)*
2012-2013

- Organized tutorial discussions for a class of 150 students on current topics in gene regulation
- Lectured concepts, theories and novel ideas of gene regulation and advanced genetic techniques
- Graded final exams, lab reports, tutorial assignments and term papers